Omar Darío López Mejia
Jaime A. Escobar Gomez   *Editors*

# Numerical Simulation of the Aerodynamics of High-Lift Configurations

Springer

# Numerical Simulation of the Aerodynamics of High-Lift Configurations

Omar Darío López Mejia
Jaime A. Escobar Gomez

Editors

# Numerical Simulation of the Aerodynamics of High-Lift Configurations

*Editors*
Omar Darío López Mejia
Department of Mechanical Engineering
Universidad de Los Andes
Bogotá
Colombia

Jaime A. Escobar Gomez
Aeronautics Engineering
Universidad de San Buenaventura
Bogotá
Colombia

*To REM*

# Preface

Wing loading has been increased as a result of a combination of higher cruise speeds and aerodynamic efficiency but with adverse effects on stall speeds. At the same time, the length of the airports' runaways cannot be increased due to economic reasons, in addition to the fact that the speeds of takeoff and landing are limited to satisfy safety standards. It is in this context in which the importance of high-lift devices for commercial aerodynamic applications comes into play.

The design of high-lift devices is focused on simpler systems to maximize the lift and reduce maintenance costs. The aerodynamic design of these devices is restricted by takeoff and landing distances, safe speeds during landing and takeoff and climb rates. All these operational parameters impose restrictions on aerodynamic properties such as the lift coefficient ($C_L$), lift-to-drag ratio (L/D) and stall angle of attack. In recent years, numerical simulations have played an important role in the prediction of these aerodynamics properties. As an example, NASA and the American Institute of Aeronautics and Astronautics (AIAA) have organized three events related to the application of numerical simulations in the prediction of the aerodynamic properties of high-lift configurations since 2010. I have personally participated in these events, called High-Lift Prediction Workshop (HiLiftPW), and in general the conclusion is that the problem of correctly estimating the turbulent and separated flow near $C_{Lmax}$ is still an important challenge for modern computational codes and software. Also, there is still a need to develop reliable turbulence models for this application, and the computational cost of these simulations is considerable, given the fact that finer meshes (around 200-M cells) are needed to reduce the deviation of the numerical solution between the various different codes and softwares. Numerical results consistently show that $C_L$ is typically under-predicted, as well as are the drag and the magnitude of the pitching moment. In this context, this book is devoted to gathering some of the results of the most recent version of the HiLiftPW that was held in June 2017.

This book has six chapters dedicated to the numerical simulations of high-lift configurations and specifically all of them that are related to full Navier–Stokes (NS) solvers. This means that the numerical and computational techniques used for these contributions are based on Computational Fluid Dynamics (CFD). All the

chapters discuss numerical solutions of the high-lift system proposed for the third HiLiftPW held in Denver in June 2017. All the chapters show numerical solutions for the aerodynamic properties of the models studied and comparisons (validation) with experimental data when available.

The first chapter is a review of high-lift configurations in order to provide a context for the book. This chapter also shows some results of the simulation of the flow around the High-Lift Common Research Model (HLCRM), which was one of the models introduced in the last HiLiftPW. These results are briefly introduced only to give some insight to the reader about the physics of the turbulent flow around these devices. The second chapter is dedicated to the topic of grid generation of high-lift configurations for CFD simulations. Typically, this is not a topic deeply discussed in textbooks or technical articles, so I personally consider that this contribution helps to give a better idea of the challenges and main features that need to be considered when facing such a complex problem. One of the interesting topics in this chapter is the discussion of the guidelines given by the AIAA on grid generation for high-lift systems. The third, fourth and fifth chapters are all dedicated to numerical computations of the Japanese Aerospace Exploration Agency (JAXA) Standard Model (JSM), using three different CFD solvers and simplifications of the governing equations. For example, Chapter "Incompressible Solutions About High-Lift Wing Configurations" is devoted to the use of an incompressible flow solver. The conclusions reached and observations made in this chapter are quite interesting since one of the main requirements of the HiLiftPW is to use fully compressible NS solvers for the simulations. Chapter "Numerical Investigations of the Jaxa High-Lift Configuration Standard Model with MFlow Solver" deals with the numerical solution of the JSM using a fully compressible NS solver; a very interesting topic discussed in this chapter is the High-Performance Computing (HPC) resources needed and the estimation of efficiency for performance in parallel computation for this kind of simulation. In Chapters "Incompressible Solutions About High-Lift Wing Configurations" and "Numerical Investigations of the Jaxa High-Lift Configuration Standard Model with MFlow Solver", computations are performed using the Finite Volume (FV) method which is the standard way to discretize the governing equations. Nevertheless, in Chapter "Time-Resolved Adaptive Direct FEM Simulation of High-Lift Aircraft Configurations", the numerical method used for computing the solution of the flow is the Finite Element Method (FEM). Since I read the book "Computational Turbulent Incompressible Flow" by Professor Hoffman in 2007, I have been intrigued by the capabilities of the FEM proposed in that book. In Chapter "Time-Resolved Adaptive Direct FEM Simulation of High-Lift Aircraft Configurations", this question is solved by showing the efficiency of the solver based on this methodology and its advantages in comparison with other numerical techniques typically used in CFD. Finally, Chapter "RANS Simulations of the High Lift Common Research Model with Open-Source Code SU2" deals with the numerical solution of the flow around the HLCRM using an open-source code called SU2. This final chapter also uses an FV method for solving the fully compressible NS equations.

It is expected that this book can serve as a reference for graduate students, as well as researchers in the field of CFD applied to the aerodynamics of high-lift configurations. Designers and engineers from the aeronautical industry may also benefit from the content of the book as it provides the state-of-the-art in CFD computations applied to the prediction of aerodynamic properties of high-lift configurations, as well as flow characteristics. We hope that the way the book is organized helps the reader to find a specific topic of interest and to engage the reader as he/she goes from one section to the next one. Finally, I would like to acknowledge the help of Dr. Rumsey and Dr. Slotnick during the 3rd HiLiftPW for helping me in the realization of this project.

Bogotá, Colombia                                                    Omar Darío López Mejia
August 2017                                                              Associate Professor

# Contents

# Review on High-Lift Systems for Aerodynamic Applications

**A. Matiz-Chicacausa and C. A. Sedano**

**Abstract** One of the main focal points in aircraft aerodynamics has been the study and development of high-lift devices and systems. These are designed in order to enable manipulation of the lifting force at various moments during flight (takeoff, cruising and landing) in such a way that the aircraft can increase or decrease the lift-to-drag ratio accordingly. High-lift systems are classified into trailing-edge and leading-edge devices. The first consists mainly of various types of flaps such as the plain flap, Fowler flap or the Krueger flap which act to increase the lifting force by reducing minimum speed, delaying flow separation or increasing the effective camber or the wing area. On the other hand, leading-edge devices consist mainly of fixed slots, movable slats, leading edge flaps or cuffs. The main idea of these devices is to sustain the lifting force even when the aircraft's speed decreases. Nowadays, there has been increasing interest in the study of high-lift systems using Computational Fluid Dynamics (CFD), instead of the experimental techniques traditionally used. Nevertheless, CFD techniques still face some major challenges that in some cases can only be solved through experimentation.

## 1 Introduction

The importance of the high-lift systems in modern transport aircraft is the significant payoff in the aircraft's performance during take-off and landing stages. To design efficient high-lift systems, several methods have been employed; most recently, Computational Fluid Dynamics (CFD) simulations, with the rapid growth of computational capabilities, have achieved increased accuracy and reliability of their results making it a more suitable tool and complementing wind-tunnel tests. The use of

A. Matiz-Chicacausa (✉)
Universidad de San Buenaventura, Cra 8H N° 172-20, Bogotá, Colombia
e-mail: amatiz@usbbog.edu.co

C. A. Sedano
Universidad de Los Andes, Cra 1 Este N°18A-12, Bogotá, Colombia
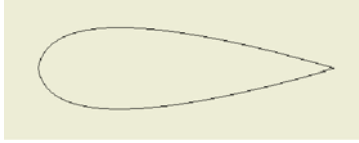e-mail: ca.sedano1167@uniandes.edu.co
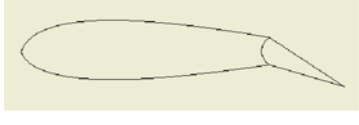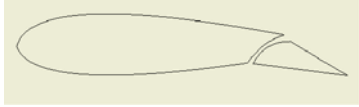
numerical simulations has resulted in wing designs that enable the bearing of higher loads without reducing cruise performance.

Although, high-lift studies trace back to the late 1920s, most of those works were empirical and the experimental databases were not widely published. As a historical note, after the end of the Cold War, nations worldwide(especially NATO countries) required that military forces react quickly anywhere in the world; thus, military transport aircraft needed to be able to operate on short landing/take-off strips [1]. This demanded better designs of high-lift systems. It was not until Smith's work in 1975 that a theoretical work published the explanations for those systems, establishing a baseline for future developments [2].

High lift-systems surfaced as a solution to reduce the extra baggage that the wing area constituted at cruising conditions, but was necessary for take-off and landing; namely flaps, slats, slots etc. Nowadays, high-lift systems are classified into two groups: leading-edge and trailing-edge devices. Trailing edge devices were the first

**Table 1** Standard high lift devices

| High-lift device | Schematic | Maximum $C_L$ |
|---|---|---|
| Plain airfoil | | 1.3–1.5 |
| Plain flap | | 2.4–2.5 |
| Split flap | | 2.6–2.8 |
| Leading-edge slat | | 2.3–2.5 |
| Single-slotted flap | | 2.9–3.1 |
| Double-slotted flap | | 3.1–3.3 |

to be developed, starting in the 1920s and 1930s. By far, the choice of wing area was established according to the speed at takeoff or landing [3]. However, the appearance of such devices provided sufficient lift while having a small wing area. The reduction in the wing area enabled designers to reduce structural weight; hence, skin- friction drag was decreased. The creation of this kind of devices had consequences in wing design and aircraft structure, therefore, also in fuel consumption, manufacturing and operational costs. Some of the standard devices employed since 1920 can be seen in Table 1, along with the respective increase in lift provided by each device.

## 2 Trailing Edge Devices

The first and most common high-lift system was the plain flap. Henri Farman first used this in 1908, however, engineers at the time were not interested in such devices. It was not until 1914 that they were installed in the SE-4 biplane and became standard on airplanes, built by Fairey beginning in 1916 [3]. The flaps are a movable part attached to the trailing edge of the wing. These are used to lower the minimum speed to produce sufficient lift force, such that the aircraft can fly, and also to increase the angle of deployment for takeoff and landing configurations. The plain flap is limited to a 20 degree angle of deployment that limits its capability to produce lift [4].

Three different innovators later developed the single-slotted flap independently: a German pilot G.V. Lanchman (1917), Sir Frederick Handley Page in England and an engineer working for Junkers in Germany. The principle of operation is that the high-pressure air below the wing is forced through the gap between flap and wing, delaying flow separation, while the airflow remains attached to the flap to increase lift. In the beginning, the patent was rejected with the argument that such a device could destroy the wing's lift. However, after Prandtl at Gottingen University were convinced to perform wind-tunnel tests, it was found that lift increased by 63%, hence Lanchman got his patent and shared rights with Page. After a two-year, wind-tunnel testing program, the single-slotted flap's viability was established beyond a doubt.

At the same time, in the US, the split flap was developed, which increased both lift and drag. The increase in drag was found beneficial during landing, resulting in a reduction of the lift-to-drag ratio, thus reducing the landing distance. This type of slat was the first type used on an airplane designed in the US, although it does not produce a significant increase in lift. The next development was the Fowler flap (see Fig. 1) by an engineer who worked with the Army Air Corps in 1924, Harlan D. Fowler. It combined two effects: The deflection of the flap was able to increase the effective camber of the wing to increasing lift. Additionally, the flap could be deployed increasing the lift by increasing the wing area. Up until 1932, the National Advisory Committee for Aeronautics (NACA) tested it, proving the value of this kind of flap. Later on, some variations of the Fowler flap were developed, such as the double-slotted Fowler flap. The single-slotted is rarely used in industry; however, the double or multiple-slotted Fowler flap are still used on modern aircraft. For instance,

**Fig. 1** Fowler flaps
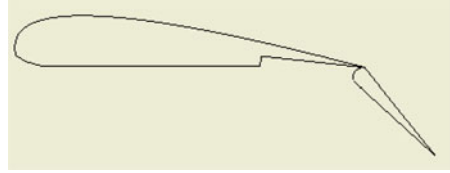


Boeing developed the triple-slotted Fowler flap to be used on the 727 jet transport in the 1960s. Further work resulted in the leading-edge slat and the era of leading-edge high-lift devices.

## 3 Leading Edge Devices

The leading-edge device is a small, highly cambered airfoil, placed on the leading edge of the airfoil, usually called a slat. This device increases the camber of the wing and slightly reduces chord; since there is a small gap between the slat and wing, it modifies the pressure distribution over the top surface of the airfoil, resulting in a higher pressure over the top surface on the main body of the wing. The most common leading edge devices are the fixed slots, movable slats, leading-edge flaps and cuffs [5]. Among them there are the rigid Kruegers and variable camber Kruegers, devices that today are used on jet transports [6].

The objective for the leading-edge design was to enable the wing to reach high angles of attack for takeoff and landing configurations. This can be achieved by providing sufficient slat-chord across the span and by defining suitable a slat placement [6].

Since 1932, NACA (today NASA) has been performing various tests in order to control the takeoff and landing configurations of aircrafts. In order to do so, the implementation of fixed slots at the leading edge of the wings was the first approach to improving the lift load on the wings [7]. This way, the lifting force could be sustained, even though the aircraft's velocity decreased. The main issue with the slots is the fact that they remain fixed. However, the movable slats, provide the same effect as the slots; since these are able to move, the slats can change the angle of attack of the wing according to the situation (landing, takeoff or cruising). Also by separating itself from the wing, the slat configuration allows airflow such that the flow separation is delayed.

The leading-edge flaps, as well as the trailing-edge flaps, are intended to increase the camber of the wing. This in turn, leads to enforcing drastic changes in the lift-to-drag ratio. Finally, the leading-edge cuffs are intended to enforce the same effect as the flaps, however the cuffs are fixed to the wing. The main advantage of fixing the devices is primarily structural. Nevertheless, the movable devices prove to have better aerodynamic effects. As a result, small aircrafts, which are not necessarily heavily loaded, do not have the need to adapt drastically their lift-to-drag ratio and
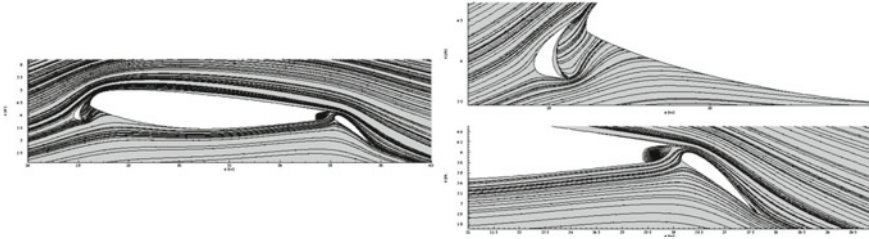
**Fig. 2** Streamlines over a wing section of the NASA's High-lift Common Research Model at angle of attack 8°. Upper right: zoom-in of the slat; lower right: zoom-in of the flap

therefore tend to use fixed devices. On the other hand, larger commercial aircrafts use the movable devices in order to adapt effectively for landing and takeoffs [5].

In this regard, various studies [2, 8] show that the best results are obtained when both leading- and trailing-edge devices are used. This is what it is usually referred to as the "configuration" or the "multi-element airfoils", which take advantage of both types of devices.

## 4 Physics of High-Lift Systems and Numerical Simulations

In order to understand the physical phenomena, the complex flows that take place over the wing have to be understood. Particularly in the case of high-lift systems and multi-element airfoils, this flow mixes subsonic and supersonic regimes. In 1975, Smith [2] published a large compendium of his aerodynamics lectures, where he explains the principles behind the aerodynamics of high-lift systems and provides clear insight into the fundamentals of multi-elements airfoil designs [2]. The importance of Smith's work as a baseline for the next generation of high-lift systems is the explanation of the principle that, as the pressure splits, the flow separation over different elements is suppressed, thus, increasing the lifting force. Understanding this basic phenomenon led to the consideration of a more complex issue, namely, the behavior of viscous effects.

The effect of high-lift systems on the flow is depicted in Figs. 2 and 3. The multi-element airfoil shown consists of the main airfoil, the Krueger flap leading-edge and trailing-edge flap. This is the configuration of the Common Research Model designed by NASA [6]. The streamlines show the flow attached to the airfoil and over both devices, i.e., the flap and the slat.

Figure 3 shows the development of the wake at various positions (15, 41, 68% and near the tip approx. 100%) over the wingspan and the effect of the trailing-edge flap delaying airflow detachment. One can observe at the root of the wing the possible interaction between the airfoil wake and the flap's boundary layer as the wake is large and turbulent. On the other hand, towards the wingtip, the wake is shorter.
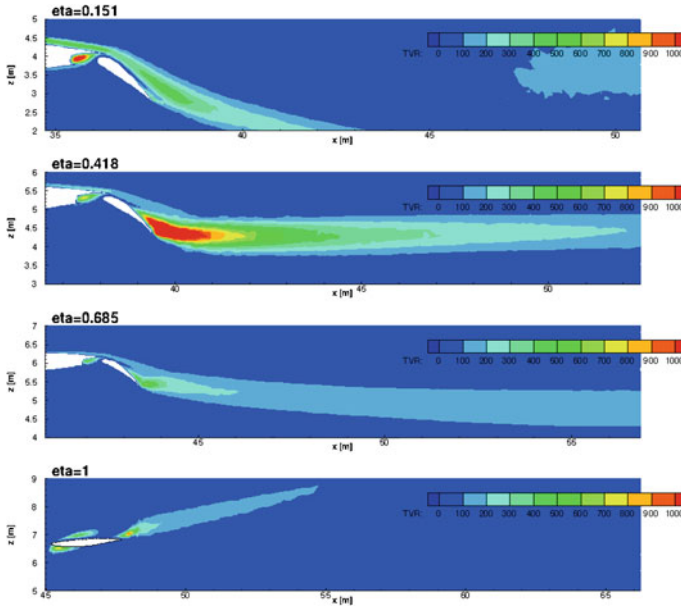
**Fig. 3** Turbulent viscosity ratio at four position over the wing span of the NASA's CRM at angle of attack 8°

Flow over high-lift systems is dominated by viscous effects due to the interaction between the boundary layer from one element and the turbulent wake induced by another. Meredith listed some of the viscous phenomena present in multi-elements airfoils [9]. Boundary-layer transition, viscous-wake interactions, boundary-layer interactions and flow separation, among others, still constitute challenging issues for CFD simulations and the aerospace industry.

Preceding the current series of workshops on the matter of high-lift systems that have been organized by the American Institute of Aeronautics and Astronautics (AIAA), the High-Lift Aerodynamics Conference held in Canada was one of the first scientific meeting where CFD showed its potential to accurately capture the flow physics by solving the Navier-Stokes equations. The goals of the High-lift Prediction Workshop series' remain similar, as it aims to improve the understanding of the physics underlying transport aircraft in high-lift stages by means of numerical computations. Additionally, it aims to assess the current CFD capabilities for predicting aerodynamic performance and to establish fundamental knowledge for numerical simulations.

During the past decade, the ability to design more efficient high-lift systems has increased. The main reason is the better understanding of the flow, thanks to the use of computational tools. However, there are still many complex issues to face, which make the simulation of aircraft by CFD computations a demanding process.

A comprehensive survey of CFD methods applied to the computation of high-lift configurations, given by Rumsey and Ying, established the challenges that CFD must confront nowadays [10]:

1. Quantify what is required to accurately predict flow fields near maximum lift, using 3D CFD. To do so, advances in CFD methods, such as adaptive grid techniques and quality 3D high-lift datasets, are needed.
2. The increased need to obtain more experimental database for CFD validation. This is especially important for the accurate definition of boundary conditions and for validation of the wide range of CFD codes.
3. Determine the cause of slat-wake mispredictions by RANS, whose causes could be related to poor modeling of transition effects, lack of unsteady effects, neglecting 3D effects and turbulence models not capturing the relevant physics of the flow.
4. Improve turbulent shear-stress predictions since they depend on the turbulence model employed. Since this relates to transition effects, the capability to accurately predict transition has to improve.

The aerospace engineering community has undertaken an effort to advance the issues listed above. Although the complexities inherent in high-lift systems remain and add a significant degree of uncertainty to the CFD computations, global variables like the surface-pressure distribution and skin-friction coefficient can be predicted with good accuracy.

More recently, in order to progress the state of the art in predicting high-lift flows, an international workshop series has been carried out. The First High-Lift Prediction Workshop (HiLiftPW-1), held in Chicago (2010), focused on the three-element NASA Trapezoidal Wing Configuration [11]. One of the main conclusions for this first version was the trend of CFD to underestimate the lift, drag and magnitude of the pitching moment [12]. The Second High-Lift Prediction Workshop (HiLiftPW-2), held in San Diego (2013), used the DLR-F11 three-element, wing-body model as the base geometry. This body was more representative of a transport aircraft configuration than the NASA Trapezoidal Wing, and there were available experimental data at low and high Reynolds numbers; this was the focus of this occurrence of the workshop. The ability to predict differences between low and high Reynolds numbers was observed in detail [13]. Likewise, the HiLiftPW-1 CFD results lacked consistency, but efforts to quantify and isolate possible causes were done, for example, to include a verification case and iterative convergence information as prerequisites for future workshops. The last occurrence, the Third High Lift Workshop (HiLiftPW-3), held in Denver (2017), posed two geometries: NASA's High-Lift Common Research Model and the Japan Aerospace Exploration Agency (JAXA) Standard Model (JSM). Among the main conclusions were: predicting flow near maximum lift is still challenging; some participants, codes or turbulence models get better agreement but there is not a clear explanation for this; finer grids are needed when flow is separated.

# References

1. Advisory Group for Aerospace Research and Development: High Lift Systems Aerodynamics. In: AGARD Conference Proceedings 515. Neuilly Sur Seine (1992)
2. Smith, A.M.O.: High-Lift aerodynamics. J. Aircr. **12**, 501–530 (1975)
3. Anderson, L.D.: Aircraft Performance and Design, p. 21. TATA McGrawHill (2010)
4. Rudolph, Peter K.C.: High lift systems on commercial subsonic airlines. In: NASA Contractor Report 4746. Seatle (1996)
5. Federal Aviation Administration, Chapter 6: Floght Controls, in Pilot's Handbook of Aeronautical Knowledge, pp. 6-1–6-12. Washington D.C. (2016)
6. Lacy, D., Sclafani, A.: Development of the high lift common research model (HL-CRM): a representative high lift configuration for transonic transport. In: AIAA SciTech Forum, 54th AIAA Aerospace Sciences Meeting, San Diego (2016)
7. Weich, F.E.: Preliminary Investigation of Modifications to Conventional Airplanes to give Nonstalling and short-landing Characteristics. National Advisory Committee for Aeronautics, Washington D.C. (1932)
8. Tinoco, E.N., Ball, D.N., Rice, F.A.: PAN AIR analysis of a transport high-lift configuration. J. Aircr. **24**, 181–187 (1987)
9. Meredit, P.T.: Viscous phenomena affecting high lift systems. In: Proceedings of the High Lift Systems and Suggestions for Further CFD Development, pp. 19.1–19-8. AGARD (1992)
10. Rumsey, C.L., Ying, S.X.: Prediction of high lift: review of present CFD capability. Prog. Aerosp. Sci. **38**, 145–180 (2002)
11. Slotnik, J.P., Hammon, J.A., Chaffin, M.: In Overview of the First AIAA CFD High Lift Prediction Workshop (Invited), AIAA paper 2011–862(2011)
12. Rumsey, C.L., Slotnik, J., Long, M., Stuever, R.A., Wayman, T.R.: Summary of the first AIAA CFD high lift prediction workshop. J. Aircr. **48**, 2068–2079 (2011)
13. Rumsey, C.L., Slotnik, J.P.: In Overview of the Second AIAA High Lift Prediction Workshop (Invited), AIAA paper (2013)
14. HiLiftPW Committee: Summary next steps and discussion. In: Third High Lift Prediction Workshop, AIAA (2017) (cited 24 July 2017). https://hiliftpw.larc.nasa.gov/

# Grid Generation About High-Lift Wing Configurations

**Nirajan Adhikari and D. Stephen Nichols**

**Abstract** The current guidelines provided by the 3rd AIAA CFD High Lift Prediction Workshop for building unstructured meshes representing high-lift wing configurations are demonstrated and discussed. Specifically, Pointwise grid generation software is used to generate general multi-element unstructured grids about the NASA High Lift Common Research Model and the Japanese Aerospace Exploration Agency Standard Model with and without nacelles and pylons. Several modifications to the guidelines that enhance grid quality are presented. Additionally, the user-defined parameters within Pointwise that govern the mesh generation process are reviewed in detail.

## 1 Introduction

Quality mesh generation is vital for accurate simulations. As the complexity of the geometry and the resulting flow field increases, building a grid that enables a flow solver to accurately capture the flow physics becomes increasingly challenging. High-lift configurations are difficult to examine because of their geometric and flow-field complexity. Extended slats and flaps along with their respective recessed wing coves require careful grid generation to capture the complex flow generated in these regions. The wing-fuselage, pylon-wing, and nacelle-pylon intersections induce strong horseshoe vortices [3] and are common locations of boundary-layer instabilities due to the strong vortical systems. The use of blunt trailing edges for the wings and their naturally fine grid spacing demands high-point density on all attached surfaces to maintain high grid quality and solution fidelity [11]. Each of these examples demonstrates the strong coupling of grid generation and the flow solver present in modern Computational Fluid Dynamics (CFD).

---

N. Adhikari · D. S. Nichols (✉)
Aerospace Engineering, Auburn University, Auburn, AL, USA
e-mail: stephen.nichols@auburn.edu

N. Adhikari
e-mail: nza0031@tigermail.auburn.edu

9

Grid generation is a challenging and time consuming part of a CFD study and largely influences the overall success of the study. Initially, a Computer-Aided Design (CAD) model is built to represent a real-life geometry, and this CAD model is further approximated during the mesh-generation process to build a valid, volumetric grid. Assuming the availability of robust and efficient CFD algorithms, the generation of high-quality grids leads to accurate solutions. General guidelines exist in all areas of CFD, and they typically address minimum requirements to achieve a certain level of solution fidelity. This work demonstrates the application of the grid-generation guidelines provided by the 3rd AIAA CFD High Lift Prediction Workshop (HiLiftPW3) to building grids about the NASA High Lift Common Research Model (HL-CRM) and the Japanese Aerospace Exploration Agency (JAXA) Standard Model (JSM). Although other mesh-generation packages exist, this work will focus on using Pointwise [10] grid-generation software to build the high-lift wing configuration meshes. Keep in mind that the strategies discussed in the following sections are generally applicable to other mesh-generation packages as well. In this work, preparing the CAD model surfaces, applying the mesh generation guidelines, generating the surface and volume mesh and specifying useful Pointwise parameters are discussed. During the course of building the meshes, several modifications to the guidelines to increase the grid quality were necessary, and these modifications are presented and justified.

## 2   CAD Model

The CAD models for HL-CRM and JSM are provided by the HiLiftPW3 committee in multiple formats [1], and Pointwise [10] grid generation software supports all of these CAD formats. However, readers should be warned that CAD models can be quite complex, and, depending upon the CAD package and method of generating the CAD model, grid generation software such as Pointwise may not be able to use a specific CAD file. Therefore, having multiple formats from which to choose is highly desirable and offers the user the flexibility to choose the optimal CAD file for a given software package. The authors are aware of no issues regarding the various formats offered by the HiLiftPW3 committee and chose the IGS format simply because those CAD files were successfully imported into Pointwise on the first attempt with no errors. Consequently, no attempts were made with the other formats. It should be noted that although the IGS (also known as IGES) format is still popular, the IGS standard was last updated in 1996 to Version 5.3 [2] and is no longer being actively developed. As a result, it is quite antiquated when compared to a modern standard such as STP (also known as STEP) [7] which is being actively developed to contain more information about the geometry and model [4, 9]. Future efforts will use newer formats such as the STP format when possible, and readers are encouraged to do the same.

The models used in this work consist of the HL-CRM with partial gaps between flap elements (Fig. 1), the JSM without a nacelle/pylon (N/P) assembly (Fig. 2) and

**Fig. 1** HL-CRM CAD model



**Fig. 2** JSM CAD model without nacelle
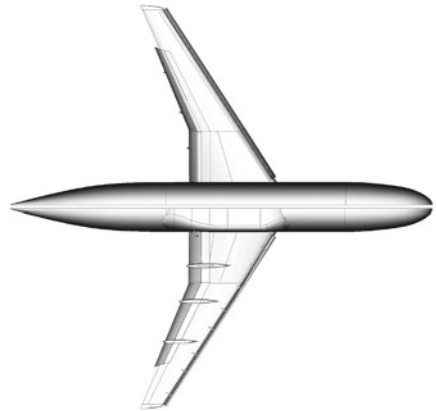


**Fig. 3** JSM CAD model with nacelle
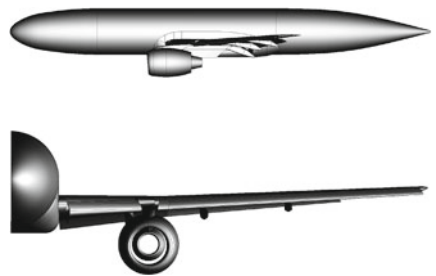


the JSM with N/P assembly (Fig. 3). The HL-CRM model does not have any support brackets while the JSM models have support brackets in both configurations. Further, the deployed slats and flaps are identical for both JSM configurations.

The CAD models include numerous trim information and a number of quilt surfaces that make this high-lift configuration a complex geometry on which to create a mesh. The model has to be a water-tight model in order to generate a volume grid, and

**Fig. 4** Single surface on the
HL-CRM fuselage



this is generally achieved by assembling multiple models into a single model. The tolerance for model and quilt assembly is set to a value smaller than the minimum edge length associated with the surface grid so that the mesh surface is properly defined in the region where surface intersection occurs. After assembling the model, various quilt surfaces are combined to minimize the total number of quilts associated with the geometry in order to facilitate surface mesh generation. The quilts are combined in such a way that a single mesh surface can be generated between surfaces with similar surface topography as shown in Fig. 4 where different quilts representing the fuselage are assembled to create a single quilt surface.

## 3 Mesh Generation Guidelines

The HiLiftPW3 committee provided a basic set of mesh generation guidelines as an attempt to maintain consistency among the workshop participants. Since these guidelines provide a list of current best practices, they are closely followed from the grid-generation process. The grid resolution is categorized into coarse-, medium- and fine-grid density levels, and the meshing guidelines are provided for the medium-level grid. Proper scaling to coarse and fine grids are requested such that the grid size grow approximately three times in size between the various grid levels for the grid convergence study. The meshing guidelines are as follows:

1. The farfield boundary should be located at least 100 reference chord lengths ($C_{REF}$) away from the aircraft for all grid levels.
2. Element size near body nose and tail should be at least ∼1.0% $C_{REF}$.
3. Chordwise spacing at the leading edge (LE) and the trailing edge (TE) should be ∼0.1% local device chord (slat-element chord for slat grid, wing-element chord for wing grid, and flap-element chord for flap grid).
4. Spanwise spacing at root and tip to be ∼0.1% semispan.
5. Grid spacing normal to symmetry plane to be considerably larger than viscous wall spacing.

The HL-CRM model was built using a full-scale mean aerodynamic chord (MAC) of 275.8 in. and a wing semi-span of 1156.75 in. while the JSM models were built with a model-scale MAC of 529.2 mm and a wing semi-span of 2300.0 mm.

In addition, the viscous wall spacing and the number of points for trailing edges are also specified. The viscous spacing and viscous spacing growth rate play an important role in the proper resolution of a boundary layer which is paramount to the calculation of aerodynamic forces on any surface. The viscous spacing is defined based on a non-dimensional normal distance to a wall, $Y^+$ value, which is defined as:

**Table 1** $Y^+$ values and corresponding wall spacings for various cases

| Model | Grid resolution level | $Y^+$ value | $\Delta y$ | Number of points on TE |
|---|---|---|---|---|
| HL-CRM | Coarse | 1.0 | 0.00175 in | 5 |
| | Medium | 2/3 | 0.00117 in | 9 |
| | Fine | 4/9 | 0.00078 in | 13 |
| JAXA JSM | Coarse | 1.0 | 0.00545 mm | 5 |
| | Medium | 2/3 | 0.00363 mm | 9 |
| | Fine | 4/9 | 0.00242 mm | 13 |

$$Y^+ = \frac{u^*y}{\nu} \tag{1}$$

where $u^*$ is the friction velocity at the nearest wall, $y$ is the distance to the nearest wall, and $\nu$ is the local kinematic viscosity of the fluid. The height of the first mesh cell (initial wall spacing) perpendicular to the no-slip wall boundary is calculated using Eq. 1. The $Y^+$ value will ensure that there are at least a few points present in the viscous sub-layer region of a turbulent boundary layer. For the grid convergence study, $Y^+$ dictates the grid resolution level. Since $Y^+$ is dependent on the friction velocity, which is unknown before solving the flow, it involves an iterative approach to obtain the required $Y^+$. For simplicity, $Y^+$ and the corresponding wall spacing are provided by the HiLiftPW3 committee as part of the meshing guidelines. The $Y^+$, the corresponding initial wall spacing ($\Delta y$), and the required number of points in the trailing edges are tabulated in Table 1. More detail regarding the meshing guidelines is present on the HiLiftPW3 website [1]. The grids created for this research conforms with most of the provided guidelines. However, some deviations were unavoidable in order to create high-quality meshes. These deviations from the meshing guidelines are explained in detail in Sect. 4.3.

## 4 Surface Mesh Generation

In order to minimize the number of mesh surfaces (domains in Pointwise), multiple quilts are assembled into a single database, and the mesh surfaces are then created on this single database. However, during the initial quilt assembly, one of the quilts (one of the surfaces in a fuselage-wing fairing) in the fuselage of the NASA HL-CRM model could not be attached to its neighboring quilts (evident in Fig. 5) because this surface had overlapping boundaries with its neighboring surfaces. Similar concerns regarding this invalid surface are mentioned by other researchers [6] who coarsened the mesh size in the invalid surfaces to avoid problems with the mesh generation. Alternatively, surface trimming usually repairs such overlapping boundaries, but the trimming process did not help in this case. Consequently, a separate domain is created

on the faulty quilt, and that domain is subsequently combined with its neighboring domains by merging connectors with the neighboring domains. As the domains are associated with a model (quilts) and the cell size on the domain is greater than the overlapping length, the combined domain produced uniform elements without any discontinuity.

Figures 5, 6, 7, and 8 show the subsequent steps leading to a combined domain from two overlapping domains. Since the domains are created on different database entities, there are overlapping connectors on domain boundaries, and these overlapping connectors are merged into a common connector to achieve a water-tight

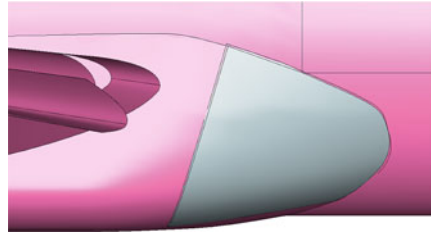**Fig. 5** Overlapping quilts



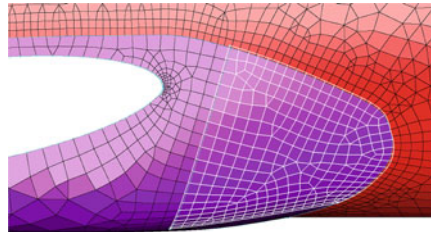**Fig. 6** Non-matching edges on the surface domains caused by the overlapping quilts



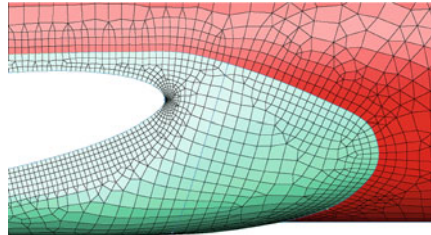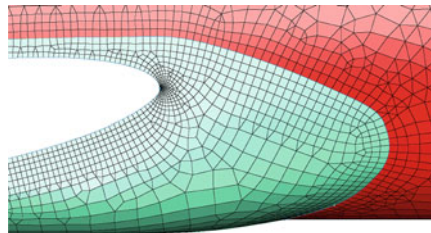**Fig. 7** Reconstructed surface with matching edges



**Fig. 8** Two domains combined into a single domain and regenerated on the surface

surface. Although the CAD files of the HL-CRM that are currently available on the HiLiftPW3 [1] website appear to have been corrected, these instructions have been included to demonstrate the process for repair overlapping quilts and to build a valid, water-tight geometry.

A fixed number of points are required on the trailing edges, so structured grids are created along all trailing edges and are diagonalized in order to convert them into unstructured grids. Also, structured grids are created and diagonalized at various locations like the wing tip in the HL-CRM and the nacelle and filleted surfaces of support brackets in the JSM to get uniform point spacing which otherwise is difficult to achieve using unstructured meshes alone.

To resolve the high-curvature geometry near the leading edges and trailing edges, high-aspect-ratio anisotropic elements (known as T-Rex elements in Pointwise) are used with the chord-wise spacing specified by the meshing guidelines (0.1% local device chord). Since the chord length for each element varies with the wing span, minimum chord is used to determine the spacing on the leading and trailing edges. An alternative approach [5] is to use the average chord for leading and trailing edge spacings. However, using the average chord length leads to low-mesh resolution when the local chord length is smaller than the average value. Thus, the minimum chord length is used for this work. The minimum chord among the outboard and the inboard flap is used on both flaps in order to maintain consistent grid spacing. Further, using a single spacing among different chord locations creates a uniform grid across the span and avoids the abrupt transition at the intersection of two different elements. Also, using the same spacing among two separate flaps facilitates the uniform matching of grid size (for better mesh quality) in the gap (fully gapped configuration) between the flaps while creating the volume grid.

The chord-wise point spacing from the leading edge increases with a fixed growth rate up to a specified number of layers until the anisotropic element size matches the local, unstructured, isotropic element size. For the wing surfaces, the maximum allowed spacing for an unstructured element is specified to be ∼1% MAC. The resolution of the high curvature near the leading edge and trailing edge of the wing of the JSM using T-Rex layers is shown in Fig. 9. Throughout the mesh-generation
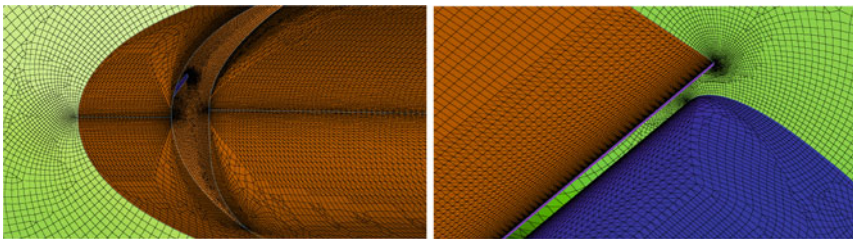


**Fig. 9** High-aspect-ratio anisotropic layers to resolve high curvature elements on the leading edge of a wing (left) and the trailing edge of a wing (right)

process, high-aspect- ratio anisotropic elements are used whenever the unstructured isotropic elements alone cannot resolve the geometry to a desirable degree.

The surface mesh generated for this research used the "Triangles and Quads" Pointwise option to create quadrilateral dominant surfaces that contain a mix of triangular and quadrilateral elements. The quadrilateral surface elements enable the creation of hexahedral elements in portions of the viscous region while creating the volume grid. Hexahedral elements are generally the least dissipative, unstructured element type and are consequently desired for the utmost in accuracy [8]. Also, the "Advancing Front Ortho" algorithm was used to generate surface meshes that better parallel features of the geometry, such as panel intersections, and a "Boundary Decay" of 0.8 was used to control the growth of the interior elements of each surface.

## 4.1  Farfield and Symmetry Plane

After the generation of the surface grid on the aircraft body, the farfield domain is created according to the specified guidelines, which require the farfield to be $\sim$100 $C_{REF}$ away from the aircraft geometry. The farfield domain is a hemisphere that has a uniform distance from the center of the aircraft body. Finally, since all the research models are half-span models, a symmetry plane is needed to ensure a water-tight boundary for the fluid domain.

## 4.2  Grid Quality

Volume grid generation is a computationally demanding process and can take multiple iterations to produce a high-quality grid. So, it is necessary to check the quality of the surface grid in order to create a high-quality volume grid in a minimum number of iterations. There is no absolute definition of a high-quality grid. However, a high-quality grid can be defined as a grid that produces a desirable solution with maximum accuracy while utilizing minimum computational cost and time. Most of the time, a grid which has less skewness fulfills the grid-quality criteria, but the acceptable skewness value is solver dependent and varies from one solver to another. A few of the most important parameters that dictate the quality of a grid are: *area ratio, minimum included angle, maximum included angle and aspect ratio*.

The area ratio is the ratio of areas between the neighboring elements. The volume grid is generated by inserting a point normal to the surface at a specified distance that increases with a fixed growth rate, so a larger area will grow faster than a smaller area and can create a skewed element in between them. Figure 10 illustrates two areas that are subject to highly skewed surface elements. Normally, for a domain with tetrahedral elements, the area ratio up to three–five is reasonable, while in a quad dominant domain, the area ratio up to six–ten is desired to prevent high skewness. However, it is not always possible to restrict the area ratio to a recommended range.

**Fig. 10** Possible locations for highly skewed surface elements when using the spacing provided by the meshing guidelines (Trim surface of the WUSS and the trailing edges)
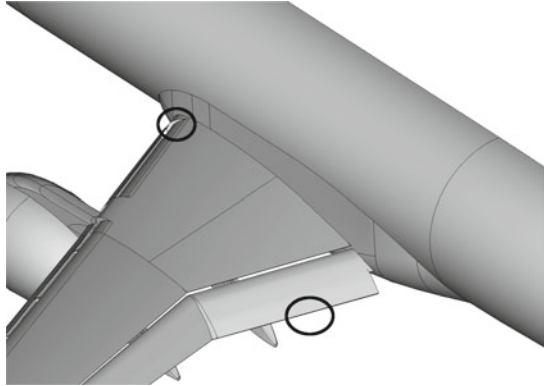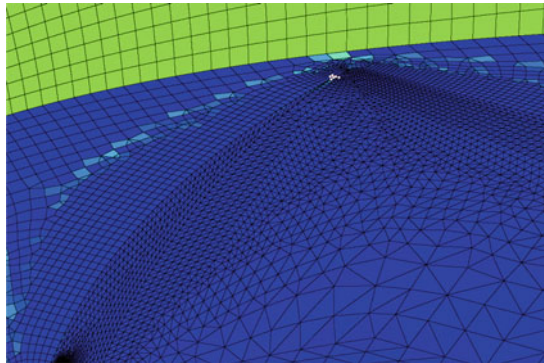


**Fig. 11** High area ratio in the trim surface location of the WUSS that is circled in Fig. 10



For example, the area ratio is usually high, around 30, in the corners of the trim surface of the Wing Under Slat Surface (WUSS) as demonstrated in Fig. 11 for the JSM. In such circumstances, during volume grid generation, if an anisotropic elemental normal to the surface creates highly skewed elements, the anisotropic layer growth stops locally, and a tetrahedral element is placed to improve skewness.

The minimum- and maximum-included angles are the minimum angle and the maximum angle in a grid element (2D or 3D element) respectively. For domains (surface grid), the maximum included angle is usually kept below 150° in order to prevent high skewness. On the other hand, the acceptable minimum included angle is solver dependent, but a value greater than 2° is usually desired. However, it can be extremely difficult to achieve a better minimum angle in the sharp corners. The trim locations of the WUSS are the regions where this quality criteria is usually violated (Fig. 10). If the angles are extremely small (below or close to 1°), the connectors can be split at some location and then recombined to a single connector at the corner to improve the minimum-included angle. One such improvement in minimum-included angle by this technique is evident in Fig. 12 where the corner has a single connector which is obtained by merging two split connectors.
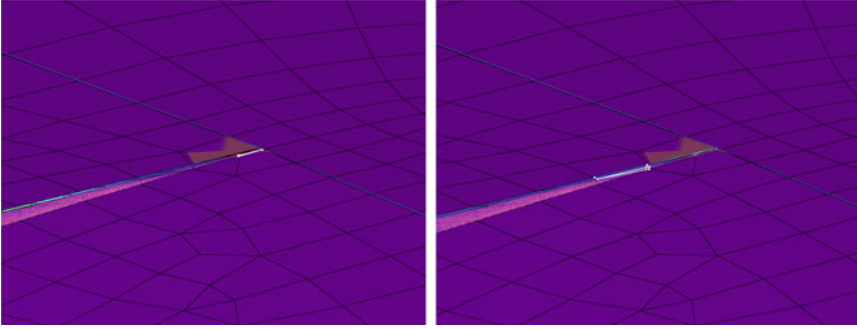
**Fig. 12** Improvement in minimum-included angle from 1.6° (left) to 2.5° (right) by joining connectors at the corners of WUSS

The aspect ratio is an additional quality criteria to examine and is defined as the ratio between the average length to the average width of a quadrilateral or as the ratio of the long edge to the short edge of a triangle. The aspect ratio directly effects the skewness of grid elements that are connected to one another. Usually, a surface element with an aspect ratio of 50 creates a volumetric element with a large interior angle of $\sim$178° which tends to reduce the grid quality. However, the aspect ratio can be controlled by carefully matching the edge (a connector in Pointwise) spacings on a domain to alleviate skewness in the volumetric grid. For example, in the slat element of the HL-CRM, the trailing edge has nine points, such that the average point spacing is $\Delta S \sim 0.012$ in., while the span of the slat is around 1,000 in. In order to limit the aspect ratio below 50, roughly 1,700 (an approximation of $1,000/(50 * 0.012)$) points are required along the span of the slat. This requirement can be somewhat restrictive from a computational point of view. In such cases, a high-aspect ratio may be accepted, and the skewness monitored during the generation of the volume mesh.

## 4.3 Deviation from HiLiftPW3 Meshing Guidelines

In order to create high-quality grids, some deviations from the provided meshing guidelines were unavoidable. The guidelines require a fixed number of points at the trailing edges (nine points for a medium grid level) and also provide a spacing for the chordwise elements of the upper and lower surfaces at the trailing edges. For the medium HL-CRM grid, this is $\Delta S \sim 0.012$ in. on the blunt trailing edge of the wing. However, the chordwise spacing for the wing tip is 0.1 in. (0.1% of local chord of 100 in.). This large variation in size between two adjacent elements is not ideal in a critical geometric feature like trailing edges. To minimize the area variations across the trailing edge, the chordwise spacing for the trailing edge of the upper surface is set to 0.018 in. Figure 13 shows the area ratio with both the spacing provided
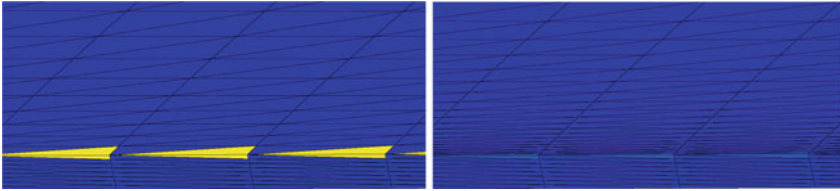
**Fig. 13** Improved area ratio at the trailing edge of the HL-CRM wing tip by refining the spacing prescribed by the meshing guidelines

by the meshing guidelines (left image) and the refined spacing (right image). The refined spacing clearly improves the area ratio. This approach is applied throughout the mesh-generation process for all other elements and configurations.

The meshing guidelines also provide the spanwise spacing at the root and tip of each element (wing, slat and flaps) based on the span of the element. The area ratio at the root and tip of the HL-CRM elements built according to the spacing specified by the meshing guidelines violates the acceptable quality criteria. The problem is even more pronounced in the slat elements shown in Fig. 14. Various adjustments in the spacing are done to bring the area ratio to an acceptable range in all three configurations (HL-CRM, JSM Nacelle OFF, and JSM Nacelle ON). The change in spacing is not consistent throughout each grid. Specifically, different spacings are used at the leading and trailing edges in a single element, and the spacing also varies from root to tip. For example, adjusted spacings in the HL-CRM are tabulated in the Table 2.
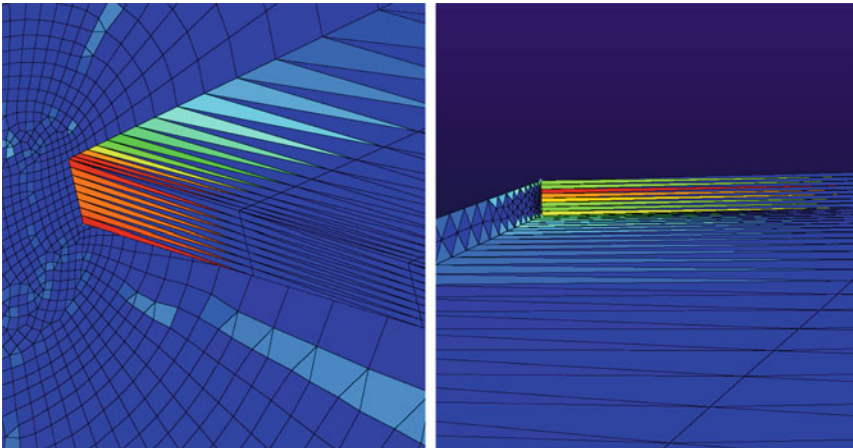


**Fig. 14** Large area ratio at the trailing edges of the HL-CRM wing root (left) and slat (right) using the spanwise spacing prescribed by the meshing guidelines

**Table 2** Adjusted spanwise spacing at various locations in the HL-CRM

| Model | Element | Location | Meshing guideline spacing (in.) | Adjusted spacing (in.) |
|---|---|---|---|---|
| HL-CRM (Medium) | Wing root | LE | 1.04 | 0.50 |
| | | TE | 1.04 | 0.20 |
| | Wing tip | LE | 1.04 | 0.05 |
| | | TE | 1.04 | 0.10 |
| | Slat | LE | 0.97 | 0.08 |
| | | TE | 0.97 | 0.03 |
| | Flap | LE | 0.70 | 0.08 |
| | | TE | 0.70 | 0.08 |
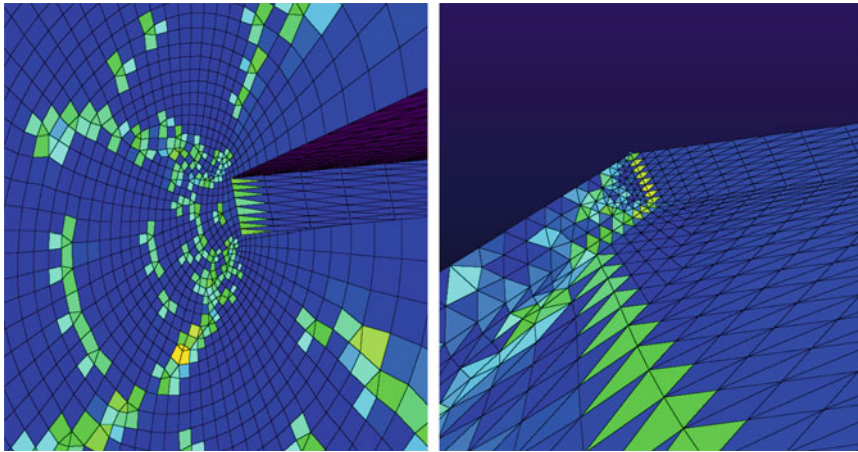


**Fig. 15** Spanwise spacing adjusted to achieve a better area ratio at the trailing edges of the HL-CRM wing root (left) and slat (right)

Improvements in the area ratio by adjusting the spanwise spacings on the HL-CRM is shown in Fig. 15 for various locations. Similar modifications to the chordwise and spanwise spacing in the HL-CRM grid were used by workshop organizers [11] during the process of generating the grids for the workshop participants.

Another deviation from the meshing guidelines is found on the trailing edge of the wing tip for the HL-CRM where the required number of points is nine, but, in order to preserve the curvature of the wing tip, the total point count is increased to 15. Furthermore, to achieve better control of the surface mesh while at the same time reducing the number of points, a structured grid is created and diagonalized on the wing-tip domain. This approach produced uniform mesh growth across the radial direction of the wing tip along the length of its chord and reduced the total number of points on that domain when compared to a fully unstructured surface mesh. The

**Fig. 16** Trailing edge of the wing tip in HL-CRM using nine points prescribed by the meshing guidelines (left) and using 15 points to preserve the curvature of the geometry (right)
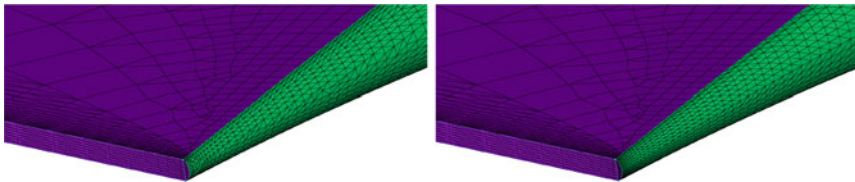
reduction in the number of points on the wing-tip domain can be seen in Fig. 16 where the unstructured anisotropic layers (left image) generate a greater number of nodes than the diagonalized structured grid (right image). Also notice the disparity in area ratio along the wing's upper surface near the trailing edge. Using an approach on the upper- and lower-wing surfaces that is similar to the technique applied to the wing tip and trailing edge can limit problems with the area ratio in this region but will increase the number of points on the wing by a considerable amount.

## 5  Volume Grid Generation

After the surfaces that act as the boundary for the computational domain have been defined, the volume is populated using isotropic and anisotropic elements. Volume-grid generation is carried out by generating anisotropic elements with a specified initial distance and a fixed growth rate followed by populating the remaining portion of the fluid domain with isotropic tetrahedral elements.

The volume elements in the anisotropic layers (Pointwise T-Rex layers) are created by placing a point normal to the surface at a specified distance (distance dictated by $Y^+$ value as in Table 1) from the wall (domain of aircraft body) and the spacing continues to increase with a specified growth rate until the maximum layers are reached. The growth rate for the viscous layers are specific for each grid-resolution level. The coarse grid has a growth rate of 1.25, the medium grid has a growth rate of 1.16, and the fine grid has a growth rate of 1.10. The meshing guidelines require the growth rate be no more than 1.25 for a coarse grid ($GR_1$) and scaled appropriately to refine grid levels based on the following expression:

$$\text{Growth Rate} = GR_1^{1/F^n} \tag{2}$$

where $F$ is approximately equal to 1.5 and $n = 1$ and 2 for the medium and fine grid levels respectively. The growing of T-Rex layers is locally stopped in locations where the created elements violate the specified skewness criteria, and tetrahedral elements are placed instead. Skewness is based on the maximum included angle of an element and for T-Rex layers, maximum included angle is set to 175° so that

any T-Rex element having maximum included angle greater than 175° will stop the
growth of T-Rex layers.

The remaining portion of the fluid domain is populated using isotropic tetrahedral
elements with a "Boundary Decay" of 0.8 to control the growth rate of the isotropic
elements away from the aircraft. However, the HiLiftPW3 committee required tighter
mesh spacing in the wakes of the slats, wing and flaps in order to capture the interac-
tion of these wakes with the downstream geometry and flow field. Therefore, the size
of the isotropic elements around the wing is alternatively controlled by defining a
region where the size of tetrahedral elements is fixed to a specified value. This region
is defined by the Pointwise "Source" feature which forms an open quasi-boundary
around a region and controls the mesh size only within that boundary. Figure 17
shows one such predefined region around the wing and nacelle of the JSM which
prescribes an 8-mm tetrahedral spacing within the region. By controlling the element
size in this region, better resolution of the flow features near the wing is achieved.
Figure 18 shows a general, multi-element grid built for the JSM with N/P with four
different element types; hexahedrals in blue, prisms in green, pyramids in yellow,
and tetrahedrals in red. The effects of the "Source" feature are readily apparent in
the uniformly packed tetrahedral region. The total node and element count for the
various grid configurations presented in this work are tabulated in Table 3.

The overall quality of the grids created for this research is quite high. The grids
are subjected to multiple iterations in order to keep the maximum included angle
less than 178°. The maximum included angle is significant because, once it reaches
180°, the element is flat and has no volume. Thus, minimizing this angle is critical
for grid quality. The HL-CRM grids presented in this work have maximum-included
angles below 177° for all grid levels (medium, coarse and fine). The grid resolution
of the medium HL-CRM grid at various span locations is shown in Figs. 19, 20, 21,
22, 23, 24, 25, 26 and 26.

However, the JSM configurations proved to be more difficult. After many iter-
ations, there remain a few highly skewed elements in the JSM configurations; 17
elements in the JSM without N/P configuration and 23 elements in the JSM with
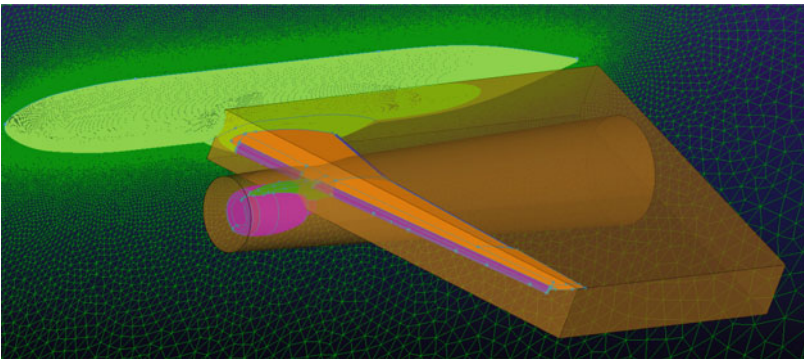


**Fig. 17** Pointwise "Source" feature for better control of size of isotropic elements
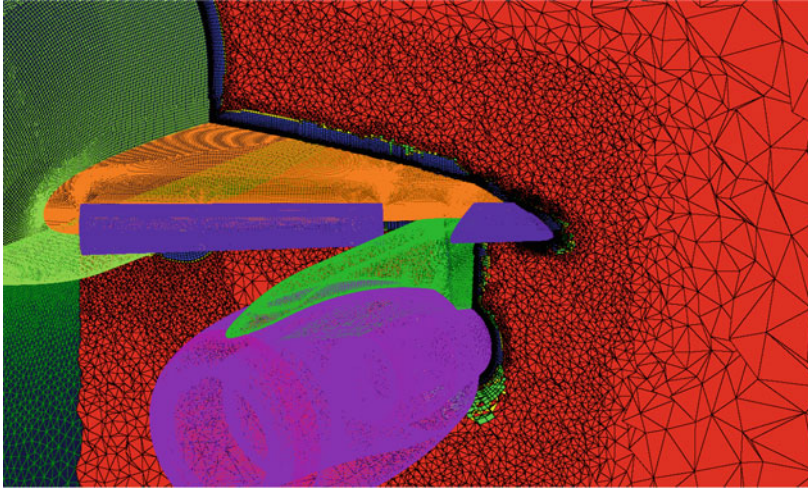
**Fig. 18** Multi-element JSM grid with hexahedral, prism, pyramid and tetrahedral elements

**Table 3** Total number of nodes and elements for the different model configurations

| Model | Grid Level | Nodes | Hexahedrals | Prisms | Pyramids | Tetrahedrals |
|---|---|---|---|---|---|---|
| HL-CRM | Coarse | 13,758,812 | 9,579,038 | 1,706,194 | 2,657,235 | 1,335,4087 |
|  | Medium | 42,422,679 | 32,293,629 | 5,304,366 | 5,698,791 | 30,733,420 |
|  | Fine | 117,586,322 | 96,656,886 | 9,201,914 | 10,380,628 | 72,395,548 |
| JSM (OFF) | Medium | 43,989,123 | 33,600,484 | 3,959,730 | 5,959,730 | 35,667,103 |
| JSM (ON) | Medium | 54,097,064 | 42,367,255 | 4,735,191 | 7,581,223 | 37,495,618 |

**Fig. 19** HL-CRM grid at
$Y = 174.5$ in.
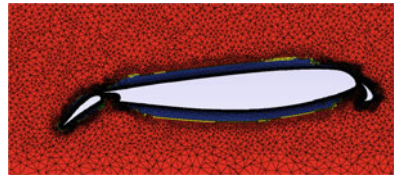


N/P configuration have maximum-included angles greater than 178°. The skewed elements reside either in the corners of the WUSS region or near the sharp edges of the slats, wing and flaps. The development of grid smoothing software either as a stand-alone package or as a tool/plug-in which effectively minimizes these maximum included angles needs to be a priority.

**Fig. 20** HL-CRM grid at
$Y = 277.5$ in.



**Fig. 21** HL-CRM grid at
$Y = 380.5$ in.



**Fig. 22** HL-CRM grid at
$Y = 483.5$ in.



**Fig. 23** HL-CRM grid at
$Y = 638$ in.



**Fig. 24** HL-CRM grid at
$Y = 792.5$ in.



**Fig. 25** HL-CRM grid at
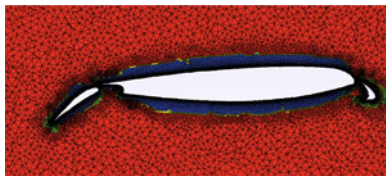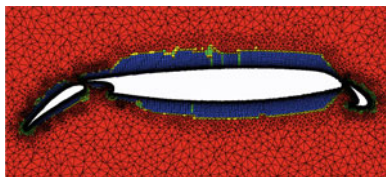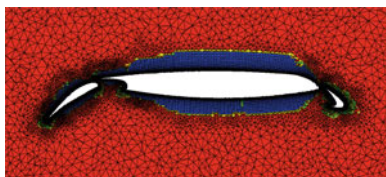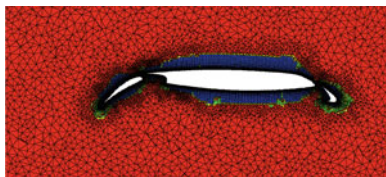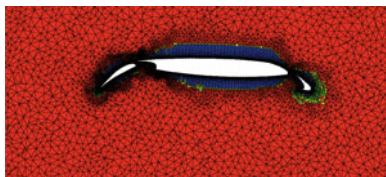$Y = 947$ in.
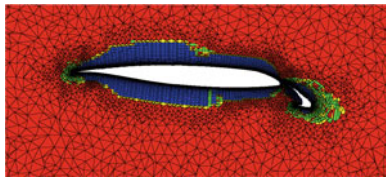
**Fig. 26** HL-CRM grid at
$Y = 1050$ in.
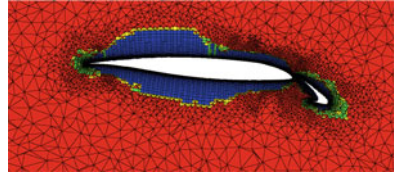


## 6 Final Remarks

At its core, mesh generation is a challenging endeavor. Regardless of the chosen flow solver, it is impossible to get a quality solution without a quality grid. Mesh generation for high-lift wing configurations is further complicated by their complex geometries and intricate flow fields. Using the current "best-practices" guidelines specified by the HiLiftPW3 committee, Pointwise mesh-generation software successfully built high-quality grids for the HL-CRM and JSM models. Although this work deals specifically with Pointwise, the strategies used in this work can be applied with other mesh- generation packages.

Although many improvements have been made over the years, grid generation remains a tedious, hands-on process. In particular, maximum- and minimum-included angles were difficult to manage around sharp edges, in the WUSS region, and at the fuselage-wing, the wing-pylon and the pylon-nacelle intersections. Tools which automatically control the maximum- and minimum-included angles should be standard practice in mesh-generation packages. Much time and effort was spent repeatedly adjusting parameters and building grids only to find another poorly built element. As long as proper meshing guidelines are followed, an automated process to control these extreme angles around complex geometries such as high-lift configurations has the potential to reduce the time required for mesh generation while at the same time providing better quality grids.

## References

1. 3rd AIAA CFD High Lift Prediction Workshop. https://hiliftpw.larc.nasa.gov
2. ANSI, USPro: Initial Graphics Exchange Specification IGES 5.3. Technical Report Formerly ANS US PRO/IPO-100-1996, Trident Research Center, Suite 204, 5300 International Blvd, N. Charleston, SC 29418 (1996)
3. Baker, C.: The laminar horseshoe vortex. J. Fluid Mech. **95**, 347–367 (1979)
4. Brown, C.: STEP files versus IGES files. https://www.cadlinecommunity.co.uk/hc/en-us/articles/115000846485-STEP-Files-vs-IGES-Files

5. Chan, W.M.: Best practices on overset structured mesh generation for the high-lift crm geometry. In: 55th AIAA Aerospace Sciences Meeting, AIAA Paper 2017–0362. Grapevine, Texas (2017)
6. Dey, S., Aubry, R., Karamete, B.K., Mestreau, E.L., Dean, J.L.: Mesh generation for high-lift aircraft geometry configurations. In: 55th AIAA Aerospace Sciences Meeting, AIAA Paper 2017–0364. Grapevine, Texas (2017)
7. ISO: Industrial automation systems and integration—Product data representation and exchange—Part 242: application protocol: managed model-based 3D engineering. Technical Report No. ISO 10303-242:2014(E), ISO (2014)
8. Karman, S., Wooden, P.: CFD modeling of F-35 using hybrid unstructured meshes. In: 19th AIAA Computational Fluid Dynamics, AIAA Paper 2009–3662, 22–25 June 2009. San Antonio, Texas (2009)
9. Lopategui, E.: It's time to get over IGES. http://blog.grabcad.com/blog/2014/10/14/get-over-iges/
10. Pointwise: Version 18.0 R1. http://www.pointwise.com
11. Woeber, C.D., Gantt, E.J.S., Wyman, N.J.: Mesh generation for the nasa high lift common research model (hl-crm). In: 55th AIAA Aerospace Sciences Meeting, AIAA Paper 2017–0363. Grapevine, Texas (2017)

# Incompressible Solutions About High-Lift Wing Configurations

**Nirajan Adhikari and D. Stephen Nichols**

**Abstract** Accurately predicting the performance of high-lift wing configurations with Computational Fluid Dynamics is an active area of research for academia and industry alike. The compressible Navier–Stokes equations are usually used in these studies to predict the complex flow field generated by high lift wing configurations. However, since these configurations are applied in low-speed conditions where $Mach \leq 0.2$, the compressible equations can exhibit some numerical stiffness caused by the quasi-incompressible nature of air under these conditions. Instead of using preconditioned compressible equations to alleviate these numerical issues, this work proposes the use of the incompressible Navier–Stokes equations to predict these flow fields. Specifically, the incompressible solutions about the Japanese Aerospace Exploration Agency Standard Model configuration with and without nacelles and pylons are compared with experiment at multiple angles of attack to demonstrate the effectiveness of this approach.

## 1 Introduction

The purpose of this study is to explore the capabilities of modern Computational Fluid Dynamics (CFD) technology to predict the flow about typical high-lift wing configurations. Since air is a highly compressible fluid, the compressible Navier–Stokes equations are normally used in these studies. However, high-lift configurations are applied at low $Mach$ numbers, and the compressible equations exhibit increasing difficulties during the solution process [4] as $Mach$ number drops below 0.2. Although various opinions exist, it is generally accepted that flows below $Mach = 0.3$ can

N. Adhikari · D. S. Nichols (✉)
Auburn University, Auburn, AL, USA
e-mail: stephen.nichols@auburn.edu

N. Adhikari
e-mail: nza0031@tigermail.auburn.edu

be considered incompressible in most situations [2]. Since the compressible governing equations are strongly linked by density, simulations for low-speed flows are adversely affected by changes in density when the density should be relatively constant. This situation is widely recognized [19] for flows below $Mach = 0.1$, and remnants of this numerical stiffness can be identified at $Mach = 0.2$ when small density variations can be expected but larger changes may be realized [14]. Several preconditioning methods [4, 7, 22] exist to address these issues with the compressible equations, and each method offers varying degrees of success depending upon the case [8].

High-lift configurations are particularly difficult to examine because of their geometric complexity and the intricacy of the resulting flow field. Extended slats and flaps, along with their respective recessed wing coves as well as engine nacelles and pylons require careful grid generation to, capture the complex flow generated in these regions. Both the sharp edges of the geometry and the recessed areas shielded by geometry typically generate strong turbulent responses that are ultimately transported by the flow and greatly affect the downstream flow field. These turbulent features oftentimes exaggerate the numerical stiffness of the compressible equations for low-speed flows [14] by dropping the density along with the pressure as more mass is transported out of the volumes than can be replaced. Further, stagnation points can elevate density along with pressure as mass is collected faster then it can be removed at these locations. These circumstances are obviously problematic for quasi-incompressible flows and can lead to pressures that don't reach the expected extreme values at the vortex cores or at the stagnation points. Furthermore, momentum, as well as internal and total energy, also realize the effects of these density variations. Common remedies for the standard compressible equations in these cases include dropping the CFL and increasing the grid-point density in these regions, and these remedies generally work well for modern flow solvers for $Mach > 0.1$. The more successful preconditioning methods condition the density and pressure to maintain entropy at low speeds and function quite well at extremely low $Mach$ numbers [8]. However, a logical way to avoid these numerical issues with density is to use the incompressible Navier–Stokes equations for these low-speed simulations.

This work will demonstrate the benefit of using a purely incompressible flow solver to predict the flow field about high-lift configurations at $Mach = 0.174$. This approach removes all unwanted density variations from the computations, thereby stabilizing momentum, pressure, and turbulence predictions and typically uses CFL values that are several times larger than those allowed by both the standard and preconditioned compressible equations. Also, unlike the compressible solvers, the incompressible equations usually require minimal limiting around complex geometries and consequently yield more accurate flow-field and force predictions. This work will present incompressible solutions about the Japanese Aerospace Exploration Agency (JAXA) Standard Model (JSM) configuration with and without nacelles and pylons at multiple angles of attack. These two JSM models were chosen for this study due to the availability of high-quality surface data.

## 2 Numerical Approach

The *Tenasi* unstructured flow solver is a node-centered, finite-volume, implicit scheme applied to general multi-element unstructured grids for parallel computations. The flow variables are stored at the vertices, and surface integrals are evaluated on the median dual surrounding each of these vertices. The non-overlapping control volumes formed by the median dual completely cover the domain and form a mesh that is dual to the elemental grid. Thus, a one-to-one mapping exists between the edges of the original grid and the faces of the control volumes. The inviscid fluxes are evaluated using either a Roe Approximate Riemann or a HLLC approach, while the viscous fluxes are evaluated using a directional derivative approach. Higher-order accuracy for the inviscid flux is achieved through the use of variable extrapolation with the gradients appearing in the reconstruction being evaluated, using an unweighted least-squares approach. The gradients appearing in the viscous fluxes are evaluated using a weighted least-squares approach. A Gram-Schmidt orthonormalization procedure is used to precompute the weights arising from the solution to the least-squares problem. *Tenasi* offers equation sets for five general flow regimes: Incompressible [21], Incompressible Surface Capturing [13], Compressible, Arbitrary Mach Number [18] and Compressible Multi-Species [6].

This work will rely upon the incompressible-flow regime presented in Cartesian coordinates and in conservative form as

$$\frac{\partial}{\partial t} \int_{\Omega} Q d\mathcal{V} + \int_{\partial\Omega} \mathbf{F} \cdot \hat{\mathbf{n}} dA = \int_{\partial\Omega} \mathbf{F}_v \cdot \hat{\mathbf{n}} dA \tag{1}$$

where $\hat{\mathbf{n}}$ is the outward pointing unit normal to the control volume $\mathcal{V}$. The vector of dependent variables and the components of the inviscid and viscous flux vectors are given as

$$Q = \begin{bmatrix} P \\ u \\ v \\ w \end{bmatrix} \quad \mathbf{F} \cdot \hat{\mathbf{n}} = \begin{bmatrix} \beta(\Theta - a_t) \\ u\Theta + \hat{n}_x P \\ v\Theta + \hat{n}_y P \\ w\Theta + \hat{n}_z P \end{bmatrix} \quad \mathbf{F}_v \cdot \hat{\mathbf{n}} = \begin{bmatrix} 0 \\ \hat{n}_x \tau_{xx} + \hat{n}_y \tau_{xy} + \hat{n}_z \tau_{xz} \\ \hat{n}_x \tau_{yx} + \hat{n}_y \tau_{yy} + \hat{n}_z \tau_{yz} \\ \hat{n}_x \tau_{zx} + \hat{n}_y \tau_{zy} + \hat{n}_z \tau_{zz} \end{bmatrix} \tag{2}$$

where $\beta$ is the artificial compressibility parameter, $u$, $v$, and $w$ are the Cartesian velocity components in the $x$, $y$, and $z$ directions, and $\hat{n}_x$, $\hat{n}_y$, and $\hat{n}_z$ are the components of the normalized control-volume face vector. $\Theta$ is the velocity normal to a control-volume face defined as

$$\Theta = \hat{n}_x u + \hat{n}_y v + \hat{n}_z w + a_t \tag{3}$$

where the grid speed $a_t = -\left(V_x \hat{n}_x + V_y \hat{n}_y + V_z \hat{n}_z\right)$ and the control-volume face velocity is $\mathbf{V}_s = V_x \hat{i} + V_y \hat{j} + V_z \hat{k}$. The shear-stress terms are defined as

$$\tau_{ij} = \frac{(\nu + \nu_t)}{Re_L} \left( \frac{\partial u_i}{\partial x_j} + \frac{\partial u_j}{\partial x_i} \right) \tag{4}$$

The variables in the preceding equations are normalized with respect to a characteristic length scale $(L_r)$ and reference values of velocity $(U_r)$, density $(\rho_r)$ and viscosity $(\mu_r)$. Thus, the Reynolds number is defined as $Re_L = \rho_r U_r L_r / \mu_r$. Pressure is normalized with $P = (P^* - P_\infty) / p_r U_r^2$ where $P^*$ is the local dimensional static pressure.

The turbulence models available in the flow solver include the one-equation Spalart-Allmaras model [17], the modified one-equation Menter Scale-Adaptive Scheme (SAS) model [11, 15], the two-equation $q - \omega$ model [5], the two-equation $k\epsilon k\omega$ hybrid model (baseline and SST variants) [15, 20], the two-equation $k - \epsilon$ model [10], the two-equation Wilcox $k - \omega$ model [23], the modified Wilcox $Stress - \omega$ model [15] and various modified versions of the Launder-Shima Reynolds stress model [9]. The models are loosely coupled with the mean flow in that the mean flow is computed with the eddy viscosity determined by the turbulence model, and then the turbulent quantities are computed with the new mean-flow values. The turbulence models are solved in the same manner as the mean flow, with the exception of the turbulence advection terms; whereas the mean-flow inviscid terms are evaluated with either a Roe or HLLC scheme, the advection terms of the turbulence models are simply upwinded depending solely on the direction of the velocity vector. Furthermore, to enhance the numerical stability of the turbulence models, the source-term contributions are included in the Jacobians only if the contributions strengthen the main diagonal.

Initial efforts in this study were met with inconsistent and unstable behaviors with the SST and Wilcox $k - \omega$ turbulence models on the JSM grids. Previous research with the one-equation SAS model [15] proved this model to be relatively insensitive to grid topology and grid refinement. This conclusion is further supported by recent studies [12] performed with the one-equation Spalart-Allmaras (SA) turbulence model, and together, these conclusions indicate that insensitivity to grid topology and refinement may be characteristic of one-equation turbulence models. For these reasons, this work will rely upon the one-equation SAS model due to its proven accuracy and insensitivity to grid topology [15]. The modified one-equation SAS model used in this work [15] is presented as

$$\frac{\partial}{\partial t} \int_\Omega \tilde{\nu}_t d\mathscr{V} + \int_{\partial\Omega} \tilde{\nu}_t \Theta dA = \frac{1}{Re} \int_{\partial\Omega} \left( \nu + \frac{\tilde{\nu}_t}{\sigma_m} \right) \overrightarrow{\nabla \tilde{\nu}_t} \cdot \hat{\mathbf{n}} dA + \mathscr{V} [P - D + C] \tag{5}$$

where

$$P = c_1 d_1 S \tilde{\nu}_t \quad D = \frac{c_2 \tilde{\nu}_t^2}{l_t^2 Re_L} \quad C = \left( \nabla \cdot \overrightarrow{u} \right) \tilde{\nu}_t \tag{6}$$

$$S = \left( 2 S_{ij} S_{ij} - \frac{2}{3} \left( \nabla \cdot \overrightarrow{u} \right)^2 \right)^{1/2} \quad S_{ij} = \frac{1}{2} \left( \frac{\partial u_i}{\partial x_j} + \frac{\partial u_j}{\partial x_i} \right) \quad d_1 = 1.0 + 0.4 \frac{\nu_t}{\tilde{\nu}_t} \tag{7}$$

$$l_t = \min(l_1, d_v) \qquad l_1 = \max(l_2, C_{SAS}\Delta_{min}) \qquad l_2{}^2 = \frac{S^2}{\nabla S \cdot \nabla S} \qquad (8)$$

and where $c_1 = 0.144$, $c_2 = 1.86$, $\sigma_m = 1.0$, $d_v$ is the distance to the nearest viscous surface, $C_{SAS} = 0.6$ and $\Delta_{min}$ is the local minimum node-to-node distance. The boundary conditions used for this study enforce $\tilde{\nu}_t = 0.0$ on a viscous surface and $\tilde{\nu}_t = 1.3$ for the farfield boundary. The eddy viscosity is determined by

$$\mu_t = \rho\nu_t = d_2\rho\tilde{\nu}_t \qquad (9)$$

$$d_2 = 1.0 - \exp\left[-0.2\left(b_1\chi + b_2\chi^3 + b_3\chi^5\right)\right] \qquad (10)$$

$$\chi = \frac{\tilde{\nu}_t}{\nu} \qquad b_1 = 0.001 \qquad b_2 = 0.005 \qquad b_3 = 0.0055 \qquad (11)$$

## 3 Grid Generation

Computer-aided design (CAD) files for the two JSM models were provided by the 3rd American Institute of Aeronautics and Astronautics (AIAA) CFD High Lift Prediction Workshop (HiLiftPW3) committee [1]. Figures 1 and 2 show the JSM model in both of the configurations used in this study. The only difference between the two models is the inclusion of the engine nacelle and pylon shown in Fig. 2. Therefore, the deployment of the slats and flaps is identical for the two models.

Following the "medium-mesh" guidelines prescribed by the HiLiftPW3 committee, Pointwise [16] grid-generation software was used to build the three dimensional mixed-element JSM grids for this study. The mesh-generation guidelines were refined on the upper- and lower-wing surfaces to give a better match with the grid spacing on the blunt trailing edges and thereby to enhance the grid quality in these regions. Pursuant to the mesh-generation guidelines, a viscous spacing of 0.00363 mm was

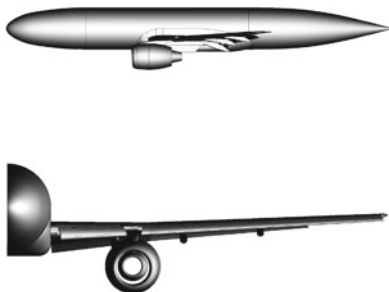**Fig. 1** Nacelle/Pylon OFF configuration
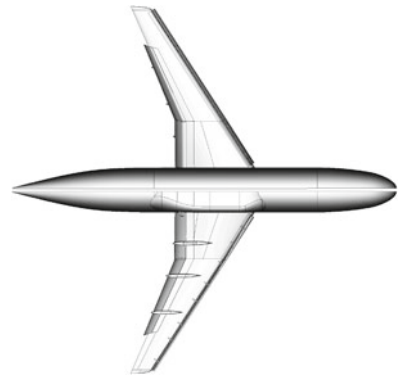
**Fig. 2** Nacelle/Pylon ON configuration

**Table 1** Total number of nodes and cells for JSM configurations

| Model | Grid level | Nodes | Hexahedrals | Prisms | Pyramids | Tetrahedrals |
|-------|-----------|-------|-------------|--------|----------|--------------|
| JSM OFF | Medium | 43,989,123 | 33,600,484 | 3,959,730 | 5,959,730 | 35,667,103 |
| JSM ON | Medium | 54,097,064 | 42,367,255 | 4,735,191 | 7,581,223 | 37,495,618 |

used on both grids to provide $y^+ \approx 2/3$, and the farfield boundary was placed 100-chord lengths away from the fuselage. Table 1 provides the element count for each grid.

## 4 Solution Process

Steady-state computations were performed with a Courant-Friedrichs-Lewy number $CFL = 10$ using a Roe Approximate Riemann inviscid flux evaluation and Approximate Jacobians for the incompressible solutions. The following conditions were applied: reference length $L_r = 0.5292$ m, reference temperature $T_r = 306.55$ K, reference density $\rho_r = 1.1328$ kg/m$^3$, reference velocity $U_r = 60.37$ m/s and reference dynamic viscosity $\mu = 1.8752x10^{-5}$ kg/(m*s). A no-slip, adiabatic, wall-boundary condition was applied to the aircraft surface, and freestream conditions were set at the farfield boundaries using the CVBC approach [21]. Following the HiLiftPW3 instructions, all simulations were performed with a half-span model. Thus, a symmetry boundary condition was applied to the symmetry plane at the centerline of the fuselage.

For parallel computations, both grids were divided into sections of roughly 300,000 grid points. This process yielded 140 and 180 partitions for the JSM OFF and ON grids, respectively. All simulations were performed on Auburn University's Hopper Cluster and required approximately 5.5 physical seconds per iteration with the *Tenasi* incompressible-flow regime for the steady-state computations.

In order to compute the lift curve, an alpha sweep was performed. To begin the sweep, simulations at 0° angle of attack (AOA) were performed on both JSM con-

figurations until convergence of the lift and drag forces was achieved. To start the simulations, 500 first-order, spatially accurate iterations were performed to establish the basic flow field around the JSM models, and 3,000 second-order, spatially accurate iterations were performed without limitation to converge the solution. Initially, the computations displayed some minor stability and convergence issues with both JSM grids, and consequently, the Barth-Jespersen limiter [3] was applied to alleviate these issues. Upon convergence at 0° AOA, the grid was gradually pitched-up over 109 iterations at a rate of 25 iterations per degree to an AOA of 4.36°, while keeping the freestream velocity constant. With the grid at 4.36°, computations were performed until the lift and drag forces converged. This process was repeated to compute solutions at additional AOAs of 10.47°, 14.54°, 18.58°, 20.59°, and 21.57° using the previous AOA as a starting point for the pitch-up procedure. Slower rates of rotation were used during the pitch-up procedure at the higher AOAs to prevent improper flow separation. All of these computations were performed as second-order, spatially accurate with $CFL = 10$.

This pitch-up procedure was computationally expensive and required almost 30 sec per iteration. The pitch-up approach was chosen over simply altering the direction of the inflow since the dynamic grid motion terms native to *Tenasi* automatically correct the flow field in every control volume at each iteration, while simply changing the inflow direction of the flow field would require every control volume in the domain to converge to the new flow-field direction. Thus, the pitch-up approach converges the quicker of the two methods. An added benefit was that the pitch-up process significantly reduced the onset of improper flow separation that plagued the initial efforts during which the inflow angle was switched directly from one AOA to another without any incremental changes in AOA. However, one draw back to the pitch-up approach is that the grid and solution must be rotated back to the original 0° AOA for the data comparisons.

## 5   Results and Discussion

In this section, the computational solutions for both JSM configurations are compared with experiment. Specifically, the computed values for $C_L$, $C_D$, and $C_M$ are analyzed, and $C_P$ at multiple slices along the slat, wing and flap are discussed.

### 5.1   Force and Moment Comparisons

The force and moment plots from the incompressible-flow solution using the SAS turbulence model are represented in Fig. 3 for the JSM Nacelle/Pylon OFF configuration and in Fig. 4 for the JSM Nacelle/Pylon ON configuration.

The computational results predict the stall properties very well for both JSM models. Although the lift is slightly underpredicted, the solution closely matches

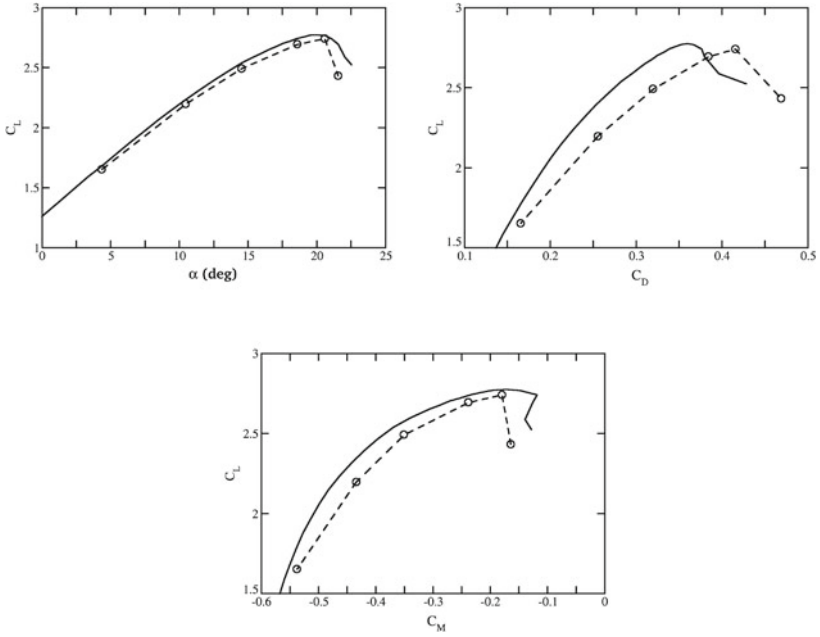**Fig. 3** Nacelle/Pylon OFF configuration: Force and moment comparison between the experiment
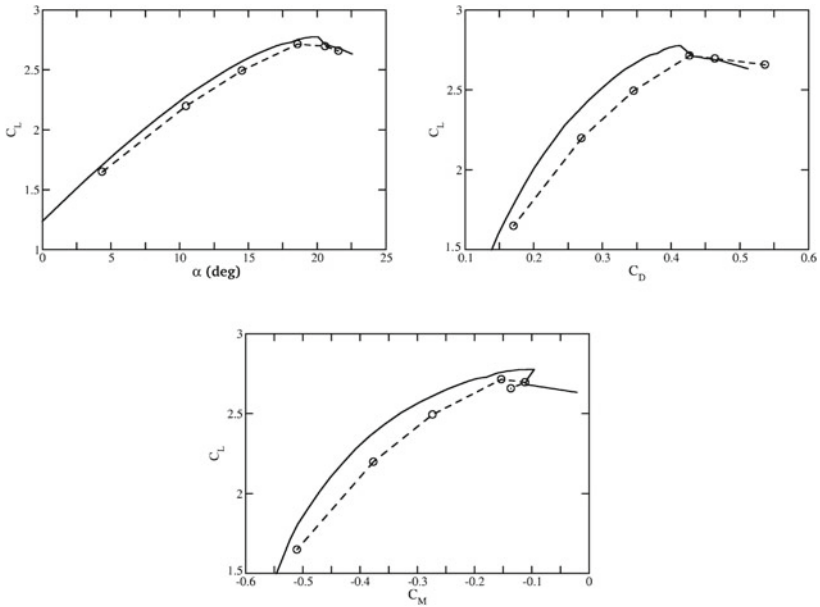(–) and the computation (∘ − ∘)

**Fig. 4** Nacelle/Pylon ON configuration: Force and moment comparison between the experiment
(–) and the computation (∘ − ∘)

experiments for the linear region of the lift curve. The location of $C_{L,max}$ is accurately predicted in the solution for both JSM configurations, but the predicted $C_{L,max}$ is slightly lower than the experiments. Historically, the SAS model tends to underpredict lift and moment while overpredicting drag. This behavior is clearly seen in the Figs. 3 and 4 where the drag and moment curves are slightly below and to the right of the experiments. The difference in $C_L$ stems largely from the solution underpredicting the suction peaks on the upper surface of the wing, and in extreme cases, indicates that the flow is incorrectly separating from the wing. These observations will be discussed in Sect. 5.2.

The differences in the force and moments obtained in this study compared with experiments are tabulated in Tables 2–4. The percentages in Tables 2, 3, and 4 denote $(|EXP_{value} - CFD_{value}|)/|EXP_{value}|$. From Table 2, the computational solution agrees very well with $C_L$ except for the JSM without N/P configuration at 21.57° AOA for which the flow was highly separated. Perhaps using several smaller incremental pitch-up procedures would correct this behavior. However, Table 3 shows that the $C_D$ was greatly overpredicted for both configurations. Although it is relatively insensitive to grid topology, the SAS turbulence model can be adversely affected if the boundary layer is overly resolved. The SAS model was calibrated for grids with a viscous spacing giving $y^+ = 1$. These grids followed the HiLiftPW3 meshing guidelines and were built with $y^+ = 2/3$. Therefore, the SAS turbulence model may be reacting to the tighter spacing and introducing higher drag. Table 4 demonstrates that the computed $C_M$ values follow the trend of the experiment but are generally 2 to 7% low except at higher AOA where the flow is beginning to separate thereby reducing lift, causing excessive drag, and consequently, increasing the moment. The experimental study with the JSM is a nacelle-installation study, and the computational results are compared in this manner as well. The effects of nacelle/pylon installation on the force and moment characteristics of the JSM is represented in the Fig. 5. The nacelle/pylon installation on the JSM shows that the lift characteristics of the JSM improve with the N/P installation, and the computational results from this study remain consistent with the experiments. However, the improvements in $C_L$ defined by $\Delta C_L$ are fairly underpredicted by the computations. Furthermore, the computational solution is consistent with the experiments on the stall characteristics

**Table 2** Differences in $C_L$ between CFD and experiments at different angle of attack

| AOA (deg) | JSM Nacelle/Pylon OFF | | | JSM Nacelle/Pylon ON | | |
|---|---|---|---|---|---|---|
| | $C_{L,CFD}$ | $C_{L,EXP}$ | %diff | $C_{L,CFD}$ | $C_{L,EXP}$ | %diff |
| 4.36 | 1.65205 | 1.68197 | 1.78 | 1.64948 | 1.70702 | 3.37 |
| 10.47 | 2.19648 | 2.23268 | 1.62 | 2.19814 | 2.27978 | 3.58 |
| 14.54 | 2.49076 | 2.53811 | 1.86 | 2.49387 | 2.57252 | 3.06 |
| 18.58 | 2.69273 | 2.74305 | 1.83 | 2.71337 | 2.75168 | 1.39 |
| 20.59 | 2.74047 | 2.76878 | 1.02 | 2.69592 | 2.70995 | 0.52 |
| 21.57 | 2.43176 | 2.69367 | 9.72 | 2.65730 | 2.68143 | 0.90 |

**Table 3** Differences in $C_D$ between CFD and experiments at different angle of attack

|  | JSM Nacelle/Pylon OFF | | | JSM Nacelle/Pylon ON | | |
| --- | --- | --- | --- | --- | --- | --- |
| AOA (deg) | $C_{D,CFD}$ | $C_{D,EXP}$ | %diff | $C_{D,CFD}$ | $C_{D,EXP}$ | %diff |
| 4.36 | 0.16569 | 0.15563 | 6.46 | 0.17077 | 0.16135 | 5.84 |
| 10.47 | 0.25563 | 0.22592 | 13.15 | 0.26978 | 0.24548 | 9.90 |
| 14.54 | 0.31991 | 0.28260 | 13.20 | 0.34566 | 0.31596 | 9.40 |
| 18.58 | 0.38419 | 0.33871 | 13.43 | 0.42690 | 0.38952 | 9.59 |
| 20.59 | 0.41580 | 0.36664 | 13.41 | 0.46412 | 0.43112 | 7.65 |
| 21.57 | 0.46909 | 0.37966 | 23.55 | 0.53688 | 0.47255 | 13.61 |

**Table 4** Differences in $C_M$ between CFD and experiments at different angle of attack

|  | JSM Nacelle/Pylon OFF | | | JSM Nacelle/Pylon ON | | |
| --- | --- | --- | --- | --- | --- | --- |
| AOA (deg) | $C_{M,CFD}$ | $C_{M,EXP}$ | %diff | $C_{M,CFD}$ | $C_{M,EXP}$ | %diff |
| 4.36 | −0.53741 | −0.54962 | 2.22 | −0.50999 | −0.52279 | 2.45 |
| 10.47 | −0.43387 | −0.46323 | 6.34 | −0.37631 | −0.40718 | 7.58 |
| 14.54 | −0.35041 | −0.36891 | 5.01 | −0.27325 | −0.29527 | 7.56 |
| 18.58 | −0.23815 | −0.23318 | 2.13 | −0.15306 | −0.16103 | 4.95 |
| 20.59 | −0.17903 | −0.14896 | 20.18 | −0.11156 | −0.10892 | 2.42 |
| 21.57 | −0.16394 | −0.12566 | 30.46 | −0.13620 | −0.11073 | 23.00 |

of these two configurations with the computational results agreeing with experiment that the JSM with N/P configuration stalls earlier than the configuration without N/P. The effects of the nacelle installation on the basis of $\Delta C_D$ and $\Delta C_M$ predicted by computation shows greater agreement with the experiments than $\Delta C_L$.

## 5.2   Pressure Comparisons

Figure 6 shows the various cutting planes for $C_P$ extraction and the approximate distance in percentages from root to tip with respect to the wingspan. Although it is not shown in Fig. 6, the cuts on the deployed wing elements are not at a constant $Y$ location. These details are explained on the HiLiftPW3 website [1]. Due to space restrictions, only a small selection of the available comparisons will be presented. The focus in this section is to demonstrate the behavior of the simulations with the understanding that the presented comparisons are indicative of the overall solution at each AOA.

Figure 7 shows excellent agreement between the experiments and the solutions for both JSM configurations at 20.59° AOA. A slight underprediction of the suction peak on the slat is noticeable for both configurations, and a more pronounced underprediction the suction peak on the flap is seen for the JSM without N/P. The
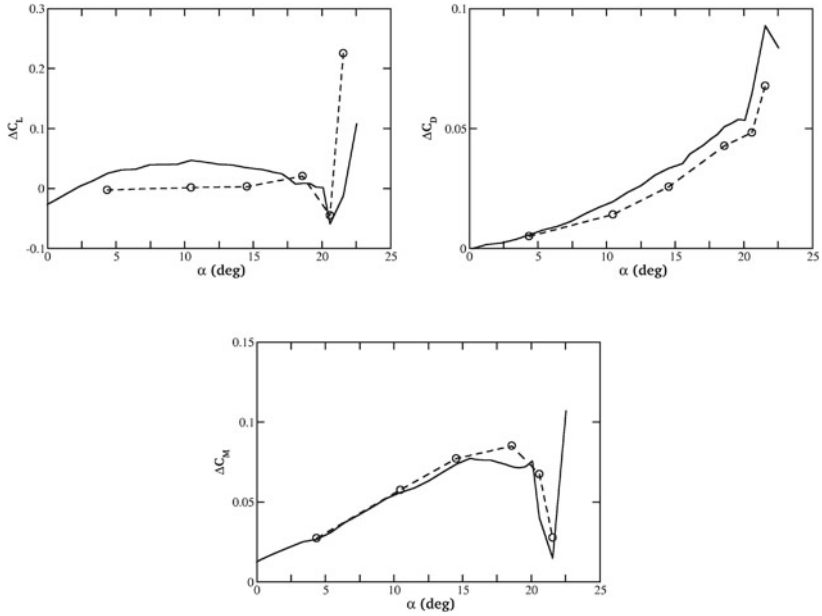
**Fig. 5** Comparison between the experiment (–) and the computation ($\circ - \circ$) of changes in $C_L$, $C_D$, and $C_M$ between the JSM configurations ("with N/P" minus "without N/P")
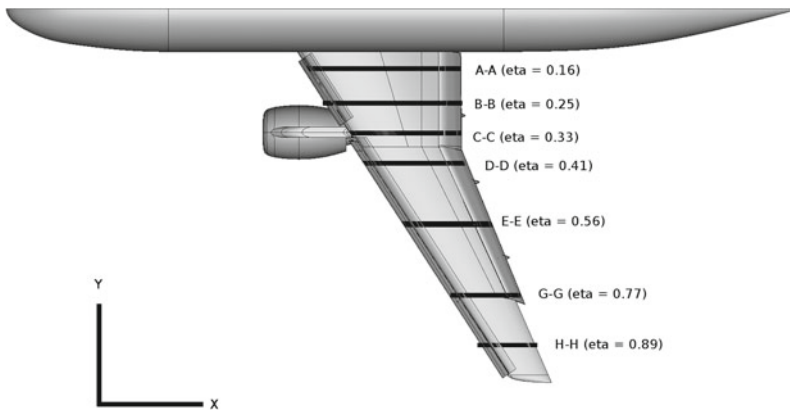


**Fig. 6** $C_P$ Extraction locations on the wing elements

agreement between experiment and computation seen in these plots is characteristic of the results at wing stations A-A to G-G for AOA up to 20.59°. Minor fluctuations in the solution at these stations and AOAs are seen predominantly on the upper surface of the flaps, while the solution on the slats and wing exhibit consistently excellent agreement. Taken as a whole, these $C_P$ results lead to the favorable comparison in $C_L$ seen in Figs. 3 and 4 for $C_L \leq C_{Lmax}$ for both JSM configurations. Figure 8 shows the effects of flow separation at 21.57° for the JSM without N/P. Strong separations
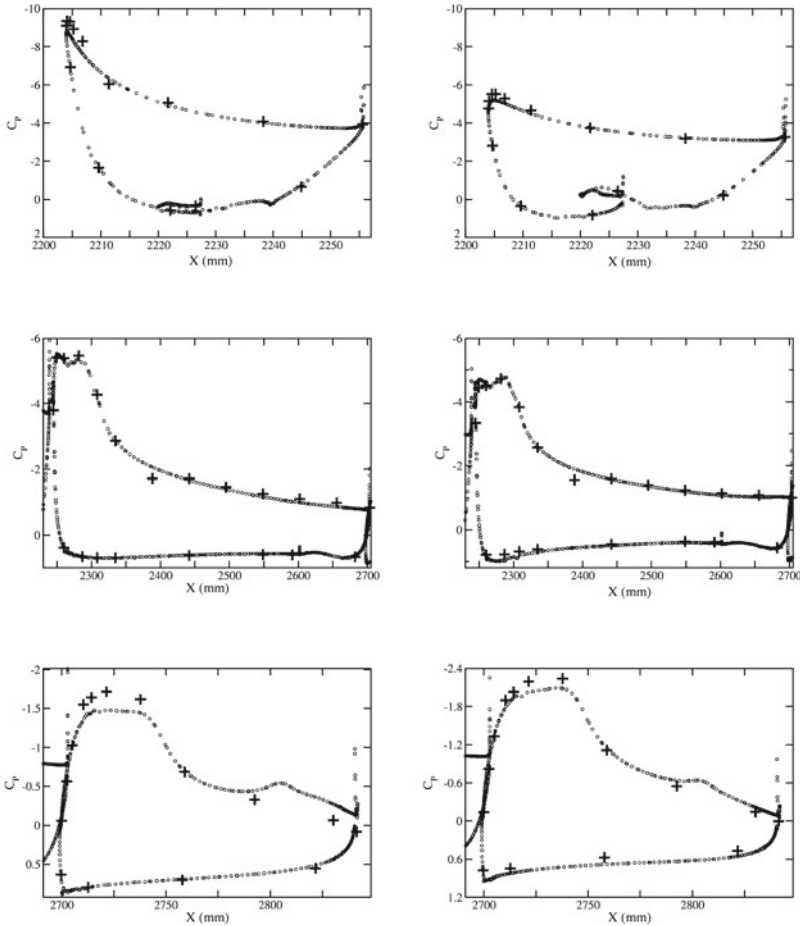
**Fig. 7** $C_P$ comparison between the experiment $(+)$ and the computation $(\circ)$ for the Nacelle/Pylon OFF (left) and ON (right) configurations at 20.59° AOA at station D-D for the slat (upper pair), the wing (middle pair) and the flap (bottom pair) elements

are evident on the slats, wing and flaps and lead to the drop in $C_L$ seen in Fig. 3. As expected from $C_L$ in Fig. 4, $C_P$ for the JSM with N/P agrees very well with the experiment at 21.57° AOA.

Station D-D is located slightly outboard and behind the engine nacelle and pylon as seen in Fig. 6. The effects of the nacelle and pylon are clearly evident in Figs. 7 and 8 for higher AOAs. Stronger suction peaks are captured by both the experiment and the computation over the slat and wing for the JSM without N/P, while a stronger peak over the flap is realized for the JSM with N/P. These effects are minimal at low AOAs when the wakes of the nacelle and pylon pass beneath the wing elements. However, as AOA increases, the wake increasingly interacts with the wing elements
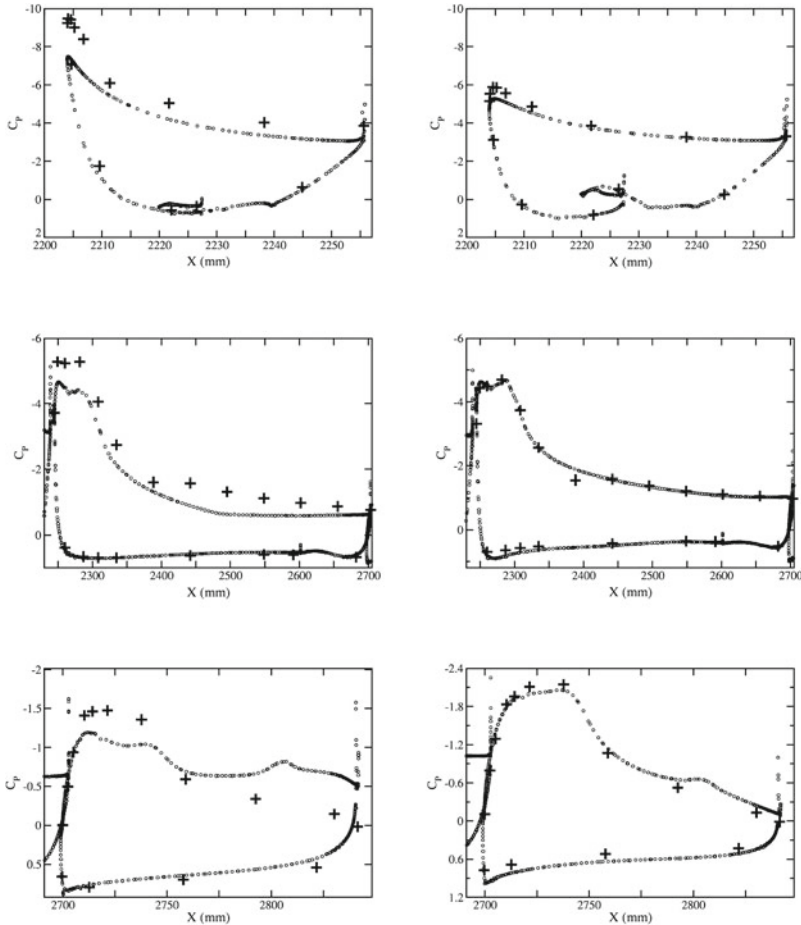
**Fig. 8** $C_P$ comparison between the experiment (+) and the computation (○) for the Nacelle/Pylon OFF (left) and ON (right) configurations at 21.57° AOA at Station D-D for the slat (upper pair), the wing (middle pair), and the flap (bottom pair) elements

and strongly influences the flow field. Specifically, the slat and wing experience decelerated N/P wake flow, yielding weaker suction peaks, while the flap encounters accelerated flow resulting in a stronger suction peak.

Although the solutions for wing stations A-A to G-G exhibit no signs of separation until 21.57° AOA, station H-H near the wing tip separates early in the alpha sweep for both JSM configurations. Figure 9 presents an excellent comparison with experiment with no sign of separation at 4.36° AOA. However, the computed flow obviously separates between 4.36° and 10.47° AOA, and the separation is relatively consistent up to 21.57° AOA as seen in Figs. 10 and 11. Early separation at the wing tip is a likely cause for the drop-off in $C_L$ as the angle of attack increases. Pitching-up from
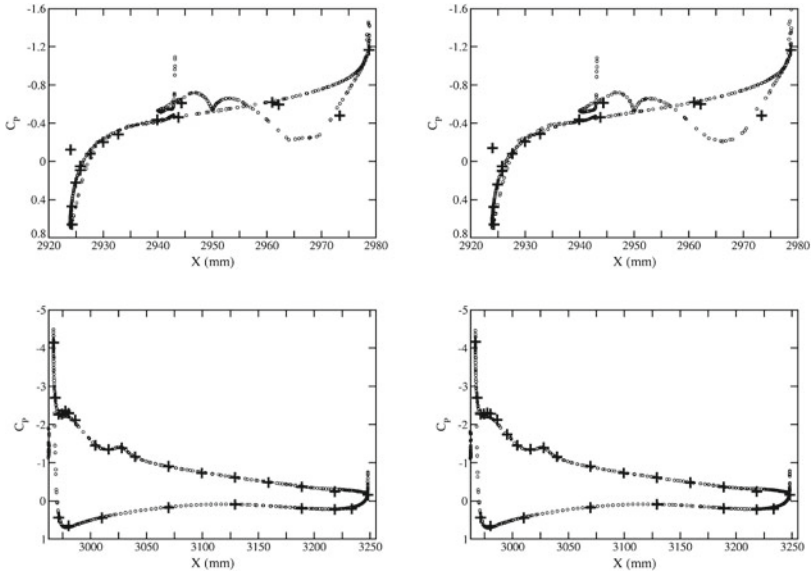
**Fig. 9** $C_P$ comparison between the experiment (+) and the computation (○) for the Nacelle/Pylon OFF (left) and ON (right) configurations at 4.36° AOA at Station H-H for the slat (upper pair) and the wing (lower pair) elements



**Fig. 10** $C_P$ comparison between the experiment (+) and the computation (○) for the Nacelle/Pylon OFF (left) and ON (right) configurations at 10.47° AOA at Station H-H for the slat (upper pair) and the wing (lower pair) element

**Fig. 11** $C_P$ comparison between the experiment (+) and the computation (∘) for the Nacelle/Pylon OFF (left) and ON (right) configurations at 21.57° AOA at Station H-H for the slat (upper pair) and the wing (lower pair) element
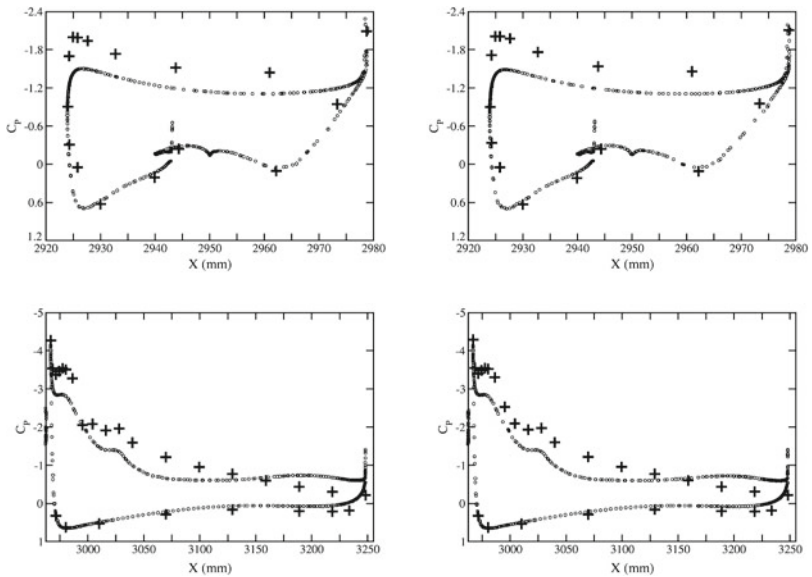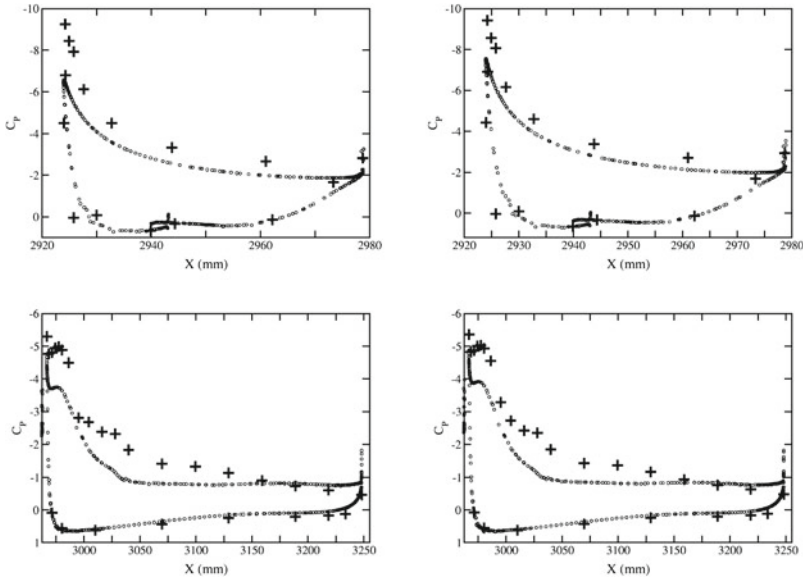
one angle to the next prevented early flow separation for the majority of the wing, and it may be possible to use smaller increments in angle of attack in future simulations to prevent the onset of flow separation at the wing tip.

## 6 Conclusions and Future Work

The *Tenasi* unstructured-flow solver successfully applied the incompressible Navier–Stokes equations to two JSM high-lift wing configurations and achieved excellent agreement between the computations and experiments. These results demonstrate that the compressible equations are not required for accurate simulations about high-lift configurations. However, it does raise the question of how far the incompressible equations can be used before compressible effects significantly influence the solution. Although the mean flow in these situations is below $Mach = 0.2$, localized flow accelerations and thermodynamic effects may place regions of the domain clearly above the accepted incompressible limit of $Mach = 0.3$. Future efforts will attempt to identify regions of flow about the JSM models which cross into the compressible range and then to quantify the resulting compressible effects.

The HiLiftPW3 meshing guidelines were closely followed for the JSM grids used in this study. However, the guidelines for viscous spacing may be too restrictive for the

SAS turbulence model as implemented in the *Tenasi* flow solver. Future efforts will explore alternative methods to provide adequate mesh density in the boundary-layer region, while at the same time reducing the size of the mesh. Using a smaller mesh to attain a quality solution will reduce the computational expense in both runtime and resources. Further, efforts to re-calibrate the SAS model for better $C_L$ and $C_D$ predictions are underway.

The pitch-up procedure employed during the simulations greatly reduced flow separation in the solutions. Fine-tuning this process to prevent wing-tip flow separation is needed for robust computations of high-lift configurations.

These simulations were performed assuming a fully turbulent boundary layer. It is conceivable that transition modeling is necessary for the utmost in accuracy in these simulations, especially at high angles of attack. Recent results of HiLiftPW3 [1] offered no firm conclusion to this inquiry; several participants showed improved performance with transition modeling, while others did not. So, this area requires more research.

Automatic grid refinement is capable of reducing grid size while placing adequate grid resolution where it is needed. However, modern techniques for unstructured grids are highly heuristic, and it is difficult to maintain mesh quality for multi-element grids as the individual elements are repeatedly refined. This is an active area of research.

# References

1. 3rd AIAA CFD High Lift Prediction Workshop. https://hiliftpw.larc.nasa.gov
2. Anderson, J.: Fundamentals of Aerodynamics, 2nd edn. McGraw-Hill, Inc. (1991)
3. Barth, T.J., Jespersen, D.C.: The design and application of upwind schemes on unstructured meshes. In: 27th Aerospace Sciences Meeting, Jan 1989, Reno, NV, AIAA Paper 89-0366 (1989)
4. Briley, W., Taylor, L., Whitfield, D.: High-resolution viscous flow simulations at arbitrary mach number. J. Comput. Phys. **184**, 79–105 (2003)
5. Coakley, T.J.: Turbulence modeling methods for the compressible Navier-Stokes equations. In: AIAA 16th Fluid and Plasma Dynamics Conference, July 1983, Danvers, Mass, AIAA Paper 83-1693 (1983)
6. Currier, N.G.: A hybrid method for flows in local chemical equilibrium and nonequilibrium. Master's thesis, University of Tennessee at Chattanooga (2010)
7. Eriksson, L.: A preconditioned navier-stokes solver for low mach number flows. In: Proceedings of the Third ECCOMAS Computational Fluid Dynamics Conference, Paris, France, pp. 199–205 (1996)
8. Gupta, A.: Preconditioning methods for ideal and multiphase fluid flows. Ph.D. thesis, University of Tennessee at Chattanooga (2013)

9. Hajjawi, M., Taylor, L.K., Nichols, D.S.: Assessment and modification for reynolds stress transport turbulence model flow prediction. In: 46th AIAA Aerospace Sciences Meeting and Exhibit, Jan 2008, AIAA Paper 2008-0568 (2008)
10. Liou, W., Shih, T.: Transonic turbulent flow predictions with new two-equation turbulence models. Technical Report No. CR-198444, NASA (1996)
11. Menter, F., Kuntz, M., Bender, R.: A scale-adaptive simulation model for turbulent flow predictions. In: 41st AIAA Aerospace Sciences Meeting and Exhibit, 6–9 Jan 2003, Reno, NV, AIAA Paper 2003-0767 (2003)
12. Murayama, M., Yamamoto, K., Ito, Y.: Japan aerospace exploration agency studies for the second high-lift prediction workshop. J. Aircr. **52**(4) (2015)
13. Nichols, D.S., Hyams, D.G., Sreenivas, K., Mitchell, B., Taylor, L.K., Whitfield, D.L.: An unstructured incompressible multi-phase solution algorithm. In: 44th AIAA Aerospace Sciences Meeting and Exhibit, 9–12 Jan 2006, Reno, NV, AIAA Paper 2006-1290 (2006)
14. Nichols, D.S., Mitchell, B., Sreenivas, K., Taylor, L.K., Briley, W.R., Whitfield, D.L.: Aerosol propagation in an urban environment. In: 36th AIAA Fluid Dynamics Conference and Exhibit, 5–8 June 2006, San Francisco, CA, AIAA Paper 2006-3726 (2006)
15. Nichols, D.S., Sreenivas, K., Karman, S.L., Mitchell, B.: Turbulence modeling for highly separated flows. In: 45th AIAA Aerospace Sciences Meeting and Exhibit, 8–11 Jan 2007, Reno, NV, AIAA Paper 2007–1407 (2007)
16. Pointwise: Version 18.0 R1. http://www.pointwise.com
17. Spalart, P.R., Allmaras, S.R.: A one-equation turbulence model for aerodynamic flows. In: AIAA Paper 92-0439 (1992)
18. Sreenivas, K., Hyams, D., Nichols, D., Mitchell, B., Taylor, L., Briley, W., Whitfield, D.: Development of an unstructured parallel flow solver for arbitrary mach numbers. In: 43rd AIAA Aerospace Sciences Meeting and Exhibit, Jan 2005, AIAA Paper 2005-0325 (2005)
19. Sreenivas, K., Taylor, L., Briley, W.: A global preconditioner for viscous flow simulations at all mach numbers. In: 36th AIAA Fluid Dynamics Conference and Exhibit, 5–8 June 2006, San Francisco, CA, AIAA Paper 2006-3852 (2006)
20. Strelets, M.: Detached eddy simulation of massively separated flows. In: 39th AIAA Aerospace Sciences Meeting and Exhibit, 8–11 Jan 2001, Reno, NV, AIAA Paper 01-0879 (2001)
21. Taylor, L.K.: Unsteady three-dimensional incompressible algorithm based on artificial compressibility. Ph.D. thesis, Mississippi State University (1991)
22. Turkel, E.: Review of preconditioning methods for fluid dynamics. Appl. Numer. Math. **12**(13), 257–284 (1993)
23. Wilcox, D.C.: Turbulence Modeling for CFD. 3rd edn. DCW Industries (2006)

# Numerical Investigations of the Jaxa High-Lift Configuration Standard Model with MFlow Solver

**Jiangtao Chen, Jian Zhang, Jing Tang and Yaobing Zhang**

**Abstract** Numerical investigations of the Jaxa high-lift configuration Standard Model from the 3rd AIAA CFD High Lift Prediction Workshop are performed with the in-house solver MFlow. The solver is based on a cell-centered, finite-volume method and is capable of handling various element types. Hybrid grids provided by the committee are used in the simulations. The performance of massively parallel computing and force/moment predictions are the two emphases of this chapter. The speedup rate of parallel computations is satisfactory, only deviating obviously from the theoretical rate for computations on 3,200 or more processors. The efficiency of parallel computations remains greater than 75%, even for computation on 6,400 processors. The force and moment prediction is then analyzed in detail. The initialization of the flow field plays an important role in the predictions of high-lift configurations. The simulation initiated with a converged flow field obtained at a lower angle of attack achieves better agreement with experiment compared with predictions initiated with freestream values, in terms of a larger maximum-lift coefficient. The drag-and-pitching-moment prediction is also improved. The solver shows good agreement with experiment at lower angles of attack, but more attention is needed at angles of attack near and beyond stall.

## Nomenclature

$\alpha$ = angle of attack
$c_{ref}$ = mean aerodynamic chord
$Ma$ = Mach number
$Re_c$ = Reynolds number based on $c_{ref}$
$T_\infty$ = free stream temperature
$P_\infty$ = free stream static pressure

J. Chen · J. Zhang · J. Tang · Y. Zhang (✉)
China Aerodynamics Research and Development Center,
Mianyang, Sichuan, People's Republic of China
e-mail: zhyb_super@sina.cn

$\eta$ = fraction of wing span
$C_L$ = lift coefficient
$C_{L\_max}$ = maximum value of lift coefficient
$C_D$ = drag coefficient
$C_M$ = pitching-moment coefficient
$C_p$ = pressure coefficient
$C_f$ = skin-friction coefficient
$C_{fx}$ = streamwise component of skin-friction coefficient

## 1 Introduction

The design of high-lift devices with great efficiency is one of the key factors in the aerodynamic design process for transport aircraft. Multi-element wings with medium-to-high aspect ratios are often adopted on commercial and military transport aircraft. Van Dam [1] reviewed developments in aerodynamic design and analysis methods for multi-element high-lift systems. Computational methods are slowly superseding empirical methods, and design engineers are spending more and more time applying computational tools instead of conducting physical experiments to design and analyze aircrafts, including high-lift systems. The high-lift flow field is characterized by confluent wakes, wake/boundary-layer merging, separated flows, transition, and so on. With the rapid development of Computational Fluid Dynamics (CFD) in recent years, including grid-generation techniques, flow solvers, high performance clusters, etc., it has become possible to assess the aerodynamic characteristics of three-dimensional high-lift configurations. An assessment of the capability of numerical predictions for high-lift flow fields can be found in Rumsey and Ying [2].

CFD is now playing a more and more important role in the design process for aircraft. CFD verification and validation exercises have drawn extensive attention among CFD researchers and vendors. To assess the numerical prediction capability of CFD technology for swept, medium-to-high aspect-ratio wings in landing/takeoff (high-lift) configurations, the Applied Aerodynamics Technical Committee of the AIAA (American Institute of Aeronautics and Astronautics) initiated the AIAA CFD High Lift Prediction Workshop (HiLiftPW) Series in 2010. Numerous numerical results [3–7] for the NASA Trap Wing configuration [8, 9] assessed the capability of state-of-the-art numerical prediction. According to the summary of the workshop [10], CFD tended to underpredict lift, drag, and the magnitude of the pitching moment compared with experiment. Numerical prediction was more difficult at higher angles of attack near stall. Some participants predicted early stall. Initial-condition dependency of solutions at high angles of attack was found. Some participants reported that better agreement with experimental data was reached at high angles of attack if the solution was initialized with a converged flow field obtained at a lower angle of attack.

For the DLR-F11 configuration from HiLiftPW-2, the importance of including slat and flap brackets during numerical simulations, when comparing with the experiment, was established [11]. Most computations without brackets tended to predict increasing $C_L$ well past the nominal stall angle [11–17]. The CFD scatter was larger at the angles of attack near stall and did not decrease much past a certain grid-refinement level [11]. The accurate prediction of high-lift flow fields still remains a challenge for Reynolds-averaged Navier-Stokes (RANS) flow solvers.

Unstructured grid methods have been widely accepted in recent years due to their efficient handling of complex geometries. The time required to generate an unstructured, mixed grid for a complex configuration is significantly lower than that required to generate a multi-block, structured grid. Therefore, it is very likely that setup time is significantly reduced, with only minor user intervention. Another very attractive feature of unstructured-grid methodology is the possibility of solution-based grid adaptation [18]. More than half of the participants of the high-lift workshops used unstructured mesh CFD tools. However, the amount of elements for a complex three-dimensional configuration can easily reach the magnitude of tens of millions, or even hundreds of millions. The huge memory requirement, especially when unstructured grids are used, stimulates the development of massively parallel computing. The performance of massively parallel computing has become an essential assessment for modern CFD tools.

To assess the capability of the in-house unstructured-grid solver MFlow for high-lift flow field prediction, this chapter presents numerical investigations of Jaxa high-lift configuration Standard Model (JSM) from HiLiftPW3. The chapter is organized as follows. First, the geometry and computational grids are briefly described. Then, the numerical methods adopted for the computations are introduced. The results section presents the performance of parallel computing and force/moment prediction. Finally, conclusions are drawn.

## 2 Geometry and Computational Grids

JSM, the high-lift configuration from HiLiftpw-3, is investigated in this chapter. The model is representative of a modern regional jet airliner [19–21]; it is a wing-body high-lift system in a nominal landing configuration (single segment baseline slat and single segment 30° flap) with support brackets on, and nacelle/pylon on/off (see Fig. 1). The flow field contains major flow characteristics of high-lift problems, whereas the model is simplified compared with a real aircraft configuration. A low-speed-wind tunnel experiment was implemented in a 6.5- by 5.5-m low-speed wind tunnel in JAXA (JAXA-LWT1) with rich sets of test data available for CFD validation.

To assess the effects of including a nacelle and pylon in the high-lift system, two test cases[1] are required concerning the previous model, with or without the

---

[1]Data available online at https://hiliftpw.larc.nasa.gov/Workshop3/testcases.html.

**Fig. 1** JSM configuration (**left**: configuration without nacelle/pylon assembled; **middle**: configuration with nacelle/pylon assembled; **right**: cross section at $\eta = 0.43$)

**Table 1** Information of the computational grids

| Configuration | #nodes | #elements | #hexahedrons | #prims | #pyramids | #tet |
|---|---|---|---|---|---|---|
| Nacelle/Pylon OFF | 52,697,852 | 108,519,653 | 14,646,898 | 65,466,705 | 380,361 | 28,025,689 |
| Nacelle/Pylon ON | 58,267,292 | 120,213,635 | 16,021,438 | 72,717,038 | 411,472 | 31,063,687 |

nacelle/pylon assembled, respectively. The angles of attack to be computed are 4.36, 10.47, 14.54, 18.58, 20.59, and 21.57°. The freestream conditions are as follows:

$$Re_c = 1.93 \times 10^6, Ma = 0.172, T_\infty = 306.55\,\text{K}, P_\infty = 99,770.5\,\text{Pa}$$

The unstructured grids[2] provided by the committee were generated with ANSA v17.1.0 by BETA CAE Systems. The detailed information of supplied grids is listed in Table 1. As shown in Fig. 2, anisotropic quad mesh was generated at the leading and trailing edges of wing, slat, and flap, as well as near the wingtip.

## 3   Numerical Methods

The simulations in this chapter are performed with the in-house unstructured grid solver MFlow [13], which is based on a cell-centered, finite-volume method and is capable of handling various element types (hexahedron, tetrahedron, prism, pyramid, and other polyhedrons generated when a geometrical multi-grid method is used). Second-order accuracy in space is achieved by linear reconstruction in cells. The vertex-based Green–Gauss approach [22] is adopted for gradient computations to maintain accuracy and robustness. Venkatakrishnan's limiter [23] is used to prevent the generation of oscillations in regions of high gradients. The Roe scheme is used for inviscid flux computations.

---

[2]Mesh available online at ftp://hiliftpw-ftp.larc.nasa.gov/outgoing/HiLiftPW3/JSM_Grids/ Committee_Grids/E-JSM_UnstrMixed_ANSA.

**a.** fuselage                          **b.** slat                          **c.** main wing



**d.** flap                          **e.** nacelle/pylon                          **f.** symmetry plane
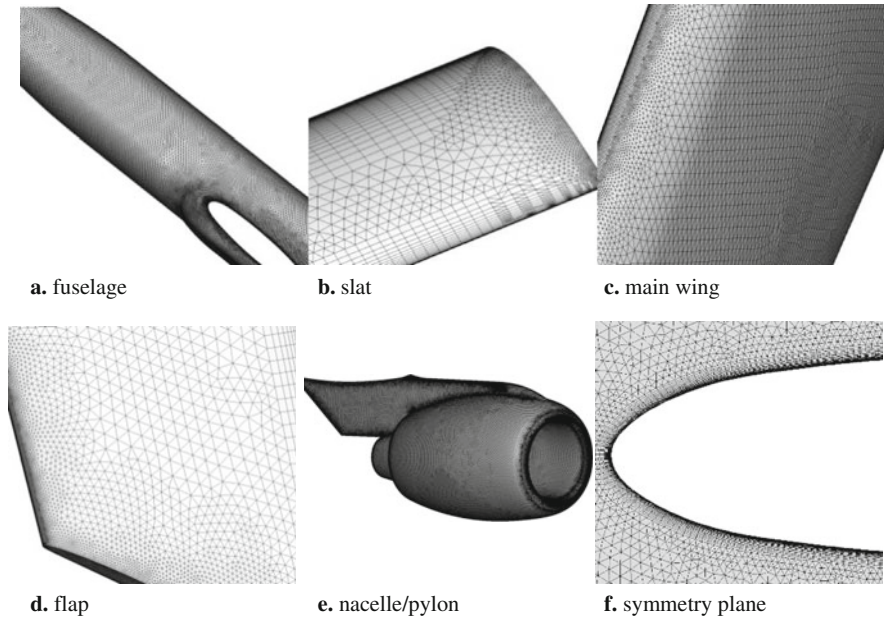
**Fig. 2** Surface grids on various parts of the model

The preconditioning matrix due to Weiss and Smith [24] is employed for low-Mach-number computations. Steady state is approached with the first-order backward Euler time-differencing scheme with local time stepping to accelerate the convergence. The flux Jacobian is derived from a first-order upwind scheme. The split convective flux Jacobian is composed of the convective flux Jacobian and its spectral radius. The viscous flux Jacobian is approximated by its spectral radius. The geometrical multi-grid methodology is used to accelerate the convergence to steady state. Fully turbulent flow is assumed, and the "Standard" Spalart-Allmaras One-Equation Model[3] [25] is used. Initial-condition dependency of solutions at high angles of attack for the prediction of high-lift flow field is widely accepted. The initialization of computation, whether with freestream values or a converged flow field obtained at a lower angle of attack, is discussed in this chapter.

Before the implementation of parallel computing on a distributed parallel system, the Metis package [26], a set of programs for partitioning graphs or meshes, is used to partition the entire grid into multi-zone smaller grids. The Message Passing Interface (MPI) [27, 28] is used for data exchange between various processors.

---

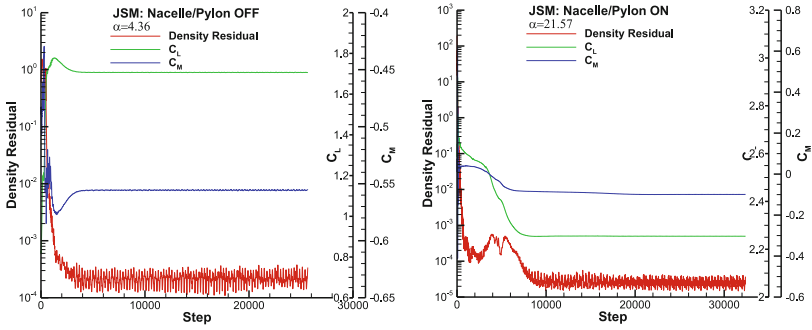[3]The formulation can be found on https://turbmodels.larc.nasa.gov/spalart.html.

**Fig. 3** Convergence of density residual and force and moment coefficient

## 4   Results

To exclude the uncertainty introduced by the lack of computational convergence, all the computations are run until the norm of the global residual decreases by more than three orders of magnitude, and the final oscillations of aerodynamic force and moment are less than 1%. Examples of the convergence of density residual and force/moment coefficient are presented in Fig. 3.

### 4.1   The Performance of Massively Parallel Computing

The speedup rate $S$ and efficiency $E$ are often used to assess the performance of massively parallel computing. They are defined as:

$$S = \frac{T_{ref}}{T_n}, E = \frac{S}{n/n_{ref}} \times 100\%$$

where $T_n$ is the amount of time taken by one iteration step when parallel computation is performed on $n$ processors. The linear speedup rate (execute $n$ times faster on $n$ processors) is hard to achieve in engineering, due to the massive data exchange required between various processors. As shown in Figs. 4 and 5, the speedup rate is satisfactory, only deviating obviously from the theoretical rate for computations on 3,200 processors or more. The efficiency remains greater than 75%, even for the computation on 6,400 processors. The load-balance problem is well handled by Metis package. Since unstructured grid is not subjected to restrictions of topology, higher efficiency is easily achieved.

## 4.2 The Effects of Nacelle and Pylon Assembled

The precise prediction of $C_{L\_max}$ and the angle at which it occurs is essential to the design of high-lift devices. Some participants predicted early stall for the NASA Trap Wing configuration from HiLiftPW-1. Many participants predicted delayed stall for the DLR-F11 configuration from HiLiftPW-2. The simulation of flow fields around and beyond stall remains a great challenge for RANS solvers.

For JSM without nacelle and pylon assembled, the lift prediction, shown in Fig. 6, shows excellent agreement with experimental data at small to medium angles of attack, if the flow field is initialized with a converged flow field obtained at a lower angle of attack. The increment of angle of attack is 2° before $\alpha = 18.58°$ and 1° after that. The predicted lift falls after $\alpha = 18.58°$ and then rises again from $\alpha = 19.58°$. However, the experimental lift exhibits continuous rise after $\alpha = 18.58°$, and peaks at $\alpha = 20.09°$. The predicted $C_{L\_max}$ occurs about 1.5° earlier than in experiments. Consequentially, the predicted $C_{L\_max}$ is smaller than experiment by 0.016.

The effect of flow-field initialization is then examined. The lift prediction initialized with freestream values does not show obvious difference with previous computations at smaller angles of attack. The lift is underpredicted at $\alpha = 18.58°$ and also breaks hereafter. The lift prediction is improved if the computation restarts from the
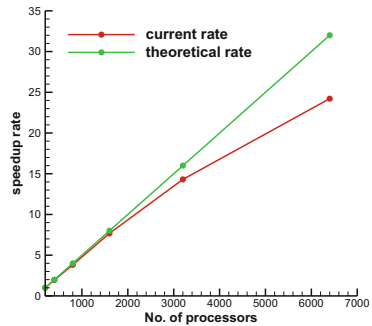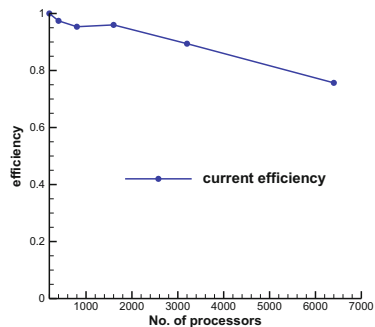


**Fig. 4** Speedup rate curve
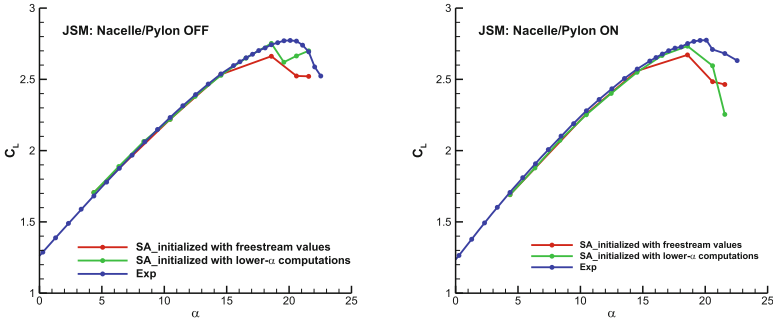


**Fig. 5** Efficiency of parallel computing

**Fig. 6** Lift prediction for JSM (**left**: Nacelle/Pylon OFF; **right**: Nacelle/Pylon ON)
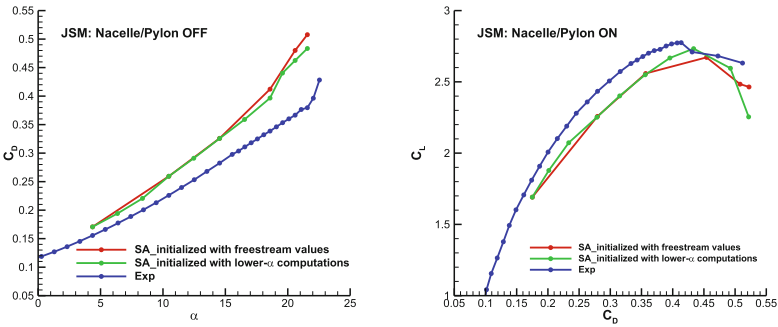


**Fig. 7** Drag and polar curve prediction for JSM (**left**: Nacelle/Pylon OFF; **right**: Nacelle/Pylon ON)

solutions at a lower angle of attack, although the predictions around stall are still not fully satisfactory.

Almost the same findings are observed for the prediction of nacelle-and-pylon-assembled configuration. The predicted lift drops dramatically after $\alpha = 18.58°$, while the experimental curve continuously rises after that and peaks at $\alpha = 20.09°$.

For both configurations, drag is overpredicted, as shown in Fig. 7. The drag prediction is slightly improved if the flow field is initialized with a converged flow field obtained at a lower angle of attack.

The precise prediction of pitching moment for a complex, three-dimensional aircraft is a great challenge for RANS solvers. For the configuration without nacelle and pylon, the predicted $C_M$ lies above or under the experimental curve at various angles of attack, as shown in Fig. 8. For the configuration with nacelle and pylon assembled, the prediction is satisfactory compared with experiment, except at $\alpha = 20.59°$, where the predicted pitching moment becomes positive. Generally, the importance of initializing the flow field with the solution at a previous angle is proved.

To assess the effects of adding a nacelle and pylon to the high-lift system, the increments in lift, drag, and pitching moment are presented in Fig. 9, together with experimental deltas. The increment in drag is well predicted at small to medium
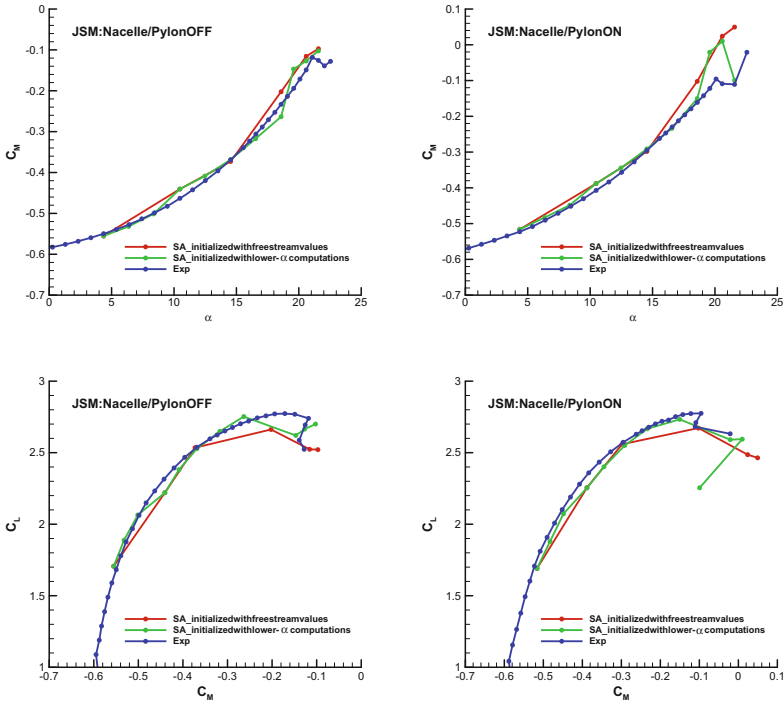
**Fig. 8** Pitching moment prediction for JSM (**left**: Nacelle/Pylon OFF; **right**: Nacelle/Pylon ON)
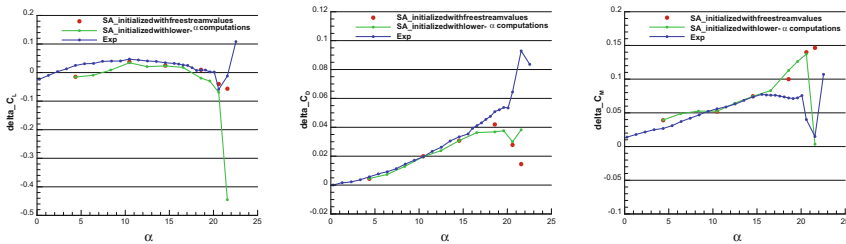


**Fig. 9** Increments in lift, drag, and pitching moment due to nacelle/pylon

angles of attack, but drops earlier than in the experiment. The prediction of the increment of the lift and pitching moment is not particularly satisfactory, especially near stall.

The $C_p$ distributions at several span stations are compared with experiment to further assess the accuracy of numerical prediction. The seven stations shown in Fig. 10 are located near the wing root, mid-span, and wingtip, respectively. The results presented in Figs. 11, 12, 13, 14, 15, 16, 17, 18, 19, 20, 21 and 22 were initialized with previous computation at lower angles of attack. The predicted $C_p$ agrees well with experiment, at $\alpha = 4.36, 10.47, 14.54$ and $18.58°$, except at the outboard-most span
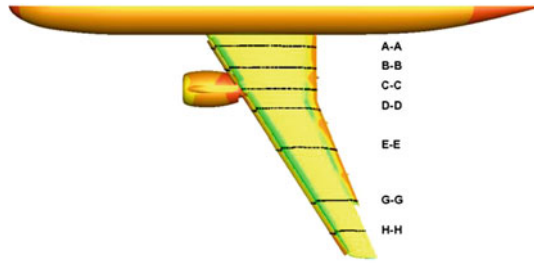
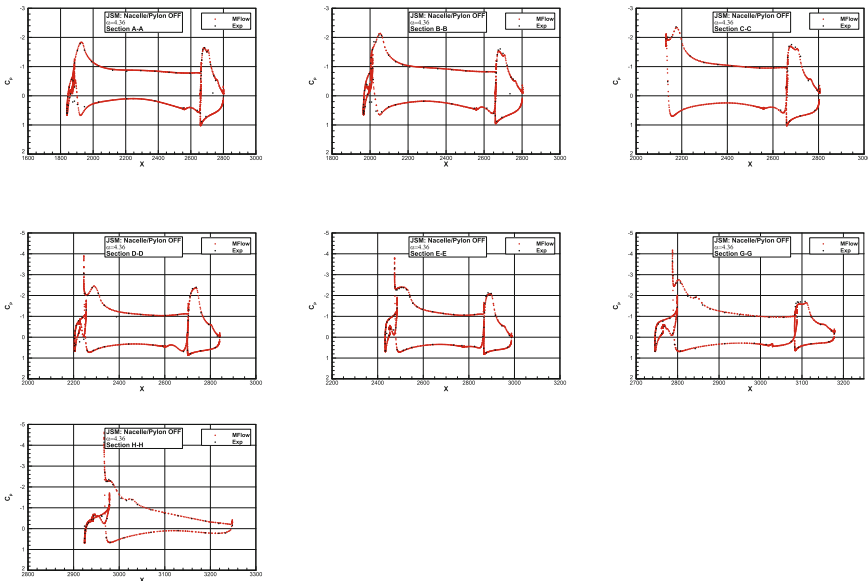**Fig. 10** Span stations where $C_p$ distributions are analyzed



**Fig. 11** $C_p$ distributions for JSM at $\alpha = 4.36°$ (Nacelle/Pylon OFF)

station H–H, where MFlow predicted too low upper-surface suction. As the angle of attack increases, the discrepancy between CFD and experiment in $C_p$ distributions extend towards inboard stations. This is extremely obvious for nacelle-and-pylon-assembled configuration. The insufficient suction on the upper surface leads to the dramatically drop of lift.

It can be expected that the predicted flow pattern on the surface is similar to the pattern in experiment at $\alpha = 4.36, 10.47, 14.54$ and $18.58°$, since the predicted lift and $C_p$ match well with experiment. This is proved by contours of skin-friction coefficient ($C_f$) and streamlines on the surface shown in Figs. 23, 24, 25, 26, 27 and 28. $C_{fx}$, which is the streamwise component of the skin-friction coefficient, can be used to identify separation regions near walls. The blue regions in the middle images denote regions with negative $C_{fx}$. The predicted flow patterns show excellent
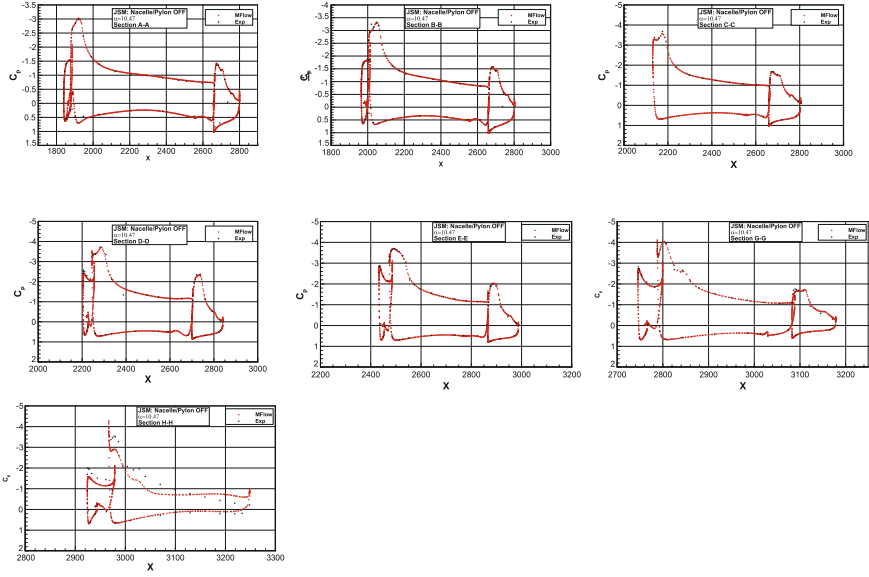
**Fig. 12** $C_p$ distributions for JSM at $\alpha = 10.47°$ (Nacelle/Pylon OFF)



**Fig. 13** $C_p$ distributions for JSM at $\alpha = 14.54°$ (Nacelle/Pylon OFF)

**Fig. 14** $C_p$ distributions for JSM at $\alpha = 18.58°$ (Nacelle/Pylon OFF)



**Fig. 15** $C_p$ distributions for JSM at $\alpha = 20.59°$ (Nacelle/Pylon OFF)

**Fig. 16** $C_p$ distributions for JSM at $\alpha = 21.57°$ (Nacelle/Pylon OFF)



**Fig. 17** $C_p$ distributions for JSM at $\alpha = 4.36°$ (Nacelle/Pylon ON)

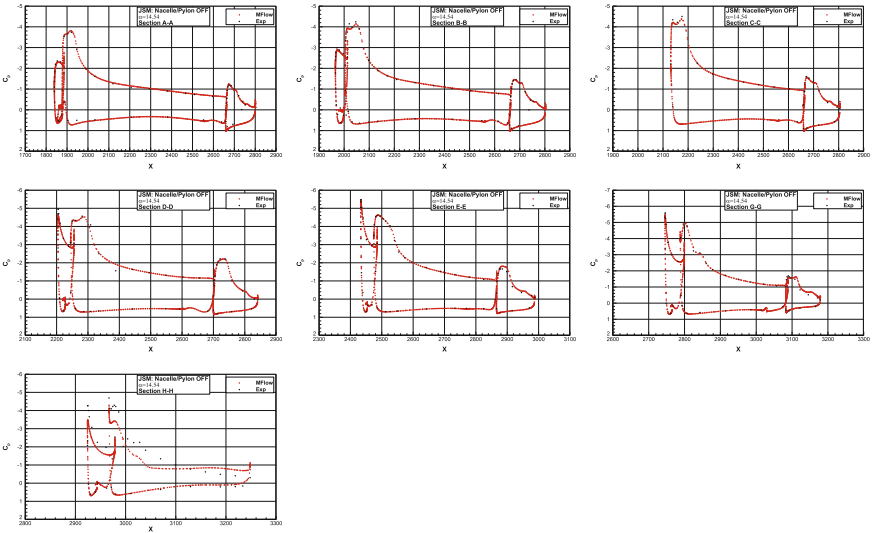**Fig. 18** $C_p$ distributions for JSM at $\alpha = 10.47°$ (Nacelle/Pylon ON)



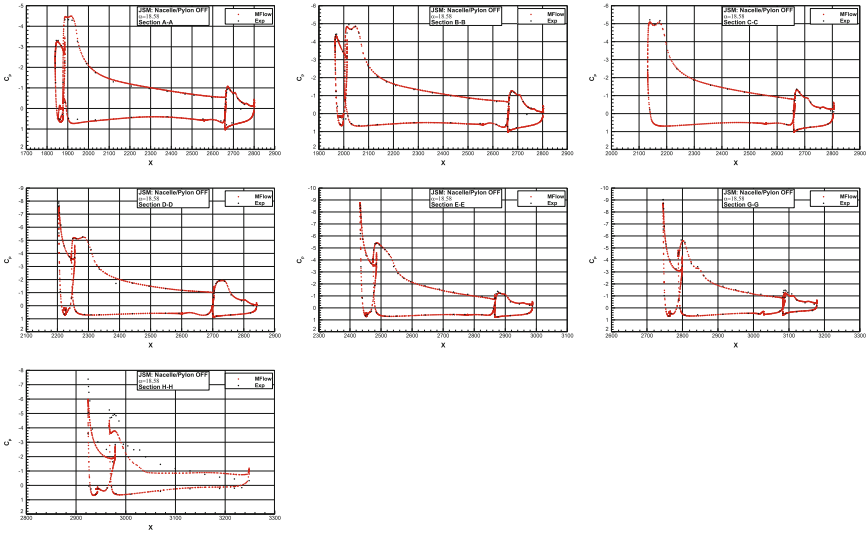**Fig. 19** $C_p$ distributions for JSM at $\alpha = 14.54°$ (Nacelle/Pylon ON)

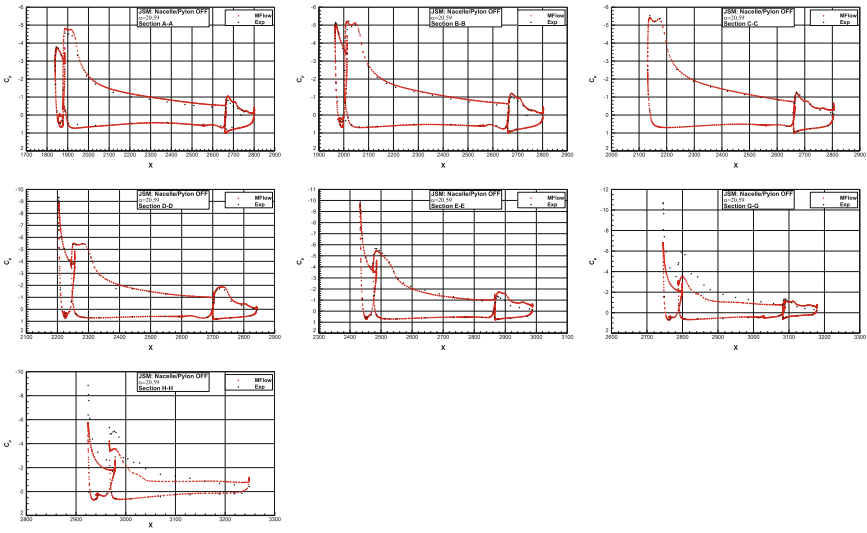**Fig. 20** $C_p$ distributions for JSM at $\alpha = 18.58°$ (Nacelle/Pylon ON)



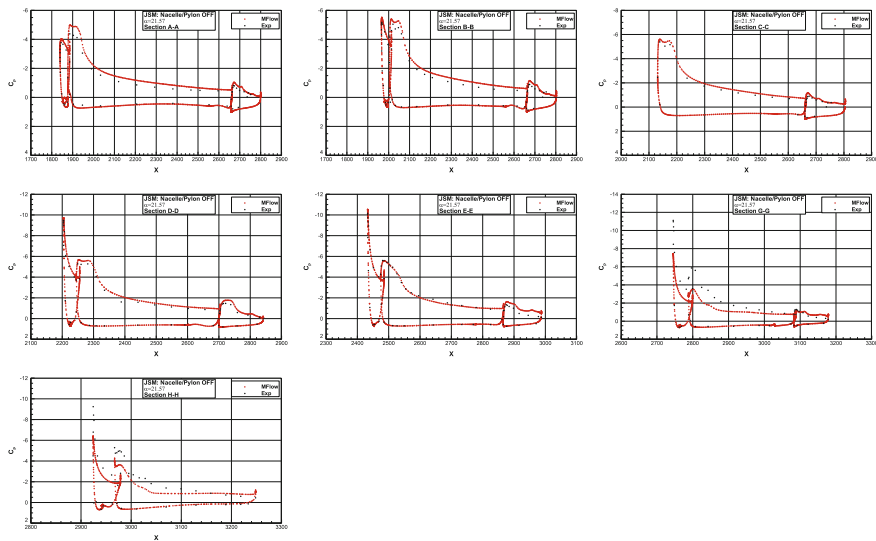**Fig. 21** $C_p$ distributions for JSM at $\alpha = 20.59°$ (Nacelle/Pylon ON)

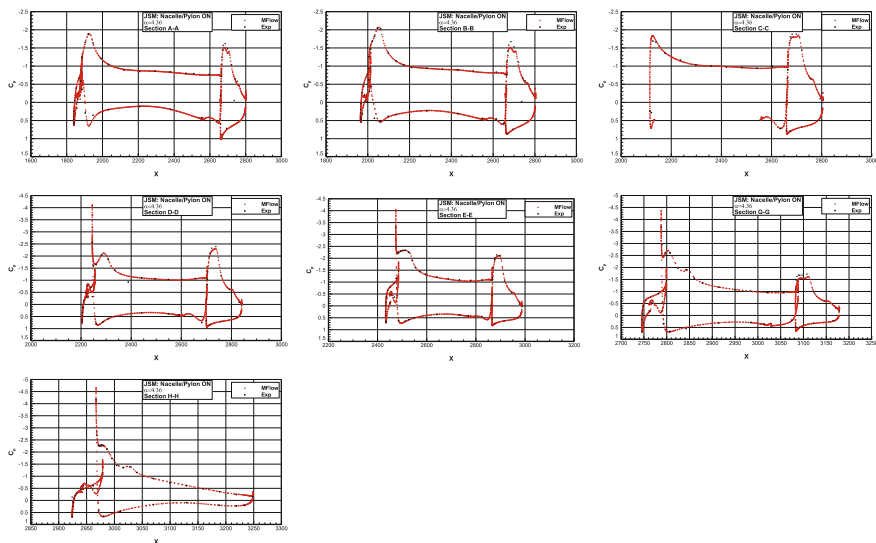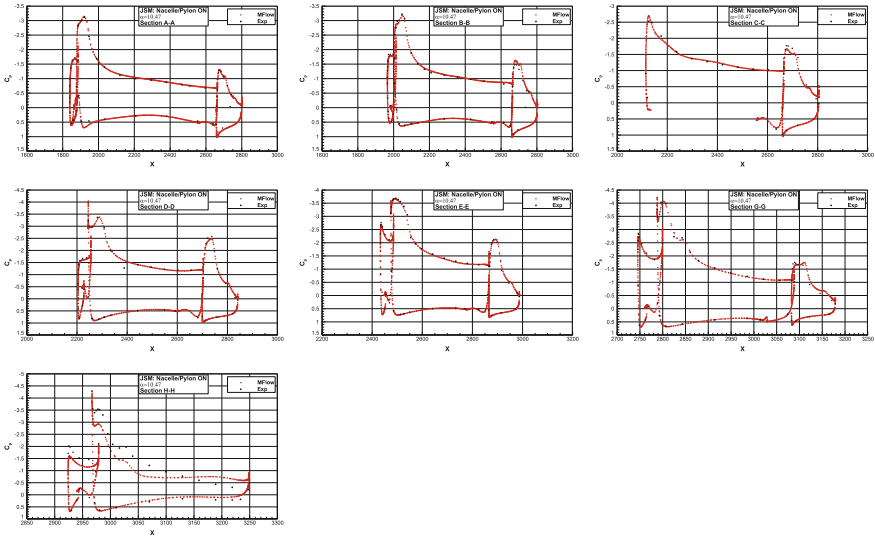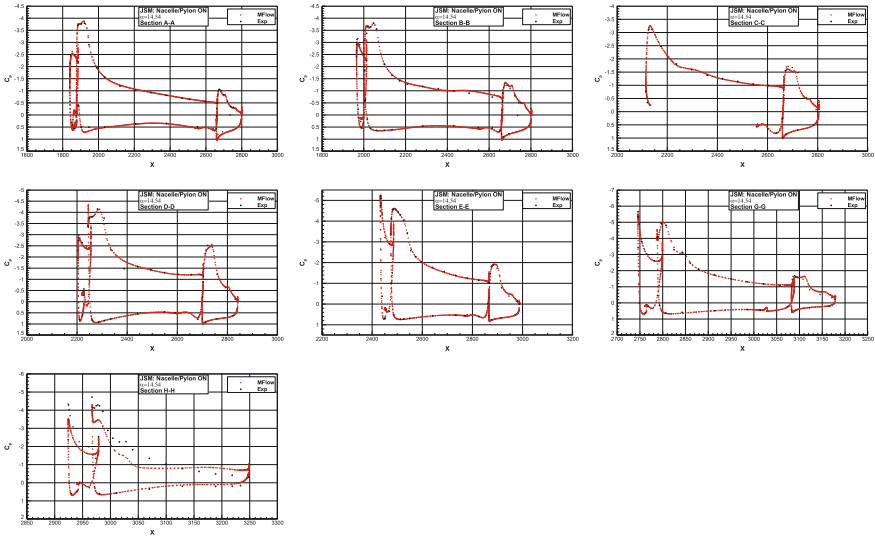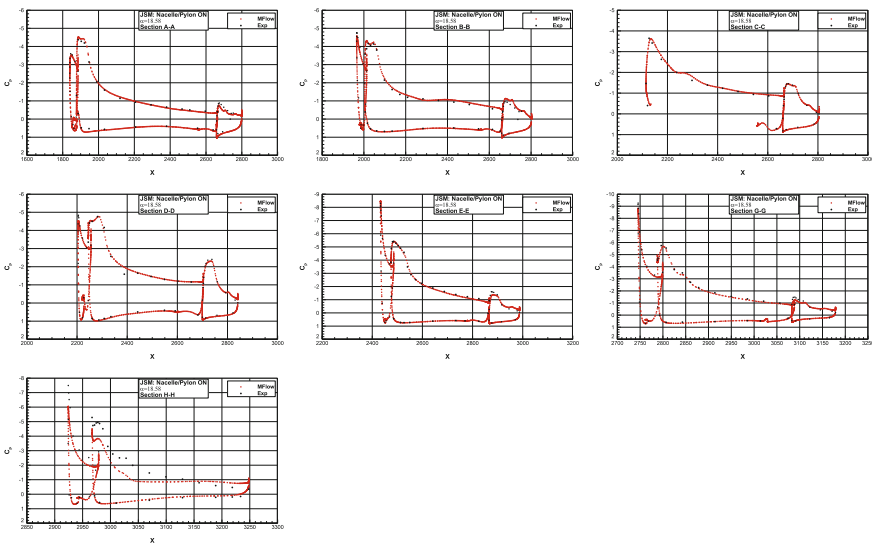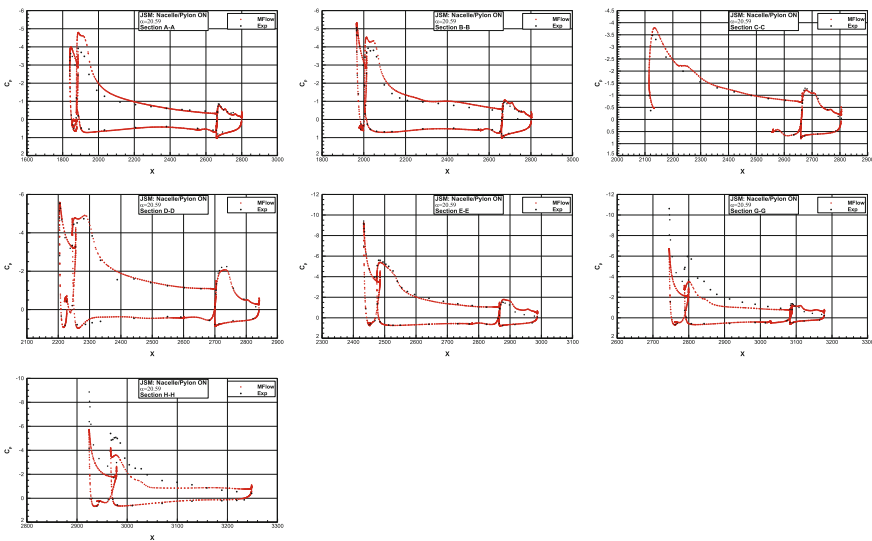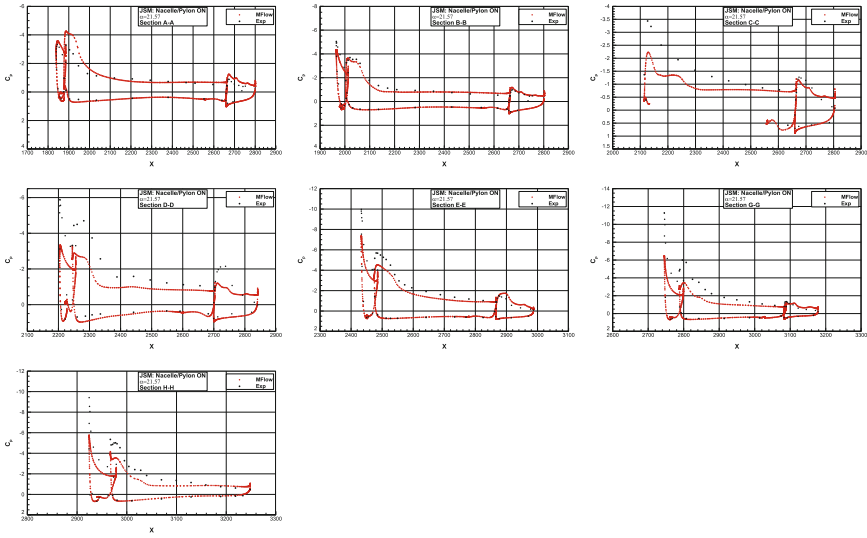**Fig. 22** $C_p$ distributions for JSM at $\alpha = 21.57°$ (Nacelle/Pylon ON)

agreement with oil flow images in experiment at $\alpha = 4.36°$, $10.47°$ and $18.58°$. Local flow separation appearing on the flap, which is more obvious at $\alpha = 4.36°$ and $10.47°$, is caused by Flap-Track-Fairings (FTFs). The flow separation due to slat support near the wingtip of the main wing begins from $\alpha = 10.47°$, however the separation is not so noticeable in experiments, judging from the oil flow image and $C_p$ distributions at H–H station. The same observation is found by several HiLiftPW-3 participants including Hidemasa Yasuda from Kawasaki Heavy Industries, Mohamed Yousuf from Boeing Research and Technology, et al.[4]

As the angle of attack increases, the separation behind the third slat support on the left causes the lift coefficient to drop earlier than in experiments.

At $\alpha = 21.57°$, lift is underpredicted for the Nacelle/Pylon ON configuration because of the large separation region behind the nacelle and pylon. However, the large separation in the wing-root region is completely underpredicted.

## 5  Conclusions

Numerical investigations of the JAXA Standard Model from the 3rd AIAA CFD High Lift Prediction Workshop are performed with the in-house solver MFlow. The load-balance problem in massively parallel computations is well handled by Metis package. Since an unstructured grid is not subjected to restrictions of topology, higher efficiency is easily achieved. The efficiency remains greater than 75%, even

---

[4]Presentations are available at https://hiliftpw.larc.nasa.gov/Workshop3/presentations.html.

**Fig. 23** Flow pattern on the surface at $\alpha = 4.36°$ (**left**: contours of $C_f$; **middle**: contours of $C_{fx}$ and streamlines; **right**: oil flow image in experiment)



**Fig. 24** Flow pattern on the surface at $\alpha = 10.47°$ (**left**: contours of $C_f$; **middle**: contours of $C_{fx}$ and streamlines; **right**: oil flow image in experiment)
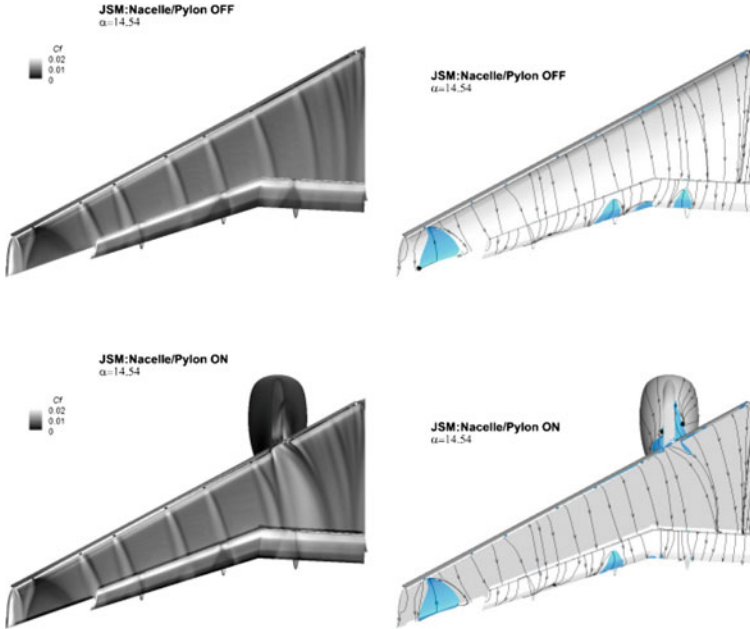
**Fig. 25** Flow pattern on the surface at $\alpha = 14.54°$ (**left**: contours of $C_f$; **right**: contours of $C_{fx}$ and streamlines)



**Fig. 26** Flow pattern on the surface at $\alpha = 18.58°$ (**left**: contours of $C_f$; **middle**: contours of $C_{fx}$ and streamlines; **right**: oil flow image in experiment)

**Fig. 27** Flow pattern on the surface at $\alpha = 20.59°$ (**left**: contours of $C_f$; **right**: contours of $C_{fx}$ and streamlines)
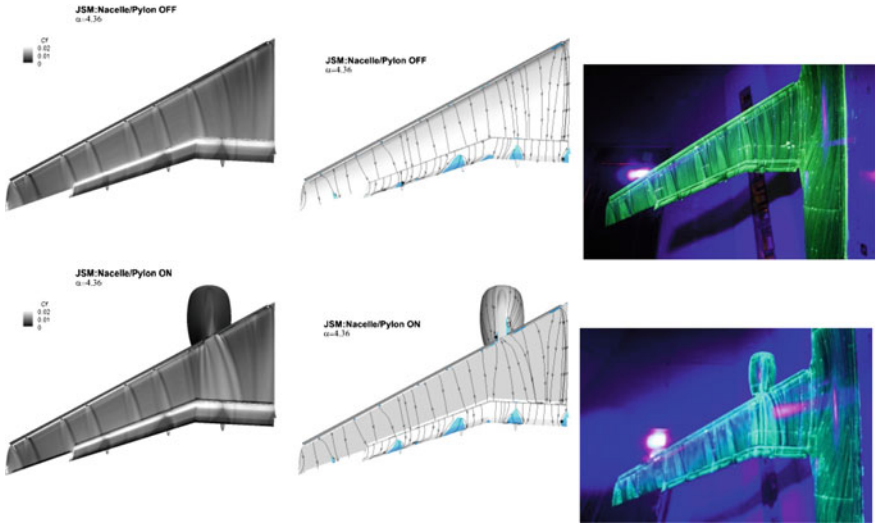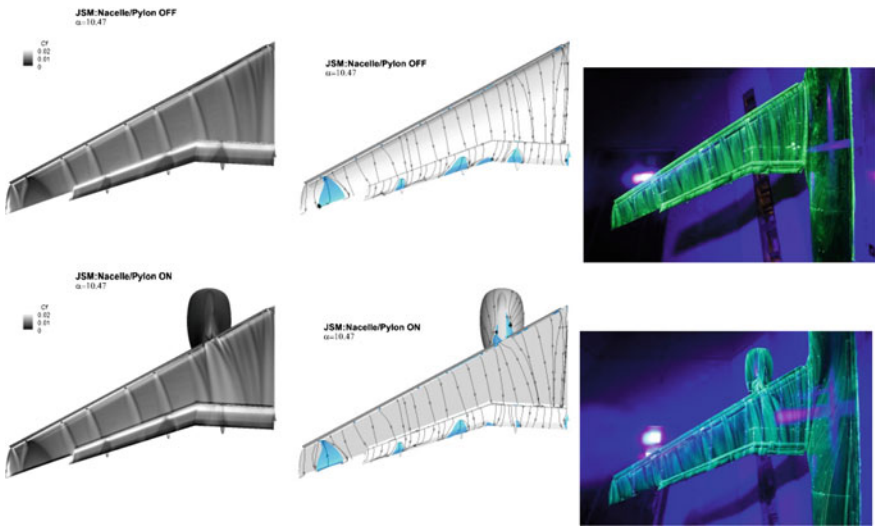


**Fig. 28** Flow pattern on the surface at $\alpha = 21.57°$ (**left**: contours of $C_f$; **middle**: contours of $C_{fx}$ and streamlines; **right**: oil flow image in experiment)
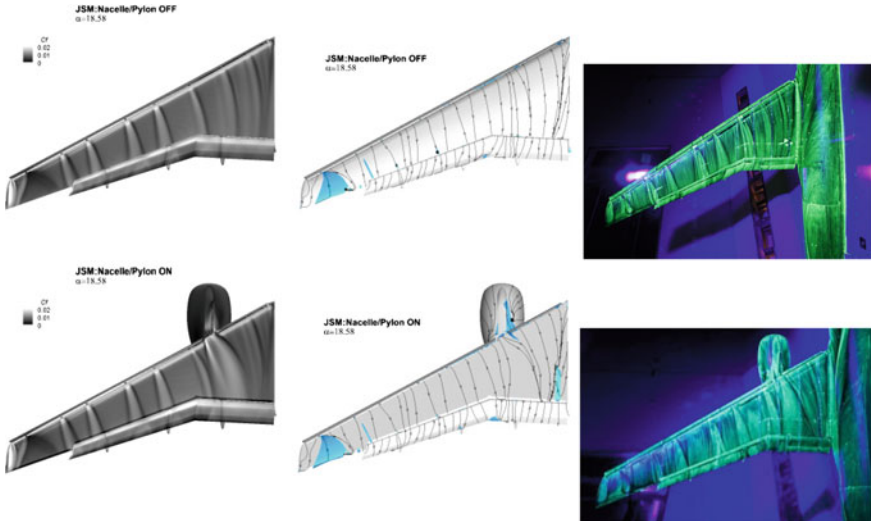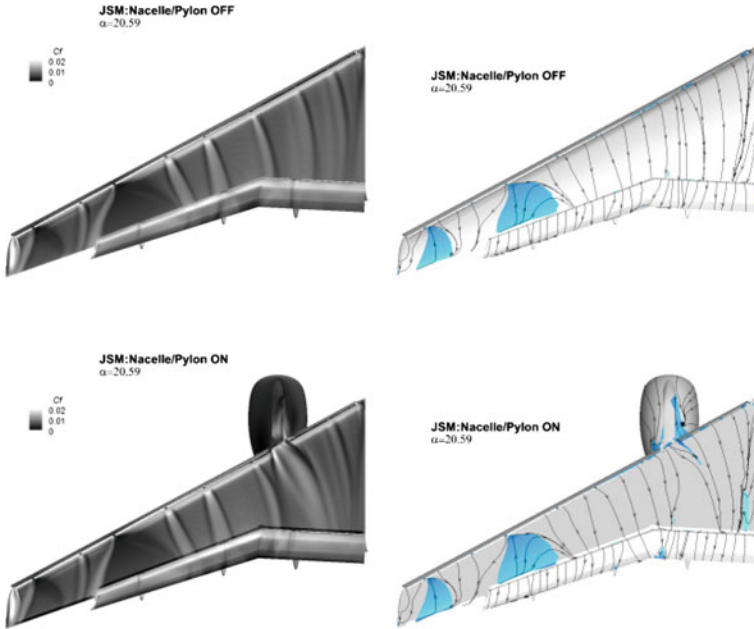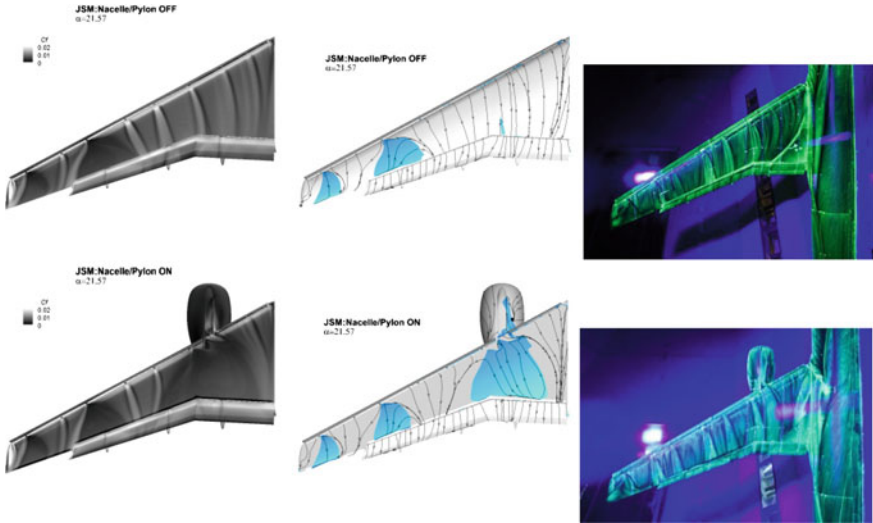
for computation on 6,400 processors. The current speedup rate deviates obviously from the theoretical rate only for computations on 3,200 or more processors.

The force and moment prediction initiated with a converged flow field obtained at a lower angle of attack achieves better agreement with experiment compared with predictions initiated with freestream values, in terms of larger maximum-lift coefficients. The drag-and-pitching-moment prediction is also improved. The increment in drag due to nacelle and pylon added is well-predicted at small to medium angles of attack, but drops earlier than in experiments. The prediction of the increment in lift-and-pitching moment is not particularly satisfactory, especially near stall.

The predicted $C_p$ agrees well with experiment, at small-to-medium angles of attack, except at the outboard-most span station, where MFlow predicted too low upper-surface suction. As the angle of attack increases, the discrepancy between CFD and experiment in $C_p$ distributions extend towards inboard stations. This is extremely obvious for nacelle-and-pylon-assembled configurations. The insufficient suction on the upper surface leads to the dramatic drop in lift near stall.

The solver shows good agreement with experiment at lower angles of attack, but more attention is needed at angles of attack near and beyond stall.

# References

1. van Dam, C.P.: The aerodynamic design of multi-element high-lift systems for transport airplanes. Prog. Aerosp. Sci **38**(2), 101–144 (2002). https://doi.org/10.1016/S0376-0421(02)00002-7
2. Rumsey, C.L., Ying, S.X.: Prediction of high-lift: review of present CFD capability. Prog. Aerosp. Sci. **38**(2), 145–180 (2002). https://doi.org/10.1016/S0376-0421(02)00003-9
3. Rumsey, C.L., Long, M., Stuever, R.A., Wayman, T.R.: Summary of the First AIAA CFD High-lift Prediction Workshop, 49th AIAA Aerospace Sciences Meeting, AIAA Paper 2011-0939, Jan 2011
4. Long, M., Mavriplis, D.: NSU3D Results for the First AIAA High-lift Prediction Workshop, 49th AIAA Aerospace Sciences Meeting, AIAA Paper 2011-0863, Jan 2011
5. Park, M.A., Lee-Rausch, E.M., Rumsey, C.L.: FUN3D and CFL3D Computations for the First High-Lift Prediction Workshop, 49th AIAA Aerospace Sciences Meeting, AIAA Paper 2011-0936, Jan 2011
6. Crippa, S., Wilkendingy, S.M., Rudnik, R.: DLR Contribution to the First High-lift Prediction Workshop, 49th AIAA Aerospace Sciences Meeting, AIAA Paper 2011-938, Jan 2011
7. Sclafani, A.J., Slotnick, J.P., Vassberg, J.C., Pulliam, T.H., Lee, H.C.: OVERFLOW Analysis of the NASA Trap Wing Model from the First High-lift Prediction Workshop, 49th AIAA Aerospace Sciences Meeting, AIAA Paper 2011-866, Jan 2011
8. Johnson, P.L., Jones, K.M., Madson, M.D.: Experimental investigation of a simplified 3D high-lift configuration in support of CFD validation. In: 18th Applied Aerodynamics Conference, AIAA Paper 2000-4217, Aug 2000
9. Hannon, J.A., Washburn, A.E., Jenkins, L.N., Watson, R.D.: Trapezoidal wing experimental repeatability and velocity profiles in the 14- by 22-foot subsonic tunnel (Invited). In: 50th AIAA Aerospace Sciences Meeting, AIAA Paper 2012-0706, Jan 2012
10. Rumsey, C.L., Slotnick, J.P., Long, M., Stuever, R.A., Wayman, T.R.: Summary of the first AIAA CFD high-lift prediction workshop. J. Aircr. **48**(6), 2068–2079 (2011). https://doi.org/10.2514/1.C031447

11. Rumsey, C.L., Slotnick, J.P.: Overview and summary of the second AIAA high-lift prediction workshop. J. Aircr. **52**(4), 1006–1025 (2015)
12. Murayama, M., Yamamoto, K., Ito, Y., Hirai, T., Tanaka, K.: Japan aerospace exploration agency studies for the second high-lift prediction workshop. J. Aircr. **52**(4), 1026–1041 (2015)
13. Chen, J.T., Zhang, Y.B., Zhou, N.C., Deng, Y.Q.: Numerical investigations of the high-lift configuration with MFlow solver. J. Aircr. **52**(4), 1051–1062 (2015)
14. Mavriplis, D., Long, M., Lake, T., Langlois, M.: NSU3D results for the second AIAA high-lift prediction workshop. J. Aircr. **52**(4), 1063–1081 (2015)
15. Coder, J.G.: OVERFLOW analysis of the DLR-F11 high-lift configuration including transition modeling. J. Aircr. **52**(4), 1082–1097 (2015)
16. Lee-Rausch, E.M., Rumsey, C.L., Park, M.A.: Grid-adapted FUN3D computations for the second high-lift prediction workshop. J. Aircr. **52**(4), 1098–1111 (2015)
17. Escobar, J.A., Suarez, C.A., Silva, C., López, O.D., Velandia, J.S., Lara, C.A.: Detached-Eddy simulation of a wide-body commercial aircraft in high-lift configuration. J. Aircr. **52**(4), 1112–1121 (2015)
18. Blazek, J.: Computational Fluid Dynamics: Principles and Applications, pp. 1–4. Elsevier Science Ltd., Oxford (2001)
19. Ito, T., Yokokawa, Y., Ura, H., Kato, H., Mitsuo, K., Yamamoto, K.: High-lift device testing in JAXA 6.5M X 5.5M low-speed wind tunnel. In: AIAA Paper 2006-3643 (2006)
20. Yokokawa, Y., Murayama, M., Ito, T., Yamamoto, K.: Experiment and CFD of a high-lift configuration civil transport aircraft model. In: AIAA Paper 2006-3452 (2006)
21. Yokokawa, Y., Murayama, M., Uchida, H., Tanaka, K., Ito, T., Yamamoto, K.: Aerodynamic influence of a half-span model installation for high-lift configuration experiment. In: 48th AIAA Aerospace Sciences Meeting, AIAA paper 2010-684, Jan 2010
22. Diskin, B., Thomas, J. L.: Comparison of node-centered and cell-centered unstructured finite volume discretizations: inviscid fluxes. AIAA J. **49**(4), 836–854 (2011). https://doi.org/10.2514/1.J050897
23. Venkatakrishnan, V.: On the accuracy of limiters and convergence to steady-state solutions. In: 31st Aerospace Sciences Meeting, AIAA Paper 1993-0880, Jan 1993
24. Weiss, J.M., Smith, W.A.: Preconditioning applied to variable and constant density flows. AIAA J. **33**(11), 2050–2057 (1995). https://doi.org/10.2514/3.12946
25. Spalart, P.R., Allmaras, S.R.: A one-equation turbulence model for aerodynamic flows. In: 30th Aerospace Sciences Meeting and Exhibit, AIAA Paper 1992-0439, Jan 1992. https://doi.org/10.2514/6.1992-439
26. Karypis, G., Kumar, V.: A fast and high quality multilevel scheme for partitioning irregular graphs. SIAM J. Sci. Comput. **20**(1), 359–392 (1998)
27. Sheke, S., Kalyan, W.: Parallel multigrid solver for Navier-Stokes equation using OpenMPI. Int. J. Comput. Sci. Trends Technol. **3**(5), 131–134 (2015)
28. Berger, M.J., Aftosmis, M.J., Marshall, D.D.: Performance of a new CFD Flow solver using a hybrid programming paradigm. J. Parallel Distrib. Comput. **65**(4), 414–423 (2005)

# Time-Resolved Adaptive Direct FEM Simulation of High-Lift Aircraft Configurations

**Johan Jansson, Ezhilmathi Krishnasamy, Massimiliano Leoni, Niclas Jansson and Johan Hoffman**

**Abstract** We present an adaptive finite element method for time-resolved simulation of aerodynamics without any turbulence-model parameters, which is applied to a benchmark problem from the HiLiftPW-3 workshop to compute the flow past a JAXA Standard Model (JSM) aircraft model at realistic Reynolds numbers. The mesh is automatically constructed by the method as part of an adaptive algorithm based on a posteriori error estimation using adjoint techniques. No explicit turbulence model is used, and the effect of unresolved turbulent boundary layers is modeled by a simple parametrization of the wall shear stress in terms of a skin friction. In the case of very high Reynolds numbers, we approximate the small skin friction by zero skin friction, corresponding to a free-slip boundary condition, which results in a computational model without any model parameter to be tuned, and without the need for costly boundary-layer resolution. We introduce a numerical tripping-noise term to act as a seed for growth of perturbations; the results support that this triggers the correct physical separation at stall and has no significant pre-stall effect. We show that the methodology quantitavely and qualitatively captures the main features of the JSM experiment—aerodynamic forces and the stall mechanism—with a much coarser mesh resolution and lower computational cost than the state-of-the-art methods in the field, with convergence under mesh refinement by the adaptive method. Thus, the

J. Jansson (✉) · E. Krishnasamy · M. Leoni · N. Jansson · J. Hoffman
Computational Science and Technology CSC, KTH, SE-100 44 Stockholm, Sweden
e-mail: jjan@kth.se

E. Krishnasamy
e-mail: ekrishnasamy@bcamath.org

M. Leoni
e-mail: mleoni@kth.se

N. Jansson
e-mail: njansson@kth.se

J. Hoffman
e-mail: jhoffman@kth.se

J. Jansson · E. Krishnasamy · M. Leoni
BCAM - Basque Center for Applied Mathematics, Bilbao, Spain

simulation methodology appears to be a possible answer to the challenge of reliably predicting turbulent-separated flows for a complete air vehicle.

## Nomenclature

| | |
|---|---|
| $C_l$ | lift coefficient (dimensionless) |
| $C_d$ | drag coefficient (dimensionless) |
| $C_p$ | pressure coefficient (dimensionless) |
| $h$ | diameter of tetrahedron in finite element mesh (m) |
| $k$ | time step (s) |
| $\mathbf{n}$ | normal unit vector (dimensionless) |
| $P$ | computed pressure (Pa) |
| $p$ | pressure (Pa) |
| $q$ | pressure test function (Pa) |
| $Re$ | Reynolds number (dimensionless) |
| $t$ | time variable (s) |
| $T$ | end time (s) |
| $\mathbf{U}$ | computed velocity ($\mathrm{m\,s^{-1}}$) |
| $\mathbf{u}$ | velocity ($\mathrm{m\,s^{-1}}$) |
| $\mathbf{v}$ | velocity test function ($\mathrm{m\,s^{-1}}$) |
| $\mathbf{x}$ | space variable (m) |
| $\alpha$ | angle of attack (dimensionless) |
| $\beta$ | friction parameter ($\mathrm{kg\,m^{-2}\,s^{-1}}$) |
| $\nu$ | kinematic viscosity ($\mathrm{m^2\,s^{-1}}$) |
| $\boldsymbol{\tau}$ | tangent unit vector (dimensionless) |

## 1  Introduction

The main challenge today in Computational Fluid Dynamics (CFD) for aerodynamics is to reliably predict turbulent-separated flows [32, 35], specifically for a complete air vehicle. This is our focus in this chapter.

We present an adaptive finite element method without turbulence modeling parameters for time-resolved simulation of aerodynamics, together with results stemming from the 3rd AIAA CFD High Lift Prediction Workshop (HiLiftPW-3), which was held in Denver, Colorado, on June 3–4 2017. The benchmark was a high-lift configuration of the JSM aircraft model shown in Fig. 1 at a Reynolds number realistic for flight conditions. The purpose of the workshop is to assess the capability of state-of-the-art CFD codes and methods.

Turbulent flows present features over a range of scales, from the scale of the aircraft down to the Kolmogorov dissipation scale. Direct numerical simulation (DNS) is not feasible for a full aircraft at realistic Reynolds numbers, instead the Reynolds

(a) Surface mesh

(b) Pylon

(c) Volume mesh

(d) Wing slice
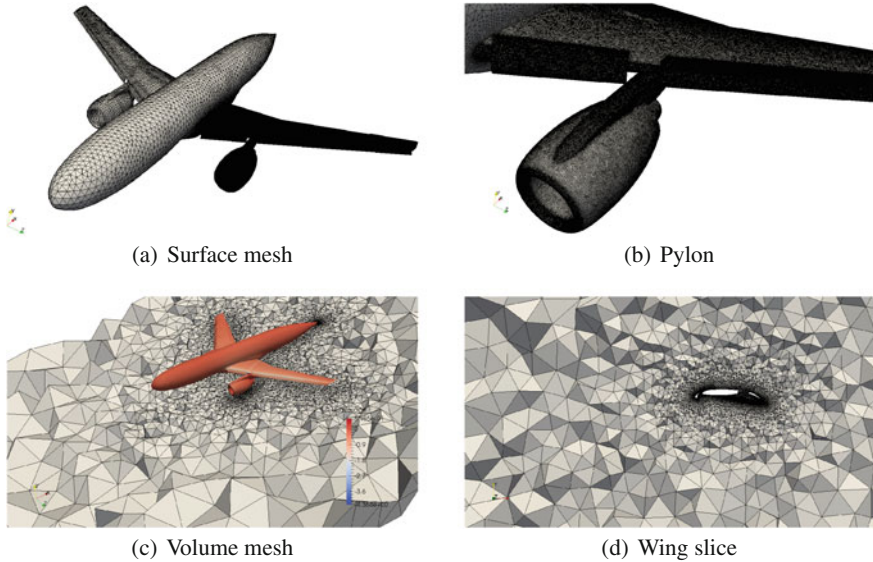
**Fig. 1** Overview of the JSM aircraft model and the starting mesh for the adaptive method

Averaged Navier–Stokes equations (RANS) have long been the state of the art in industry [31]. RANS methods do not provide a full resolution of the flow field but simulate the mean field and introduce turbulence models to make up for the unresolved dynamics. In particular, standard RANS do not resolve the transient flow field, but a statistical average of the turbulent flow.

In contrast, Large Eddy Simulations (LES) [29] resolve the dynamics of a filtered flow field, at the cost of higher mesh resolution than RANS, with subgrid models for unresolved scales. Both RANS and LES, and hybrids such as DES, introduce model parameters that need to be tuned to the problem at hand, and the results are highly sensitive to the design of the computational mesh [19, 25–27, 33]. In particular, turbulent boundary layers cannot be resolved and must be modelled. Boundary-layer models require tailored boundary-layer meshes, which are expensive in terms of both mesh density and manual work. Witherden and Jameson in [35] state that "as a community we are still far away from LES of a complete air vehicle".

The method we present is an adaptive finite element method without an explicit turbulence model and boundary layer model, thus without model parameters and without the need for a boundary-layer mesh. The mesh is automatically constructed by the method as part of the computation through an adaptive procedure based on a posteriori error estimation using adjoint techniques. Dissipation of turbulent kinetic energy is provided by residual-based numerical stabilization. The method is thus purely based on the Navier–Stokes equations, and no other modeling assumptions are made.

We model the effect of turbulent boundary layers by a parametrization of the wall shear stress in terms of a skin friction. For very high Reynolds numbers we approximate the small skin friction by zero skin friction, corresponding to a free-slip boundary condition, which results in a computational method without any model parameters that need to be tuned, and without the need for costly boundary-layer resolution.

In this chapter, we give the main components of the simulation methodology, and we present our results stemming from the HiLiftPW-3, where we highlight the non-standard aspects of the methodology and discuss the results in relation to the experiments. The HiLiftPW-3 specified two variants of the JSM: one without pylon (or nacelle) and one with the pylon included in the geometry ("pylon on"). The difference in the aerodynamic forces between the two variants measured in experiments is small, typically less than 2%. For this reason we will focus only on the "pylon on" variant with the aim of validating our methodology.

The workshop guidelines prescribed the study of these two variants either with a fixed mesh or, more interestingly, using mesh adaptation techniques. Considering the nature of our method, which intimately depends on its adaptive procedure, we concentrated on the latter study. We did not use the provided computational meshes, but instead generated more suitable ones for our methodology starting from the provided CAD files. We would like to point out that our adaptive methodology does not require any ad-hoc meshing procedure aimed at helping the solver identify flow features that are qualitatively known before starting the computations. Not only does this simplify the meshing procedure, which can now be carried out by non-specialized software (and scientists), but it also makes it faster: the only thing that we need is an initial mesh that captures the geometry of the object; this is due to the fact that the generated mesh loses memory of the underlying CAD model, and therefore the refinement of boundary triangles cannot correct a rough initial approximation of the CAD geometry. We plan to get rid of this constraint in the near future, implementing the functionality to refine boundary cells with the new vertices projected on the CAD model. Once we have a sufficiently accurate surface description, however, we can let the mesh be coarse in the volume part, which will be refined iteratively by the adaptive algorithm.

This convenient approach enables us to perform computations starting with rather coarse meshes, increasing the number of cells only where needed in order to best utilize the available computational resources. Our initial mesh for the JSM case has about $2.5 \times 10^6$ cells.

We find that the simulation results compare very well with experimental data for all the angles of attack that we studied; moreover, we show mesh convergence by the adaptive method, while using a relatively low number of spatial degrees of freedom. The low computational cost also allows for a time-resolved simulation, which provides additional results that cannot be obtained from a stationary simulation, such as the ones based on RANS.

Thus, the simulation methodology appears to be a possible answer to the challenge of reliably predicting turbulent-separated flows for a complete air vehicle. Specifically, we present here simulation results reproducing the physically correct stall

mechanism of large-scale separation at the wing-body juncture, which is promising for our continuing work on validating the methodology.

## 2  Simulation Methodology

In contrast to the statistical averages of RANS and the filtered solutions of LES, our simulation method is based on computational approximation of weak solutions to the Navier–Stokes equations (NSE) that satisfy the NSE in a variational form integrated over a class of test functions.

Finite element methods (FEM) are based on a variational form of the NSE, and, if the method satisfies certain conditions on stability and consistency, the FEM solutions converge towards a weak solution to the NSE as the finite element mesh is refined [8]. We refer to such FEM as a General Galerkin (G2) method, or a Direct Finite Element Simulation (DFS).

The resolution in DFS is set by the mesh size, and no turbulence model is introduced. Dissipation of turbulent kinetic energy in underresolved parts of the flow is provided by the numerical stabilization of G2 in the form of a weighted least squares method based on the residual of NSE.

The mesh is adaptively constructed based on a posteriori estimation of the error in chosen goal or target functionals, such as drag and lift forces. The a posteriori error estimates take the form of a residual weighted by the solution of an adjoint problem, which is computed separately using a similar stabilized FEM method [8]. The adaptive algorithm starts from a coarse mesh, which is locally refined at each iteration based on the a posteriori error estimates.

We use a free-slip boundary condition as a model for high-Reynolds-number turbulent boundary layers with small skin friction. This means that boundary layers are left unresolved, and that no boundary layer mesh is needed.

This methodology has been validated on a number of standard benchmark problems in the literature [2–4, 7], including for an aircraft model for the HiLiftPW-2 [14], and we find that, also for the benchmark considered in this chapter, the method is very efficient and provides results close to the experimental reference data.

We have used a low-order finite-element discretization on unstructured tetrahedral meshes, which we refer to as cG(1)cG(1), i.e., continuous piecewise linear approximation in space and time.

### 2.1  The cG(1)cG(1) Method

As the basic model for incompressible Newtonian fluid flow, we consider the NSE with constant kinematic viscosity $\nu > 0$, enclosed in $\Omega \subset \mathbb{R}^3$, with boundary $\Gamma$, over a time interval $I = [0, T]$:

$$\begin{cases} \dot{\mathbf{u}} + (\mathbf{u} \cdot \nabla)\mathbf{u} + \nabla p - 2\nu\nabla \cdot \varepsilon(\mathbf{u}) = f, & (\mathbf{x}, t) \in \Omega \times I, \\ \nabla \cdot \mathbf{u} = 0, & (\mathbf{x}, t) \in \Omega \times I, \\ \mathbf{u}(\mathbf{x}, 0) = \mathbf{u}^0(\mathbf{x}), & \mathbf{x} \in \Omega, \end{cases} \quad (1)$$

with $\mathbf{u}(\mathbf{x}, t)$ the velocity vector, $p(\mathbf{x}, t)$ the pressure, $\mathbf{u}^0(\mathbf{x})$ the initial data and $f(\mathbf{x}, t)$ a body force. Moreover, $\sigma_{ij} = 2\nu\varepsilon_{ij}(\mathbf{u}) - p\delta_{ij}$ is the stress tensor, with the strain-rate tensor $\varepsilon_{ij}(\mathbf{u}) = 1/2(\partial u_i/\partial x_j + \partial u_j/\partial x_i)$, and $\delta_{ij}$ the Kronecker delta. The relative importance of viscous and inertial effects in the flow is determined by the Reynolds number $Re = UL/\nu$, where $U$ and $L$ are characteristic velocity and length scales.

The cG(1)cG(1) method is based on the continuous Galerkin method cG(1) in space and time. With cG(1) in time, the trial functions are continuous, piecewise linear and the test functions piecewise constant. cG(1) in space corresponds to both test functions and trial functions being continuous, piecewise linear.

Let $0 = t_0 < t_1 < ... < t_N = T$ be a sequence of discrete time steps, with associated time intervals $I_n = (t_{n-1}, t_n)$ of length $k_n = t_n - t_{n-1}$, and let $W \subset H^1(\Omega)$ be a finite element space consisting of continuous, piecewise linear functions on a tetrahedral mesh $\mathscr{T} = \{K\}$ of mesh size $h(\mathbf{x})$, with $W_{\mathbf{w}}$ the functions $\mathbf{v} \in W$ satisfying the Dirichlet boundary condition $\mathbf{v}|_\Gamma = \mathbf{w}$.

We seek $\hat{\mathbf{U}} = (\mathbf{U}, P)$, continuous piecewise linear in space and time, and the cG(1)cG(1) method for the NSE with homogeneous Dirichlet boundary conditions reads: for $n = 1, ..., N$ find $(\mathbf{U}^n, P^n) \equiv (\mathbf{U}(t_n), P(t_n))$, with $\mathbf{U}^n \in V_0 \equiv [W_0]^3$ and $P^n \in W$, such that:

$$\begin{aligned} &((\mathbf{U}^n - \mathbf{U}^{n-1})k_n^{-1} + \bar{\mathbf{U}}^n \cdot \nabla\bar{\mathbf{U}}^n, \mathbf{v}) + (2\nu\varepsilon(\bar{\mathbf{U}}^n), \varepsilon(\mathbf{v})) - (P^n, \nabla \cdot \mathbf{v}) \\ &+ (\nabla \cdot \bar{\mathbf{U}}^n, q) + SD_\delta^n(\bar{\mathbf{U}}^n, P^n; \mathbf{v}, q) = (f, \mathbf{v}), \quad \forall\hat{\mathbf{v}} = (\mathbf{v}, q) \in V_0 \times W, \end{aligned} \quad (2)$$

where $\bar{\mathbf{U}}^n = \frac{1}{2}(\mathbf{U}^n + \mathbf{U}^{n-1})$ is piecewise constant in time over $I_n$, with the stabilizing term

$$\begin{aligned} SD_\delta^n(\bar{\mathbf{U}}^n, P^n; \mathbf{v}, q) \equiv & \quad (3) \\ (\delta_1(\bar{\mathbf{U}}^n \cdot \nabla\bar{\mathbf{U}}^n &+ \nabla P^n - f), \bar{\mathbf{U}}^n \cdot \nabla\mathbf{v} + \nabla q) + (\delta_1\nabla \cdot \bar{\mathbf{U}}^n, \nabla \cdot \mathbf{v}), \end{aligned}$$

and

$$(\mathbf{v}, \mathbf{w}) = \sum_{K \in \mathscr{T}} \int_K \mathbf{v} \cdot \mathbf{w} \, dx,$$

$$(\varepsilon(\mathbf{v}), \varepsilon(\mathbf{w})) = \sum_{i,j=1}^3 (\varepsilon_{ij}(\mathbf{v}), \varepsilon_{ij}(\mathbf{w})),$$

with the stabilization parameter $\delta_1 = \kappa_1 h$, where $\kappa_1$ is a positive constant of unit size. We choose a time step size $k_n = C_{CFL} \min_{\mathbf{x} \in \Omega} h/|\mathbf{U}^{n-1}|$, with $C_{CFL}$ typically in the range $[0.5, 20]$. The resulting non-linear algebraic equation system is solved with a robust Schur-type fixed-point iteration method [18].

## 2.2   The Adaptive Algorithm

A simple description of the adaptive algorithm, starting from $i = 0$, reads:

1. For the mesh $\mathscr{T}_i$: solve the primal and (linearized) dual problems for the primal solution $(\mathbf{U}, P)$ and the dual solution $(\Phi, \Theta)$.
2. Compute the quantity $\mathscr{E}_K$ for any cell $K$ of $\mathscr{T}_i$. If $\sum_{K \in \mathscr{T}_i} \mathscr{E}_K < TOL$ then stop, else:
3. Mark 5% of the elements with highest $\mathscr{E}_K$ for refinement.
4. Generate the refined mesh $\mathscr{T}_{i+1}$, and goto 1.

Here, $\mathscr{E}_K$ is the *error indicator* for each cell $K$, which we describe in Sect. 2.3. For now, it suffices to say that $\mathscr{E}_K$ is a function of the residual of the NSE and of the solution of a linearized dual problem. The formulation of the dual problem includes the definition of a *target functional* for the refinement, which usually enters the dual equations as a boundary condition or as a volume source term. This functional should be chosen according to the problem we are solving. In other words, one needs to ask the right question in order to obtain the correct answer from the algorithm. In this chapter, our target functional is chosen to be the mean value in time of the aerodynamic forces.

The dual problem can be written as (see [6] for more details):

$$
\begin{cases}
-\dot{\boldsymbol{\varphi}} - (\mathbf{u} \cdot \nabla)\boldsymbol{\varphi} + \nabla \mathbf{U}^\top \boldsymbol{\varphi} + \nabla\theta - \nu\Delta\boldsymbol{\varphi} = \psi_1 & (\mathbf{x}, t) \in \Omega \times I \\
\nabla \cdot \boldsymbol{\varphi} = \psi_2 & (\mathbf{x}, t) \in \Omega \times I \\
\boldsymbol{\varphi} = \psi_3 & (\mathbf{x}, t) \in \Gamma \times I \\
\boldsymbol{\varphi}(\cdot, T) = \psi_4 & \mathbf{x} \in \Omega,
\end{cases}
\tag{4}
$$

where we find that the structure is similar to the primal NSE equations, except that the adjoint problem is linear, the transport is backward in time, and that we have a reaction term $(\nabla \mathbf{U}^\top \boldsymbol{\varphi})_j = U_{,j} \cdot \boldsymbol{\varphi}$, not present in the primal NSE.

The only other input required from the user is an initial discretization of the geometry, $\mathscr{T}_0$. Since our method is designed for tetrahedral meshes that do not require any special treatment of the near-wall region (no need for a boundary-layer mesh), the initial mesh can be easily created with any standard mesh-generation tool.

## 2.3   A Posteriori Error Estimate for cG(1)cG(1)

The a posteriori error estimate is based on the following theorem (for a detailed proof, see Chap. 30 in [8]):

**Theorem 1**  *If $\hat{\mathbf{U}} = (\mathbf{U}, P)$ solves (2), $\hat{\mathbf{u}} = (\mathbf{u}, p)$ is a weak NSE solution, and $\hat{\boldsymbol{\varphi}} = (\boldsymbol{\varphi}, \theta)$ solves an associated dual problem with data $M(\cdot)$, then we have the following a posteriori error estimate for the target functional $M(\hat{\mathbf{U}})$ with respect to the reference functional $M(\hat{\mathbf{u}})$:*

$$|M(\hat{\mathbf{u}}) - M(\hat{\mathbf{U}})| \leq \sum_{n=1}^{N} \left[ \int_{I_n} \sum_{K \in \mathscr{T}_i} |R_1(\mathbf{U}, P)_K| \cdot \omega_1 \, dt \right.$$

$$\left. + \int_{I_n} \sum_{K \in \mathscr{T}_i} |R_2(\mathbf{U})_K| \, \omega_2 \, dt + \int_{I_n} \sum_{K \in \mathscr{T}_i} |SD_\delta^n(\hat{\mathbf{U}}; \hat{\boldsymbol{\varphi}})_K| \, dt \right] =: \sum_{K \in \mathscr{T}_i} \mathscr{E}_K$$

*with*

$$R_1(\mathbf{U}, P) = \dot{\mathbf{U}} + (\mathbf{U} \cdot \nabla)\mathbf{U} + \nabla P - 2\nu\nabla \cdot \varepsilon(\mathbf{u}) - f,$$
$$R_2(\mathbf{U}) = \nabla \cdot \mathbf{U}, \tag{5}$$

*where $SD_\delta^n(\cdot; \cdot)_K$ is a local version of the stabilization form (3), and the stability weights are given by*

$$\omega_1 = C_1 h_K |\nabla \boldsymbol{\varphi}|_K,$$
$$\omega_2 = C_2 h_K |\nabla \theta|_K,$$

*where $h_K$ is the diameter of element $K$ in the mesh $\mathscr{T}_i$, and $C_{1,2}$ represent interpolation constants. Moreover, $|w|_K \equiv (\|w_1\|_K, \|w_2\|_K, \|w_3\|_K)$, with $\|w\|_K = (w, w)_K^{1/2}$, and the dot denotes the scalar product in $\mathbb{R}^3$.*

For simplicity, it is here assumed that the time derivatives of the dual variables $\hat{\varphi} = (\boldsymbol{\varphi}, \theta)$ can be bounded by their spatial derivatives. Given Theorem 1, we can understand the adaptive algorithm. As already mentioned, the error indicator, $\mathscr{E}_K$, is a function of the residual of the NSE and the solution of a linearized dual problem (a detailed formulation of the dual problem is given in Chap. 14 in [8]). Thus, on a given mesh, we must first solve the NSE to compute the residuals, $R_1(\mathbf{U}, P)$ and $R_2(\mathbf{U})$, and then a linearized dual problem to compute the weights multiplying the residuals, $\omega_1$ and $\omega_2$. With that information, we are able to compute $\sum_{K \in \mathscr{T}_i} \mathscr{E}_K$ and check it against the given stop criterion. This procedure of solving the forward and backward problems for the NSE is closely related to an optimization loop and can be understood as the problem of finding the "optimal mesh" for a given geometry and boundary conditions, i.e., the mesh with the least possible number of degrees of freedom for computing $M(\hat{\mathbf{u}})$ within a given degree of accuracy.

## 2.4 The Do-Nothing Error Estimate and Indicator

To minimize loss of sharpness, we also investigate an approach where the weak form is used directly in a posteriori error estimates, without integration by parts to the strong form, using the Cauchy–Schwarz inequality and interpolation estimates. We

here refer to this direct form of a posteriori error representation by duality as the "do-nothing" approach.

In terms of the exact adjoint solution $\hat{\boldsymbol{\varphi}}$, the output error with respect to a weak solution $\hat{\mathbf{u}}$ can be represented as

$$|M(\hat{\mathbf{u}}) - M(\hat{\mathbf{U}})| = |(R(\hat{\mathbf{U}}), \hat{\boldsymbol{\varphi}})| = |\sum_{K \in \mathscr{T}_i} (R(\hat{\mathbf{U}}), \hat{\boldsymbol{\varphi}})_K| \tag{6}$$

This error representation involves no approximation or inequalities. We thus refer to the following error indicator based on the representation as the *do-nothing error indicator*:

$$e^K \equiv (R(\hat{\mathbf{U}}), \hat{\boldsymbol{\varphi}})_K \tag{7}$$

A computable estimate and an error indicator are again based on the computed approximation $\hat{\boldsymbol{\varphi}}_h$ of the dual solution:

$$|M(\hat{\mathbf{u}}) - M(\hat{\mathbf{U}})| \approx |(R(\hat{\mathbf{U}}), \hat{\boldsymbol{\varphi}}_h)| \tag{8}$$

$$e_h^K \equiv (R(\hat{\mathbf{U}}), \hat{\boldsymbol{\varphi}}_h)_K \tag{9}$$

where we may lose reliability of the global error estimate by the Galerkin orthogonality property, which states that $(R(\hat{\mathbf{U}}), \hat{\boldsymbol{\varphi}}_h)$ vanishes for a standard Galerkin finite element method if $\hat{\boldsymbol{\varphi}}_h$ is chosen in the same space as the test functions. Although, in the setting of a stabilized finite element method, this may not be the case, see [17].

## 2.5 Turbulent Boundary Layers

In our work on high-Reynolds-number turbulent flows [5, 9, 34], we have chosen to apply a skin-friction stress as wall-layer model. That is, we append the NSE with the following boundary conditions:

$$\mathbf{u} \cdot \mathbf{n} = 0, \tag{10}$$

$$\beta \mathbf{u} \cdot \tau_k + \mathbf{n}^T \sigma \tau_k = 0, \quad k = 1, 2, \tag{11}$$

for $(\mathbf{x}, t) \in \Gamma_{solid} \times I$, with $\mathbf{n} = \mathbf{n}(\mathbf{x})$ an outward unit normal vector, and $\tau_k = \tau_k(\mathbf{x})$ orthogonal unit tangent vectors of the solid boundary $\Gamma_{solid}$. We use matrix notation with all vectors $\mathbf{v}$ being column vectors and the corresponding row vector being denoted by $\mathbf{v}^T$.

With skin-friction boundary conditions, the rate of kinetic energy dissipation in cG(1)cG(1) has a contribution of the form

$$\sum_{k=1}^{2} \int_0^T \int_{\Gamma_{solid}} |\beta^{1/2} \bar{\mathbf{U}} \cdot \tau_k|^2 \, ds \, dt, \tag{12}$$

from the kinetic energy that is dissipated as friction in the boundary layer. For high Re, we model $Re \to \infty$ by $\beta \to 0$, so that the dissipative effect of the boundary layer vanishes with large $Re$. In particular, we have found that a small $\beta$ does not influence the solution [5]. For the present simulations, we used the approximation $\beta = 0$, which can be expected to be a good approximation for real high-lift configurations, where $Re$ is very high.

### 2.6   Numerical Tripping

The simulation setting so far is idealized in the sense that the inflow is noise-free, the surfaces have no roughness, there are no vibrations in the surface, etc. This is not a realistic setting.

In the DNS community, the effect of introducing noise was investigated in [30], and it turns out that in idealized settings different DNS methods and frameworks may get different results for the same problem, but introducing a noise term has the effect of making the results more uniform.

We explore a similar idea here, where we add a volume force term similar in nature to a white noise in a domain approximating the bounding box of the aircraft geometry. We want the noise to only slightly perturb the solution and to act as a seed for growth of perturbations in unstable mechanisms (such as stall), but we do not want the noise to dominate the solution.

To achieve this balanced effect, we scale the white-noise force term by 5% of the maximum pressure gradient $|\nabla p|$.

We investigate the effect of such numerical tripping in the results section, comparing simulations with and without the tripping. We will see that, especially for stall, this appears to have a key effect in triggering the correct physical separation.

### 2.7   The FEniCS-HPC Finite Element Computational Framework

The simulations in this article have been computed using the Unicorn solver in the FEniCS-HPC automated FEM software framework.

FEniCS-HPC [10] is an open source framework for the automated solution of PDEs on massively parallel architectures, providing automated evaluation of variational forms whose description is given in a high-level mathematical notation, duality-based adaptive error control, implicit turbulence modeling by use of stabilized FEM, and strong linear scaling up to thousands of cores [12, 13, 15, 16, 21, 22, 24].

FEniCS-HPC is a branch of the FEniCS [1, 23] framework focusing on high performance on massively parallel architectures.

Unicorn is a solver technology (models, methods, algorithms, and software) with the goal of automated high-performance simulation of realistic continuum-mechanics applications, such as drag or lift computation for fixed or flexible objects (FSI) in turbulent incompressible or compressible flow. The basis for Unicorn is Unified Continuum (UC) modeling [11] formulated in Euler (laboratory) coordinates, together with the General Galerkin (G2) adaptive stabilized finite-element discretization described earlier in this chapter.

The simulations in this chapter were run on supercomputer resources described in the Acknowledgments section, and took ca. 10 h on the finest mesh for the whole time interval, using ca. 1,000 cores.

## 3   Results

We have performed simulations with the adaptive DFS methodology using the Unicorn/FEniCS-HPC framework for the JSM "pylon on" variant of the HiLiftPW-3 benchmark for the angles 4.36°, 10.58°, 18.58°, 21.57° and 22.58°. All angles except 22.58° have rich experimental data including forces, $cp$ and oil film provided by the workshop, which we will compare against subsequently. The angle 22.58° only has force data. The angles 21.57° and 22.58° exhibit stall in the experiment, e.g., large-scale separation leading to loss-of-lift force. Capturing stall quantitatively and with the correct stall mechanism is an open problem in aerodynamics, so we therefore investigate both the angle 21.57°, which is the highest angle with detailed experimental data, as well as 22.58°.

The experiment is a semispan model at $Re = 1.93 \times 10^6$. However, "free air" computations were requested, and, to avoid possible modeling errors introduced by a symmetry plane, we model the entire aircraft. However, we choose the output quantity as drag and lift of the left side of the aircraft only, to save computational resources, where we expect the adaptive method to refine in the right half-volume only when there is a significant error contribution to the drag and lift on the left side.

The initial mesh in the adaptive method has ca. $2.5 \times 10^6$ vertices, and the mesh is then iteratively refined with 5% of the cells in every iteration until we observe mesh convergence in drag and lift, or as many times as we can afford. The finest adapted meshes in our computations presented here have between $5 \times 10^6$ and $10 \times 10^6$ vertices.

We solve the time-dependent Navier–Stokes equations (1) with a non-dimensional-unit inflow velocity over the time interval $I = [0, 10]$. For some of the cases close to stall where we observe a longer startup, we extend the time interval to $I = [0, 20]$. To compute the aerodynamic coefficients, we take the mean value in the last quarter of the time interval, e.g., [7.5, 10] or [15, 20], respectively.

We have divided this section into three parts:

1. Detailed comparison of aerodynamic forces against the experiments, including convergence of the adaptive method and analysis of stall.
2. Detailed comparison of the pressure coefficients $cp$ against the experimental data, including analysis of $cp$ in the stall regime.
3. Flow visualizations are presented, including dual quantities acting as weights in the error estimates and comparison of surface velocity against oil-film visualizations in the experiment.

## 3.1   Aerodynamic Forces

The aerodynamic force in the case of zero skin friction as we describe in Sect. 2.5 is computed as:

$$F = \frac{1}{|I|} \int_I \int_{\Gamma_a} p\mathbf{n} \, ds dt, \tag{13}$$

with $\Gamma_a$ the left half-boundary of the aircraft. The drag and lift coefficients are then $C_d = \frac{2F_x}{A}$ and $C_l = \frac{2F_y}{A}$ since we have unit inflow, where A is the reference area for the JSM aircraft model given by HiLiftPW-3.

We use the duality-based "do-nothing" adaptive method, which iteratively refines the mesh by repeatedly solving the primal and dual problem based on the a posteriori error estimate. This generates a sequence of adapted meshes, a procedure that takes the role of the classical *mesh study*.

In Fig. 2, we plot the lift coefficient, $C_l$, and drag coefficient, $C_d$, versus the angle of attack, $\alpha$, for the various meshes from the iterative adaptive method. The size of the dots indicates the iteration number in the adaptive sequence, with larger dots indicating a larger number, that is more refinement. We connect the finest meshes with lines and also plot the experimental data as lines. For the angles 18.58° and 22.58°, we compute the solution both with and without the "numerical-tripping" term described in Sect. 2.6. To assess the dependence on the angle of attack, the tripped cases are plotted in red and the adaptive sequence is shifted somewhat to the right for clarity.

We observe mesh convergence to within 1–2% for all cases, a close match to the experiments for $C_l$, within circa 5%, and a small overprediction of ca. 10% for $C_d$, which is consistent with the majority of the participants in HiLiftPW-3 across a range of methods [28], suggesting a systematic error in the problem statement or the experimental data.

For the stall regime angles 18.58°, 21.57° and 22.58°, we qualitatively reproduce the stall phenomenon in the experiment—a decrease in $C_l$ with increased angle of attack past 21.57°. We observe that the stall angle occurs somewhere between 18.58°, 21.57°, which is ca. 1° from the experimental stall angle.

Additionally, we verify that the "numerical tripping" functions as expected: the term has no significant impact on the solution for an angle of 18.58°, which is the

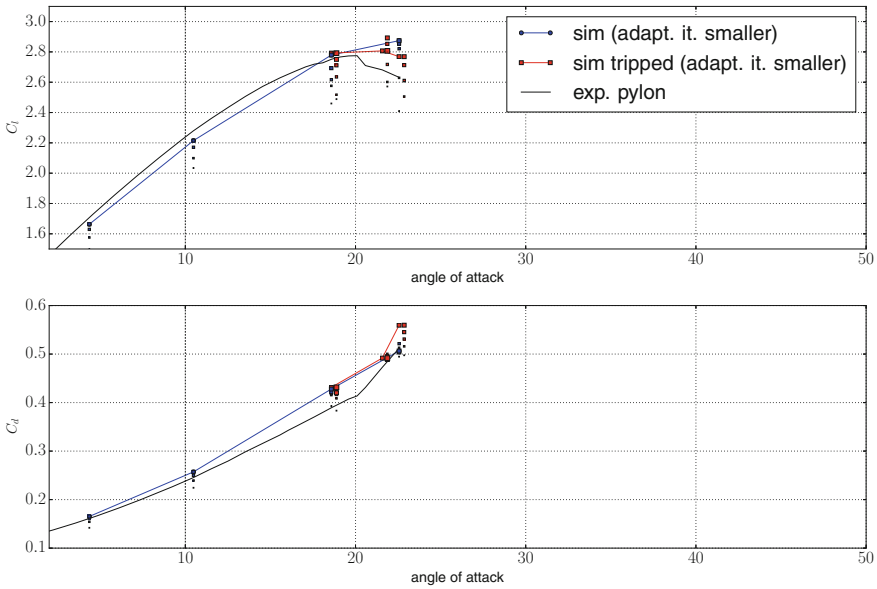HiLiftPW-3 JSM pylon-on Unicorn - $C_l$ and $C_d$ vs. angle of attack



**Fig. 2** Lift coefficient, $C_l$, and drag coefficient, $C_d$, versus the angle of attack, $\alpha$, for the different meshes from the iterative adaptive method

maximum lift angle and the maximum non-stalling angle, whereas for the stalling angle 22.58° we observe that the tripping has the effect of triggering a large-scale separation consistent with the stall phenomenon, whereas the untripped case appears to contain too small perturbations for the separation to occur. We analyze the stall mechanism in more detail in the surface velocity visualization next.

To analyze the variability in time of $C_d$ and $C_l$, we plot the time evolution for $\alpha = 4.36°$ in Fig. 3, untripped with $\alpha = 18.58°$ in Fig. 4 and tripped with $\alpha = 18.58°$ in Fig. 5.

For the pre-stall cases we observe an initial "startup phase" for $t \in [0, 5]$ and then an oscillation around a stable mean value. The effect of the numerical tripping is noise in the $C_d$ and $C_l$ signals with amplitude of about 1% (Fig. 5).

## 3.2 Pressure Coefficients

The pressure coefficients $C_p$ from both simulation on the finest adaptive mesh and experiments are plotted in Figs. 7, 8 and 9, for the wing, flap, and slat, respectively.

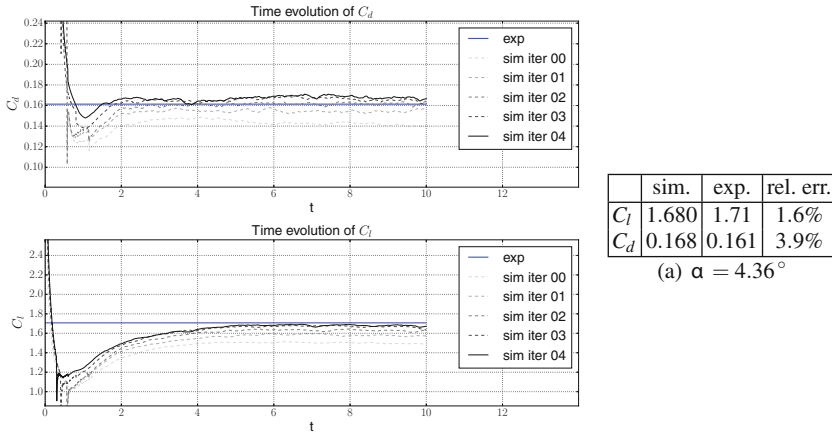The pressure-sensor locations corresponding to the plots are specified in the diagram in Fig. 6.

**Fig. 3** Time evolution of lift coefficient, $C_l$, and drag coefficient, $C_d$, and a table of the value for the finest adaptive mesh with relative error compared to the experimental results for $\alpha = 4.36°$
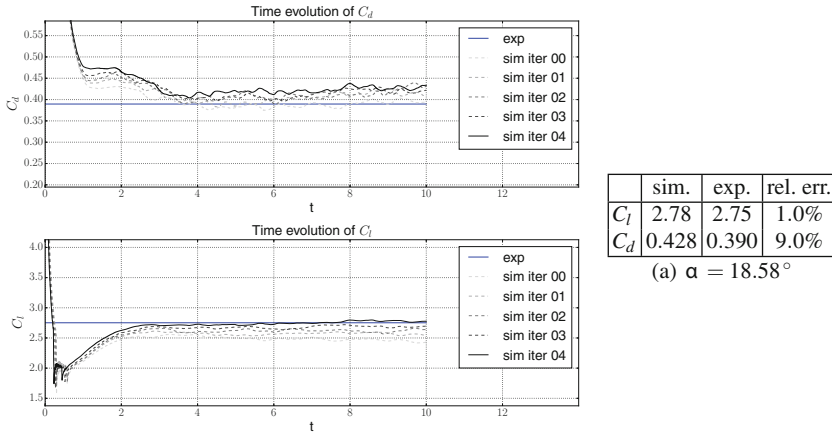


**Fig. 4** Time evolution of lift coefficient, $C_l$, and drag coefficient, $C_d$, and a table of the value for the finest adaptive mesh with relative error compared to the experimental results for $\alpha = 18.58°$, untripped

Since the aerodynamic force defined in (13) matches the experiment well, and since it consists of integrals of the pressure weighed by the normal vector, the $C_p$ values also have to match the experiment on average. However, the $C_p$ plots can give insight into local mechanisms such as separation patterns, an important example being the stall mechanism. These local mechanisms are what we will focus on here.

First of all, we see that for the pre-stall angles $\alpha = 10.48°$ and $\alpha = 18.58°$ the simulation and experiment match very well for the wing and slat, and generally well for the flap, aside from local differences. The $C_p$ for the simulation is lower on the
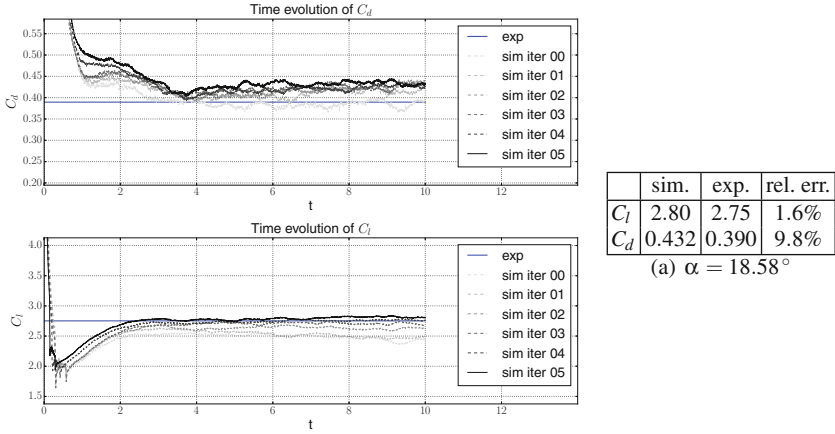
**Fig. 5** Time evolution of lift coefficient, $C_l$, and drag coefficient, $C_d$, and a table of the value for the finest adaptive mesh with relative error compared to the experimental for $\alpha = 18.58°$ with numerical tripping
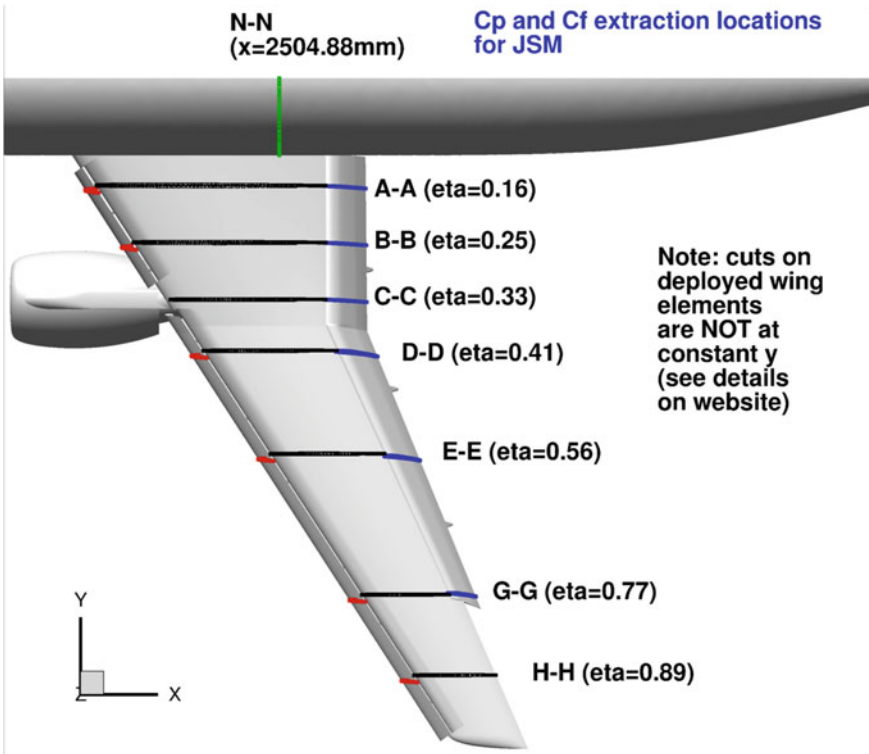


**Fig. 6** Diagram of the pressure-sensor layout for the JSM configuration showing where the pressure sensors are located and how they are denoted
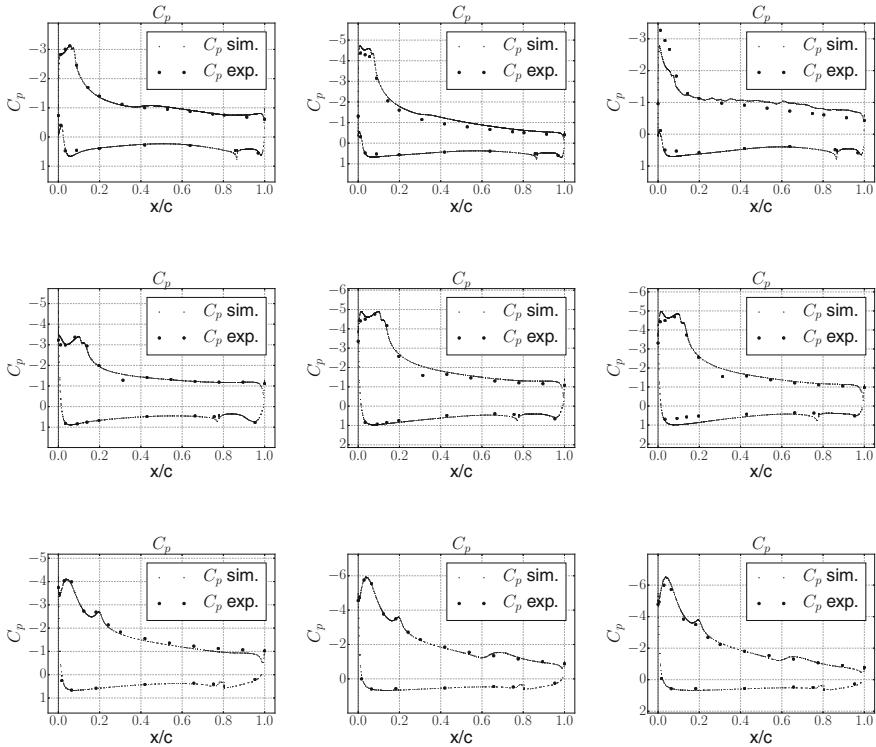
**Fig. 7** Pressure coefficients, $C_p$, versus normalized local chord, $x/c$, for the angles of attack $\alpha = 10.48°$ (left), $\alpha = 18.58°$ (middle) and $\alpha = 22.56°$ (right) at locations A-A (top), D-D (middle) and G-G (bottom) for the wing of JSM pylon on

upper surface for the flap close to the body (the A-A station). Otherwise the curves generally match.

For the stall regime, we analyze both 21.57° where experimental $C_p$ are available and 22.56° where experimental $C_p$ plots are not available. We compare both against the experimental $C_p$ plots for 21.57° to have a margin if we have stall at a higher angle in the simulation. The simulation matches the experiment very well: there is a small discrepancy for the wing close to the body (the A-A station), but considering that this is where the large-scale separation causing the stall is located, the results match acceptably.

The matching $C_p$ curves are consistent with matching $C_d$ and $C_l$ from the aerodynamic force plots.

We now compare the tripped and untripped simulation with the experiment at 22.56°, as well as 22.56° in Fig. 10 for the wing. We clearly see that the untripped simulation for 22.56° grossly misses the $C_p$ on the upper surface at station A– A, near the wing-body junction where the large-scale separation mechanism causing stall is located, while the tripped simulation captures the experimental $C_p$ curve well, aside
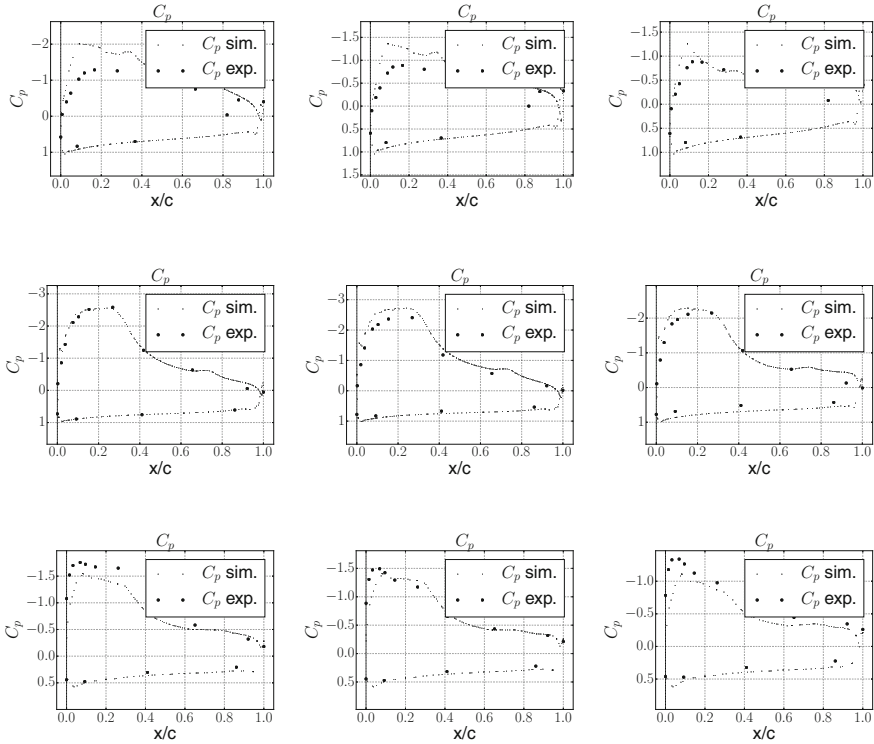
**Fig. 8** Pressure coefficients, $C_p$, versus normalized local chord, $x/c$, for the angles of attack $\alpha = 10.48°$ (left), $\alpha = 18.58°$ (middle) and $\alpha = 22.56°$ (right) at locations A-A (top), D-D (middle) and G-G (bottom) for the flap of JSM pylon on

from a slightly lower $C_p$ near the leading edge. We conclude that the tripping acts to trigger the physically correct separation. At the other stations, D–D and G–G, the tripped and untripped simulations are very similar, indicating that the tripping does not have a significant effect aside from the triggering of the perturbations.

The $\alpha = 21.57°$ simulation is tripped and captures the experiment less well than $22.56°$, but better than $22.56°$ untripped indicating that we may have a ca. 1° later stall angle in the simulation than in the experiment.

### 3.3 Flow and Adaptive Mesh Refinement Visualization

Here we concentrate on presenting effective visualization of the flow and the adaptive mesh refinement procedure. Our aim is to provide information on the properties and features of the approximated solution and, more importantly, of the approximating procedure, most of which cannot be discerned from one-dimensional plots of the
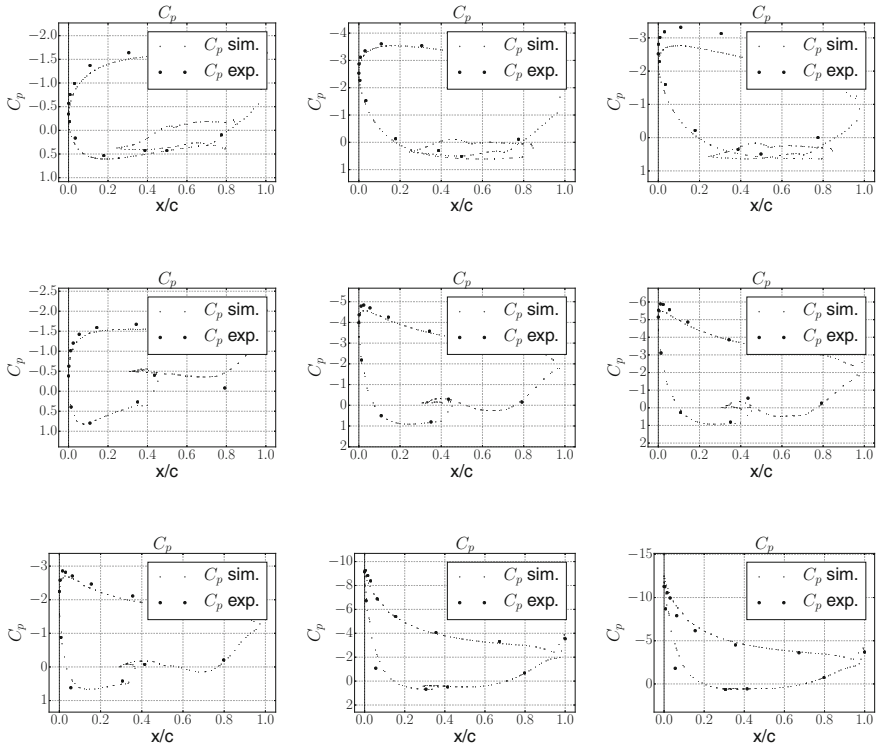
**Fig. 9** Pressure coefficients, $C_p$, versus normalized local chord, $x/c$, in the stall regime for the angles of attack $\alpha = 10.48°$ (left), $\alpha = 18.58°$ (middle) and $\alpha = 22.56°$ (right) at locations A-A (top), D-D (middle) and G-G (bottom) for the slat of JSM pylon on

pressure coefficient and the aerodynamic forces. Sometimes, these more complex visualizations cannot be directly compared to experiments, but still they constitute a qualitative validation of the results.

The first plots that we show are the surface plots of the velocity magnitude on the upper side of the wing. Together with the velocity magnitude surface plots, we also supply pictures of the oil-film experiment that was provided by the organizers as a validation. These serve as comparison, and we report such comparison in Fig. 11.

Some common features intrinsic of the geometry of the JSM aircraft are revealed by the oil-film experiment and reproduced by the velocity plots. A pattern of low velocity streaks, alternating with areas of higher velocity, is seen on the suction side of the fixed wing for all angles of attack. This is caused by separation at the slat tracks upstream, which is correctly captured by the numerical solution.

Another characteristic feature of the flow is the turbulent separation near the tip of the wing. This is particularly evident in the case $\alpha = 18.59°$.

Areas that exhibit this kind of flow behavior influence the aerodynamic forces on the aircraft, and, indeed in our experimentation, we found that computations
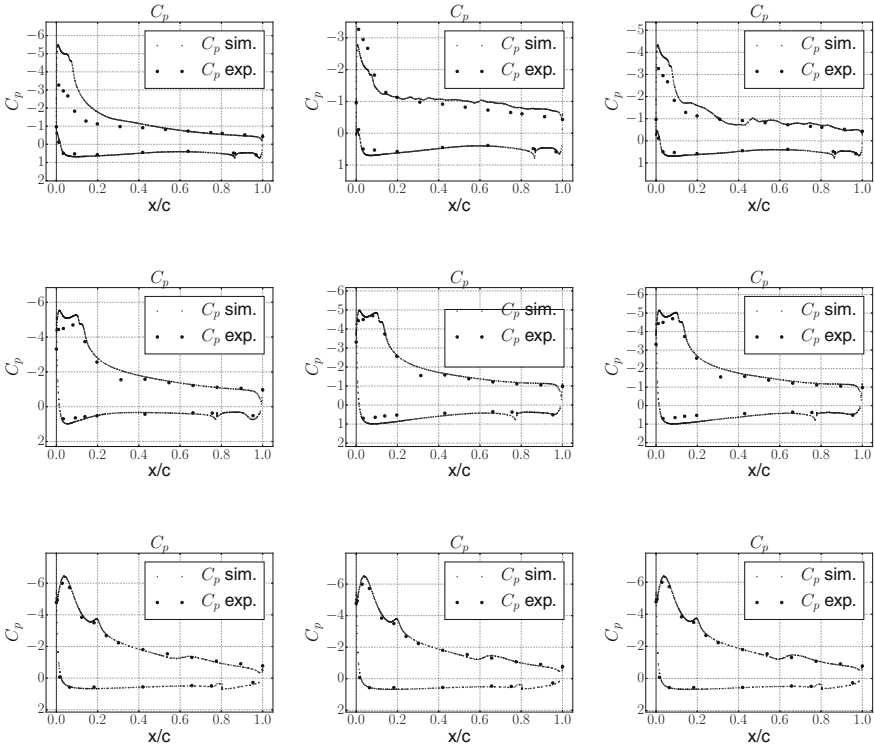
**Fig. 10** Pressure coefficients, $C_p$, versus normalized local chord, $x/c$, for the angle of attack $\alpha = 22.56°$ untripped (left), the same angle $\alpha = 22.56°$ tripped (middle) and $\alpha = 21.57°$ tripped at locations A-A (top), D-D (middle) and G-G (bottom) for the wing of JSM pylon on

done on some meshes resulted in wrong predictions of the target functionals, usually yielding lower lift coefficients than the experimental ones. We were able to overcome this intermediate obstacle by refining the surface mesh were the original geometry had a higher curvature. We later interpreted the effectiveness of this workaround as a symptom that the original meshes were unable to capture the surface geometry to a sufficient degree of accuracy, and were for this reason failing at reproducing these complex patterns.

Another interesting visualization technique, which we are about to present, is more closely related to turbulence itself: the Q-criterion [20]. The Q-criterion was widely used in the literature to visualize the turbulent features of fluid flows. The main idea is that it is possible to define a quantity, commonly denoted by the letter $Q$, whose value is related to the vorticity, and thus the visualization of the isocontours of $Q$ is claimed to give visual information on the presence and location of vortexes within the flow field.

The Q-criterion for the case of the airplane with pylon is displayed in Fig. 12 for three different angles of attack.

(a) $\alpha = 10.48°$            (b) $\alpha = 10.48°$

(c) $\alpha = 18.59°$            (d) $\alpha = 18.59°$

(e) $\alpha = 21.57°$            (f) $\alpha = 22.56°$
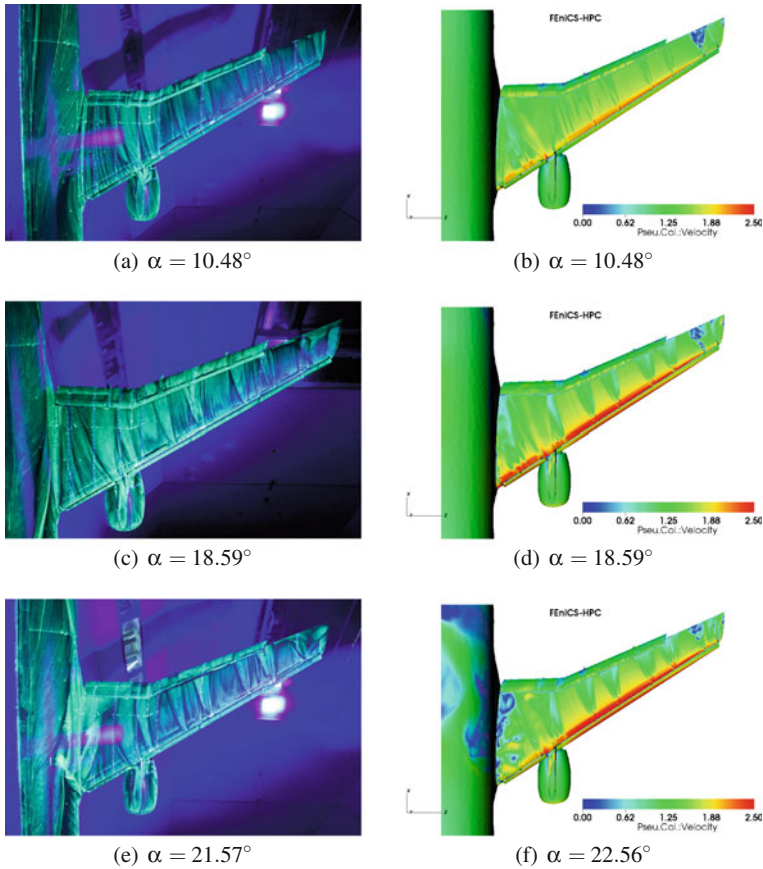
**Fig. 11** Comparison between experimental oil film visualization (left) and surface rendering of the velocity magnitude (right)

Once again, the visualization technique highlights the same pattern as in the previous case: the isosurfaces assume a characteristic V shape along the interfaces between the fast and slow velocity regions on the suction side of the wing. Not only that, but we can also clearly distinguish a clustering of these isosurfaces near the tip of the wing, matching the position of the turbulent separation zone that we mentioned previously. The Q-criterion visualizations are consistent with the surface velocity plots, and this internal coherence increases our trust in the computational results.

Let us now turn our attention to the adaptive procedure which produces the successive approximations of the fluid flow. As we described already, the mesh-refinement solution is driven by the residual of the Navier–Stokes equations and the solution of the dual Navier–Stokes equations. We begin by showing a plot of a volume rendering of the dual solution, see Fig. 13.
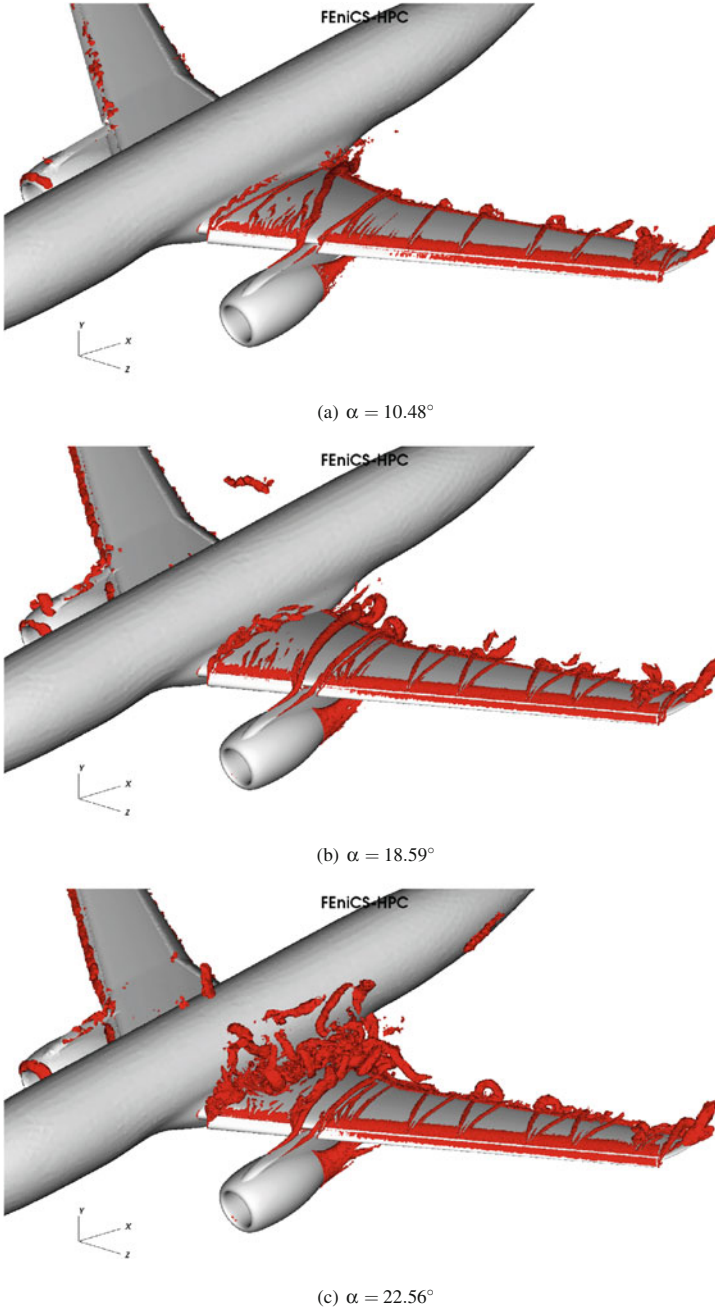
(a) $\alpha = 10.48°$


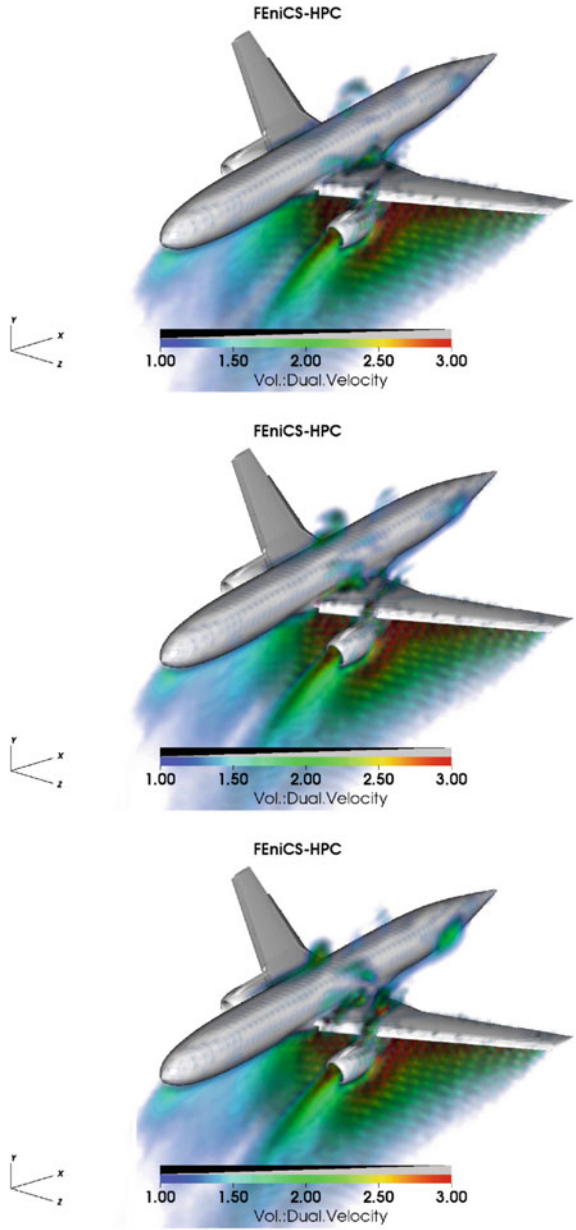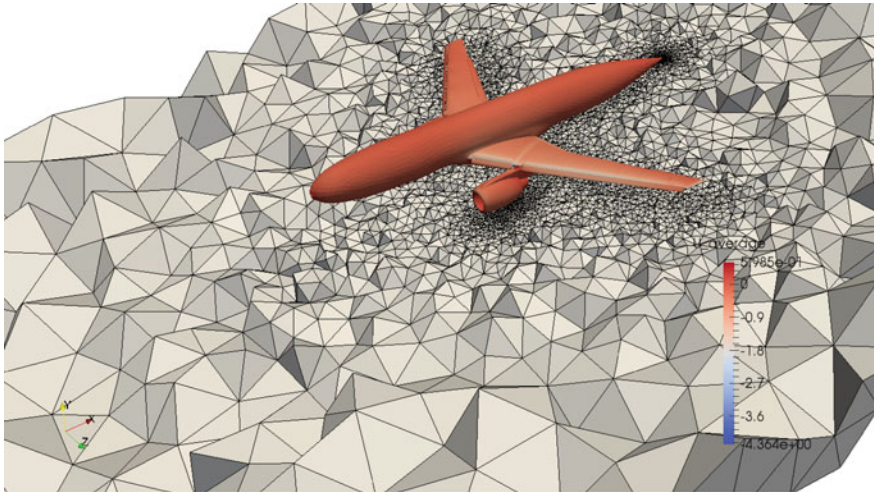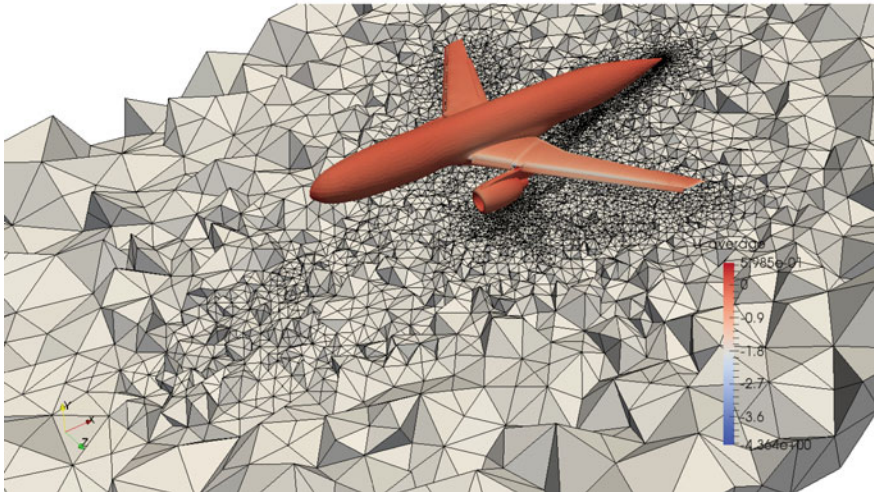
(b) $\alpha = 18.59°$



(c) $\alpha = 22.56°$

**Fig. 12**  Instantaneous isosurface rendering at the final time of the Q-criterion with value $Q = 100$

**Fig. 13** Volume rendering
of the time evolution of the
magnitude of the adjoint
velocity $\varphi$ magnitude,
snapshots at t = (16, 18, 20),
$\alpha = 22.58$

(a) Starting mesh



(b) Finest adaptive mesh

**Fig. 14** Crinkled slice aligned with the angle of attack, $\alpha = 10.48°$

What is worth noting here is that the adjoint velocity flows backwards in time and, consequently, it appears to be flowing in the opposite direction of the primal velocity. We observe that the part of the mesh where the dual velocity has higher values is *upstream* to the airplane. Because of the way the do-nothing error estimator is designed, we expect that the refinement will happen where both the residual and the dual solution are large. Indeed, this has the important implication that the mesh refinement will not only happen on the wing, where the forces are computed, but

also upstream, splitting cells that, a priori, are unrelated to the computation of the aerodynamic forces.

This feature is unique for our methodology: while other methods tend to refine the mesh in zones where *intuitively* higher accuracy would yield better approximation of the aerodynamic forces, namely around the body and downstream, the adaptive algorithm provides an automatic procedure that knows nothing about the features of the flow but only takes into account the residual of the equations of motion and the solution of the dual problem.

In our numerical experimentation we found that this is exactly what happens, as we are about to show. Consider Fig. 14, showing a crinkled slice of the mesh for the initial and the finest meshes for a given angle of attack. It is clear that the mesh refinement procedure is concentrating both on the area around the surface where the aerodynamic forces are computed and in the upstream region. Some cells are refined downstream due to the large residual.

## 4    Conclusions

This chapter presents an adaptive finite element method without turbulence model parameters for time-dependent aerodynamics, and we validate the method by simulation results of a full aircraft model originating from the 3rd AIAA CFD High-Lift Prediction Workshop (HiLiftPW-3), which was held in Denver, Colorado, on June 3–4 2017. The mesh is automatically constructed by the method as part of the computation through duality-based a posterori error control and no explicit turbulence model is used. Dissipation of turbulent kinetic energy in under-resolved parts of the flow is provided by the numerical stabilization in the form of a weighted least squares method based on the residual of the NSE. Thus, the method is purely based on the NSE mathematical model, and no other modeling assumptions are made.

The DFS method and these simulations are thus *parameter-free*, where no a priori knowledge of the flow is needed during the problem formulation stage, nor during the mesh-generation process. Additionally, the computational cost is drastically reduced by modeling turbulent boundary layers in the form of a slip boundary condition, and thus no boundary-layer mesh is needed.

The computed aerodynamic coefficients are very close to the experimental values for all the angles of attack that we studied. In particular, $C_l$ is within circa 5% of the experiments, $C_d$ has a small overprediction of circa 10%, which is consistent with the majority of the participants in HiLiftPW-3 across a range of methods [28], suggesting a systematic error in the problem statement or the experimental data.

The fact that the error is automatically estimated by the method is itself a critical feature missing in most (if not all) other computational frameworks for CFD.

Moreover, the adaptive procedure in DFS is seen to converge to a mean value with oscillations on the order of 1–2%. This contributes to increase confidence in the numerical method.

The point of adaptive computations is all about saving on the computational cost. During the workshop we had the chance to compare our performance with that of the other participating groups. In terms of number of degrees of freedom, DFS is about ten times cheaper than the leading RANS and Lattice Boltzmann Methods.

To capture stall, we applied a tripping-noise term that turned out to have the effect of triggering the physically correct stall-separation pattern. A similar idea with a noise term is employed in the DNS community, and the addition of this term seems to have no effect on non-stalling configurations, which is an important validation.

We observed that DFS was able to capture the stall mechanism of the proposed configuration, namely the large-scale separation pattern that occurs at the wing-body juncture. The same mechanism is observed in the experiments. The stall angle is also captured within ca. $1°$.

# References

1. FEniCS (2003) Fenics project. http://www.fenicsproject.org
2. Hoffman, J.: Computation of mean drag for bluff body problems using adaptive dns/les. SIAM J. Sci. Comput. **27**(1), 184–207 (2005)
3. Hoffman, J.: Adaptive simulation of the turbulent flow past a sphere. J. Fluid Mech. **568**, 77–88 (2006)
4. Hoffman, J.: Efficient computation of mean drag for the subcritical flow past a circular cylinder using general galerkin g2. Int. J. Numer. Meth. Fluids **59**(11), 1241–1258 (2009)
5. Hoffman, J., Jansson, N. (2010) A computational study of turbulent flow separation for a circular cylinder using skin friction boundary conditions. Ercoftac series, vol. 16. Springer, Dordrecht
6. Hoffman, J., Johnson, C.: Computational Turbulent Incompressible Flow: Applied Mathematics Body and Soul, vol. 4. Springer, Berlin (2006)
7. Hoffman, J., Johnson, C.: A new approach to computational turbulence modeling. Comput. Methods Appl. Mech. Eng. **195**, 2865–2880 (2006)
8. Hoffman, J., Johnson, C.: Computational turbulent incompressible flow. In: Applied Mathematics: Body and Soul, vol. 4. Springer, Berlin (2007)
9. Hoffman, J., Johnson, C.: Resolution of d'alembert's paradox. J. Math. Fluid Mech., 10 Dec 2008. (Published Online First at www.springerlink.com)
10. Hoffman, J., Jansson, J., Jansson, N.: Fenics-hpc: automated predictive high-performance finite element computing with applications in aerodynamics. In: Proceedings of the 11th International Conference on Parallel Processing and Applied Mathematics, PPAM 2015. Lecture Notes in Computer Science (2015)
11. Hoffman, J., Jansson, J., Stöckli, M.: Unified continuum modeling of fluid-structure interaction. Math. Models Methods Appl. Sci. (2011)

12. Hoffman, J., Jansson, J., de Abreu, R.V., Degirmenci, N.C., Jansson, N., Müller, K., Nazarov, M., Spühler, J.H.: Unicorn: parallel adaptive finite element simulation of turbulent flow and fluid-structure interaction for deforming domains and complex geometry. Comput. Fluids **80**, 310–319 (2013)

13. Hoffman, J., Jansson, J., Degirmenci, C., Jansson, N., Nazarov, M.: Unicorn: A Unified Continuum Mechanics Solver, Chap. 18. Springer, Berlin (2012)

14. Hoffman, J., Jansson, J., Jansson, N., Abreu, R.V.D.: Towards a parameter-free method for high reynolds number turbulent flow simulation based on adaptive finite element approximation. Comput. Methods Appl. Mech. Eng. **288**, 60–74 (2015)

15. Hoffman, J., Jansson, J., Jansson, N., Nazarov, M.: Unicorn: a unified continuum mechanics solver. In: Automated Solutions of Differential Equations by the Finite Element Method. Springer, Berlin (2011)

16. Hoffman, J., Jansson, J., Jansson, N., Johnson, C., de Abreu, R.V.: Turbulent flow and fluid-structure interaction. In: Automated Solutions of Differential Equations by the Finite Element Method. Springer, Berlin (2011)

17. Hoffman, J., Jansson, J., Jansson, N., De Abreu, R.V., Johnson, C.: Computability and adaptivity in CFD. In: Stein, E., de Horz, R., Hughes, T.J.R. (eds.) Encyclopedia of Computational Mechanics (2016)

18. Houzeaux, G., Vázquez, M., Aubry, R., Cela, J.: A massively parallel fractional step solver for incompressible flows. J. Comput. Phys. **228**(17), 6316–6332 (2009)

19. Huang, L., Huang, P.G., LeBeau, R.P.: Numerical study of blowing and suction control mechanism on naca 0012 airfoil. AIAA J. Aircr. (2004)

20. Hunt, J.C., Wray, A.A., Moin, P.: Eddies, streams, and convergence zones in turbulent flows (1988)

21. Jansson, N., Hoffman, J., Jansson, J.: Framework for massively parallel adaptive finite element computational fluid dynamics on tetrahedral meshes. SIAM J. Sci. Comput. **34**(1), C24–C41 (2012)

22. Kirby, R.C.: FIAT: Numerical Construction of Finite Element Basis Functions, Chap. 13. Springer, Berlin (2012)

23. Logg, A., Mardal, K.-A., Wells, G.N., et al.: Automated Solution of Differential Equations by the Finite Element Method. Springer, Berlin (2012)

24. Logg, A., Ølgaard, K.B., Rognes, M.E., Wells, G.N.: FFC: The FEniCS Form Compiler, Chap. 11. Springer, Berlin (2012)

25. Mellen, C.P., Frölich, J., Rodi, W.: Lessons from lesfoil project on large-eddy simulation of flow around an airfoil. AIAA J. **41**, 573–581 (2003)

26. Moin, P., You, D.: Active control of flow separation over an airfoil using synthetic jets. J. Fluids Struct. **24**(8), 1349–1357 (2008)

27. Piomelli, U., Balaras, E.: Wall-layer models for large-eddy simulation. Annu. Rev. Fluid Mech. **34**, 349–374 (2002)

28. Rumsey, C.: 3rd AIAA CFD High Lift Prediction Workshop (HiLiftPW-2) (2017). http://hiliftpw.larc.nasa.gov/

29. Sagaut, P.: Large Eddy Simulation for Incompressible Flows, 3rd edn. Springer, Berlin (2005)

30. Schlatter, P., Orlu, R.: Turbulent boundary layers at moderate reynolds numbers: inflow length and tripping effects. J. Fluid Mech. **710**, 534 (2012)

31. Shan, H., Jiang, L., Liu, C.: Direct numerical simulation of flow separation around a naca 0012 airfoil. Comput. Fluids **34**, 10961114 (2005)

32. Slotnick, J., Khodadoust, A., Alonso, J., Darmofal, D., Gropp, W., Lurie, E., Mavriplis, D.: Cfd vision 2030 study: a path to revolutionary computational aerosciences (2014)

33. Spalart, P.R.: Detached-eddy simulation. Annu Rev. Fluid Mech. **41**, 181–202 (2009)

34. Vilela de Abreu, R., Jansson, N., Hoffman, J.: Adaptive computation of aeroacoustic sources for a rudimentary landing gear. Int. J. Numer. Meth. Fluids **74**(6), 406–421 (2014)

35. Witherden, F.D., Jameson, A.: Future directions of computational fluid dynamics. In: 23rd AIAA Computational Fluid Dynamics Conference, p. 3791 (2017)

# RANS Simulations of the High Lift Common Research Model with Open-Source Code SU2

**A. Matiz-Chicacausa, J. Escobar, D. Velasco, N. Rojas and C. Sedano**

**Abstract** High-lift devices have been used in aviation for several decades as an effective solution to keep takeoff and landing speeds within an acceptable range, while increasing wing loading for faster and more efficient cruising. Accurate prediction of performance of such devices is essential not only for design requirements but also for providing reliable operational speeds to crews and automatic flight systems. In this regard, the chapter presents numerical solutions and analysis of the flow around the so-called High Lift Common Research Model (HL-CRM) as a contribution to the Third High Lift Prediction Workshop. Stanford's University CFD code SU2 was used to compute a set of solutions on two grids of the family B3 provided by the organizing committee, at 8° and 16° of angle of attack, and Reynolds number of $3.26 \times 10^6$. Results showed good agreement in aerodynamic coefficients when compared to solutions submitted by participants of the workshop. The main features of the flow over the lifting surfaces and in the wake of the wing were also observed and discussed based on theory and results published by other authors.

A. Matiz-Chicacausa (✉) · J. Escobar
Universidad de San Buenaventura, Cra 8H No 172-20, Bogotá, Colombia
e-mail: amatiz@usbbog.edu.co

J. Escobar
e-mail: jescobar@usbbog.edu.co

D. Velasco · N. Rojas · C. Sedano
Universidad de Los Andes, Cra 1 Este No 18A-12, Bogotá, Colombia
e-mail: ds.velasco2170@uniandes.edu.co

N. Rojas
e-mail: n.rojas452@uniandes.edu.co

C. Sedano
e-mail: ca.sedano1167@uniandes.edu.co

# 1 Introduction

Nowadays, Computational Fluid Dynamics (CFD) codes are a reliable and consistent tool to predict aerodynamic behavior for simplified aircraft configurations. However, high-lift aerodynamics analysis is still a challenging aspect. Complexities in high-lift flows include wakes in pressure gradients, wake/boundary-layer merging, streamline curvature, separated flow, wingtip vortical flow, and laminar/turbulent transition regions on wing elements [1]. Therefore, a series of workshops to advance the state of the art in predicting high-lift flows through CFD simulations was established.

The first HiLiftPW in 2010 focused on the three-element NASA Trapezoidal Wing Configuration. Interesting results were presented as, for example, that CFD tended to underpredict lift, drag, and the magnitude of the pitching moment compared with experimental measurements, also a significant spread of solutions near stall and difficulties in predicting flow near the wingtip [1]. Hence, a second version of the workshop was planned to overcome previous issues, like grid-convergence studies. The DLR-F11 three-element wing/body was chosen as a reference for the second workshop. This configuration was more representative than the previous one, and experimental data for low and high Reynolds number were available to validate CFD computations [2]. In the frame of the third High Lift Prediction Workshop held in Denver, after successful previous editions, the Common Research Model (CRM) developed by Lacy and Scalafani [3] aimed to simulate, at two angles of attack (8° and 16°) and two configurations: (i) full-chord flap gap and (ii) partially-sealed chord-flap gap. The goals of the workshop were to assess the numerical prediction capabilities of current CFD codes for high-lift configurations, to develop guidelines for CFD prediction of high-lift flow fields, to determine the critical parameters of high-lift physics to enable the development of accurate prediction methods, and to enhance CFD prediction capabilities for high-lift aerodynamics. For the third workshop, blind computations of the CRM were performed by around 40 participants with various CFD codes.

High-lift systems owe their importance to the fact that they enable commercial airplanes to efficiently perform low-speed operations, which further affects takeoff and landing stages, for instance. The study of these systems enabling us to measure the impact of relatively small changes in the aerodynamic behavior leads to important payoffs in aircraft weight and performance [4]; some examples are presented by Meredith [5].

The particularity of the field flow on high-lift systems is the interaction and eventual merging of each upstream element's wake with the boundary layer of the elements downstream. This flowfield is characterized by a thin, turbulent boundary layer that produces stronger gradients of pressure, hence it is less likely to experience flow separation.

The flow circulation over the forward element (i.e., slat) induces a velocity component opposed to the natural direction of the flow over the trailing edge of the downstream element (i.e., main wing); this so-called *slat effect*, decreases the suction peak over the leading edge of the downstream element, so that pressure recovery is

reduced and flow detachment is delayed. At the same time, the back element induces a circulation effect on the upstream element that tends to increase its loads; therefore, lift increases. The accelerated flow over the upper surface of the downstream element alleviates the pressure recovery, which is also beneficial for the boundary layer, and the flow is discharged at a higher velocity at the trailing edge of the slat. This is known as the dumping effect [6].

Numerical simulations are well established in the aerospace industry as a tool to predict aerodynamic behavior, design airplanes components, and study fluid-structure interaction, among others. In the past, CFD was mainly used for aerodynamic-cruise design but in recent years it has been employed for many types of aerodynamic studies, among which, low-speed design is still one of the more challenging. Low-speed design includes studies of the shape of fixed wings or flap-leading edges and configurations of slats-flaps wing. Additionally, it deals with multi-functional use of high-lift components and, the simplification of high-lift systems. From the physical point of view, flow separation and reattachment, laminar-turbulent transition, viscous wakes interaction, and confluent boundary layers are complex phenomena, which are difficult to model [7] and hence to simulate by CFD; furthermore, geometric complexities amplify disagreement between wind tunnel data and CFD simulations results [8].

CFD simulations of high-lift systems have been an interesting topic among researchers for the past decade. To reduce the difficulties of simulating complex geometries with structured grids, various grid-adaption techniques have been used, with the multizonal approach and chimera grids some of the most common. Mathias and Cummins employed both techniques, chimera and multi-block patched grids, to capture the complexities of the flow associated with two- and three-dimensional, multi-element, high-lift systems and to validate results from CFL3D with experimental data [9]. NASA's high-lift trapezoidal wing has been widely studied due to the extensive set of experimental data available; among other authors [10], the main goal was to validate CFD code OVERLOW, while the solver captured the viscous behavior over high-lift configurations. Karea et al. [7] aimed to find the adequate resolution for the grid to capture the complex viscous phenomena and to accurately predict aerodynamic coefficients, while Chaffin and Pizadeh [11] focused on grid-refinement requirements to model flow physics, correctly predict aerodynamic coefficients, and study the effect of slat and flap brackets.

Considering the CFD approach to accurately predict flow behavior over high-lift systems, there are many possible sources of inconsistency that still are issue of study currently. First is the error associated with grids lacking good resolution. Reynolds-Averaged Navier Stokes (RANS) simulations capture the flow field up to large-scales of turbulent structures; however, it might be that the zones depending on the grid resolution do not capture well these structures, and hence they underestimate aerodynamic coefficients. Another issue of interest is the turbulence model, since there is a large range of models from which to choose and significant disagreement exist among their results [12]. The RANS method lacks physical accuracy and cannot completely describe the turbulent flow field; additionally, the unsteady nature of the flow must be properly simulated by solving time-dependent equations.

The concern of developing better quality grids and adaptive grid techniques to improve physical modeling and to capture the complexities associated with flow performance and geometries is still an issue of discussion. One of the main conclusions of the last High Lift Prediction Workshop was the apparent need for extra-fine grids (around 200–600-million grid points) to reduce scatter among the participant's results since predicting flow near $C_{L,max}$ is still challenging, and flow separation appears to not be properly modeled [13].

This chapter presents the participation of Universidad de San Buenaventura and Universidad de Los Andes to the most recent High Lift Prediction Workshop using the Stanford University Unstructured (SU2) CFD open-source code [14]. The development of open-source codes has accelerated the last decade, but they have not been fully validated. Moreover, the representation of this kind of code on the HiLiftPW is reduced to OpenFOAM, participation by Oxford University in the last two workshops and the Colombian participation with SU2 in the third version. SU2 has grown rapidly since its release. The focus on solving aerodynamic problems and satisfactory results has led to an increasing acceptance of SU2 [14, 15]. The goals of this work were to test low computational capabilities with world-class problems and to assess open-source code's capabilities to predict aerodynamic forces/moments with complex geometries.

## 2  NASA's Common Research Model

For the third High Lift Prediction workshop, the High Lift Common Research Model (HL-CRM) designed by NASA engineers [3] was used as a reference geometry with a full-chord flap-gap configuration. This is a wing-body high-lift system studied in a nominal landing configuration (slats and flaps deployed at 30° and 37°, respectively) without nacelle, pylons, and tail or support brackets. In the present work, an aerody-
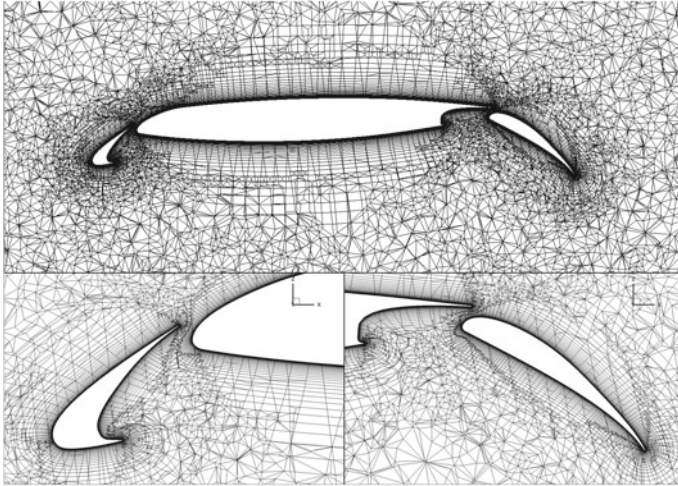


**Fig. 1** Coarse mesh over NASA's CRM
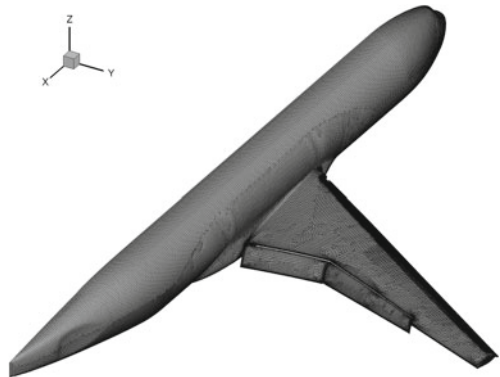
**Fig. 2** Coarse mesh around a wing section. Lower right: slat; lower left: flap

namic study was performed for the HL-CRM at $M = 0.2$ and $Re = 3.26 \times 10^6$ at angles of attack $\alpha = 8°$ and $\alpha = 16°$.

Simulations were performed on two grids of different levels of refinement with the full-chord flap-gap configuration. Figure 1 depicts NASA's CRM with the coarse mesh. Figure 2 shows a sectional view of the coarse mesh around the wing and a detailed view of the mesh over the flap and slat.

## 3 Numerical Methods

This section describes the software employed for all simulations in this work (Stanford University Unstructured SU2), the computational configuration of the cases to achieve convergence, and the turbulence model.

### 3.1 Stanford University Unstructured (SU2)

SU2 is an unstructured, node-based solver; the numerical scheme is based on the finite-volume method to discretize the governing equations (full compressible solver) with a standard edge-based structure on a dual grid with control volumes constructed using a median-dual, vertex-based scheme [16].

Regarding discretization of the governing equations, the Green-Gauss Method for the gradient terms was used at all grid nodes and then averaged to obtain the flow values at the cell faces. Due to the nature of the solver, the convective and viscous

fluxes are evaluated at the midpoint of an edge, and then the solver integrates the values over the edges. The convective fluxes were discretized using a second-order of accuracy in space with a gradient limitation (MUSCL) and numerical method ROE [17].

Time discretization was achieved with the first-order implicit Eulers scheme. The Courant-levy number for the local time step was set to be adaptive between a value range of a maximum of ten and a minimum of one. To improve the convergence rate, the lower-upper symmetric Gauss-Seidel preconditioner (LU-SGS) was used, and a Roe-Turkel preconditioner for low Mach flow [18] was employed.

Numerical simulations performed on both coarse and medium grids started fresh at 8° angle of attack with first order discretization of the convective fluxes for the first iterations to assure convergence and then modified to second order to improve convergence. Furthermore, two levels of multigrid were used on the coarse grid to accelerate convergence and changed to one level before the solution suddenly started to diverge. Numerical simulations at 16° angle of attack were computed from the solution obtained at 8° angle of attack. Residuals for all the transport variables decreased at least six orders of magnitude.

### 3.2   Turbulence Modelling

Turbulence modeling is a key aspect of CFD simulations. Currently, this can be achieved by four approaches: Reynolds-Averaged Navier-Stokes (RANS) which requires the least computational resources; direct numerical simulations (DNS); large eddy simulations (LES) that requires high computational resources; and hybrid methods that combine RANS and LES (e.g., DES). Currently, RANS models are the most often used among aerodynamic applications due to their good compromise between accurate results and their requirements for computational resources. This study used the Standard Spalart-Allmaras RANS model [19] which is heavily used in aerodynamic applications and simulations of external flows.

### 3.3   Computational Resources

Three high-performance computing systems were used to run all the numerical simulations presented in this chapter. First, a Dell Precision R5500 running Rocks 6.2., with Dual Intel Xeon X5675, 3.06 GHz, 12-M Cache, 6.40 GT/s Intel QPI, and 96 GB DDR3 ECC RDIMM was used to compute solutions on the coarse grid for both 8° and 16° angles of attack. Second, the simulation on the medium grid at angle of attack of 8° was run in a 17-HP blade serverss ProLiant BL460c Gen8 each equipped with 192-GB RAM, two Intel(R) Xeon(R) CPU E5-2695 v2 2.40 GHz (12 cores) processors, 4 HD 279 GB in RAID 1, and Infinitiband network architecture (40gbps). Third, computations on the medium grid at 16° angle of attack were run

**Table 1** Computational resources and simulation times

|  | Universidad de San Buenaventura | | Universidad de Los Andes | Sabalcore |
|---|---|---|---|---|
| Alpha | 8° | 16° | 8° | 16° |
| Grid (B3) | Coarse | Coarse | Medium | Medium |
| Cells | 18.011.980 | 18.011-980 | 47.557.044 | 47.557.044 |
| Processor | Intel | Intel | Intel | Intel |
| Nodes | 1 | 1 | 4 | 4 |
| Cores | 12 | 12 | 64 | 64 |
| RAM used | 62.8 Gb | 62.8 Gb | 157 Gb | 62.8 Gb |
| Time/iter (min) | 1.39 | 1.39 | 1.25 | 0.43 |

using the HPC On-demand services offered by Sabalcore Computing Inc.[1] All the simulations were run in 4 nodes (64 processors) of the Cobalt cluster equipped with processors Intel Xeon E5-2600 Series, up to 3.1-GHz highest performing Bare-metal cores, up to 8 GB of RAM per core, Infiniband network architecture (56 Gbp), 40-Gbps Data Network and Parallel File System (1.5 Gbps of I/O). The computational resources used and simulation times are summarized in Table 1.

## 3.4 Geometry Description and Grids

The geometry for the High-Lift Common Research Model (HL-CRM) was developed by Lacy and Sclafani at The Boeing Company [3]. The design process consisted of the modification of the various high-speed elements that composed the geometry for the high-speed CRM [20] previously studied. Namely the idea was to adapt the wing/body/nacelle/pylon/horizontal-tail configuration in such a way that the new model gave precedence to increasing the lift instead of the speed of the vehicle. The only design considerations were that it must resemble a "modern commercial airplane without including all of the details" [3], while bearing in mind that the model was intended to be used as a CFD validating tool. Therefore, the new model must have a certain geometric simplicity and a spanwise consistency, which simplifies the interpretation of the CFD results. This section will attempt to give a broad explanation of the major changes performed for each element.

For the wing, four principal changes were made. First, the wing had to be "re-lofted", by a spanwise straightening, such that the other high-lift devices could be easily implemented. To do so, a set of sections that in the Y plane, were sheared vertically. Also, a span line on the upper surface was used to simplify the positioning of the span slats. The second modification was increasing the effective leading-edge radius of the wings, while making the trailing edge thickness 0.2 inches at full scale.

---

[1] http://www.sabalcore.com.

Third, the loft was changed from a four-surface loft to a one-piece loft. This was done in order to simplify CFD processes (i.e., meshing and boundary-condition setup) by having constant parametric spanlines. Finally, it was to have a straightened wing centered on the wing reference plane, which would approximate the high-speed CRM through defined rotations and translations.

The high-lifting devices chosen were slats for the leading edge and single-slotted flaps for the trailing edge. The slats' configuration had two main objectives: allowing the wing to achieve high angles of attack and forcing a nose-down pitch at stall. To achieve the first one, use of a continuous leading-edge chord distribution was chosen, while having linear chord distributions for the inboard and outboard of the nacelle. This leads to having a constant chord slat for the inboard span and a linear chord distribution for the outboard span. An additional constraint was imposed in order to resemble a typical commercial aircraft, by defining a circular arc trajectory for the slats between the stowed and deployed position [3]. Taking into the different constraints for the slats, the wing's under-slat surface (WUSS) design is straightforward. This showed that the landing position for the slats should be at 30° rotation and 22° for takeoff.

The flaps were design such that the outboard flap would have a chord which was 25% of the local wing chord. The inboard flap, however, would be constant such that it is equal to the inboard end of the outboard flap. These constraints were selected with the purpose of maintaining some flexibility of the pressure distribution. These allowed using an optimization framework, taking as the design goal a triangular pressure distribution at an angle of 40° [3].

Additionally, the stowed-flap leading edge was translated forward, to keep the linear spanwise gap distributions. Finally, a value of 40° was chosen as the maximum landing-flap angle in order to iterate the design of the overlap and gap between the flaps and the wings. Eventually, the simulations used a flap deflection of 37° for the landing configuration. Although the HL-CRM does have a nacelle-pylon configuration, the simulations conducted as part of the HLPW-3 did not include these elements in order to simplify the solution. To do so, the geometry was modified by removing the protrusion from the WUSS where the pylon was connected to the wing and filling the resulting gap in the slat using a continuous loft [21] (Fig. 3).

### 3.5   Geometry

Lastly, the fuselage was modified in order to reduce the number of surfaces that composed it (Fig. 4). The decision was to keep a number of these surfaces so as not to make major changes in comparison to the high-speed CRM. However, there were some issues when meshing this structure because the fuselage's belly showed some inconsistencies with the surface parametrization. This was solved by accommodating the discontinuities in bounding curves which once again had to go through a process of parametrization [21].
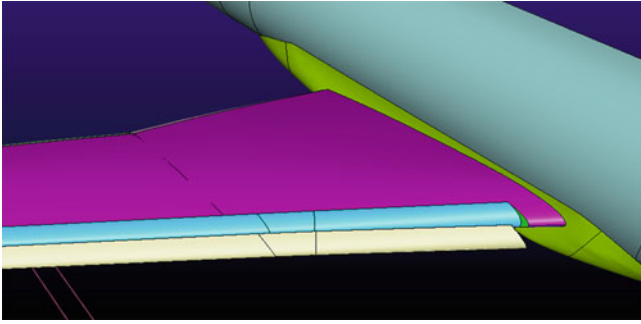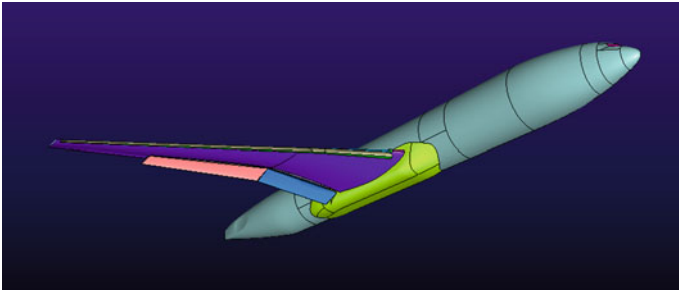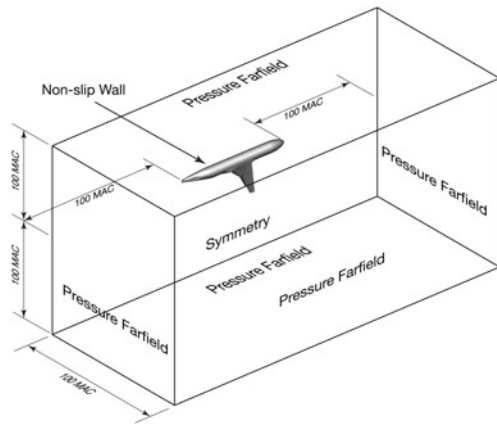
**Fig. 3** Removal of nacelle-pylon assembly



**Fig. 4** Final geometry of the HL-CRM for the 3rd CFD AIAA HiLiftPW

**Fig. 5** Boundary conditions and general dimensions of the computational domain (not to scale)



There were four types of meshes (coarse, medium, fine, and extra-fine) divided by the number of elements found in each one. The computational domain remains constant for each grid. Boundary conditions of the computational domain are illustrated in Fig. 5

**Fig. 6** Surface mesh for the B3 coarse mesh
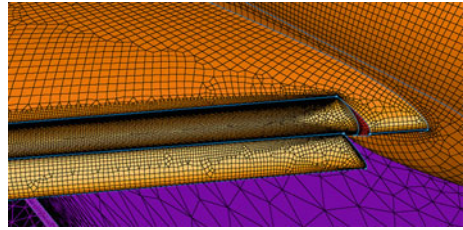


**Table 2** Grid generation parameters for various meshes

| Mesh | y plus | Initial wall spacing (in) | Layers of prisms | Growth rate | Total number of elements |
|---|---|---|---|---|---|
| Coarse | 1 | $1.75 \times 10^{-3}$ | 100 | 1.25 | 18.011.980 |
| Medium | 2/3 | $1.17 \times 10^{-3}$ | 100 | 1.25 | 47.557.044 |
| Fine | 4/9 | $7.8 \times 10^{-4}$ | 100 | 1.25 | 118.774.267 |
| Extra fine | 8/27 | $5.2 \times 10^{-4}$ | 100 | 1.25 | 397.082.470 |

For this study, the selected grid family was the B3,[2] which has a special characteristic in the surface mesh. Quads and triangles were used on the surface mesh as is shown in Fig. 6. The algorithm used to generate this surface mesh was Pointwise unstructured advancing front ortho for triangles and quads; this is a new feature of Pointwise version 18. On the leading edge and the trailing edge, the tool T-Rex from Pointwise was used to create layers of quads to correctly model the curvature, 30 layers of quads with a growth rate of 1.5 were used in the wing, flaps and slats. It is worth noting that this meshing was performed only for surfaces.

On the other hand, in order to make volumetric meshing, an additional refinement was performed. In order to capture correctly the wake on the wing, another new feature of Pointwise called *source* was used. This feature enables the user to cluster more points over specific parts of the various blocks. Relevant information of each volumetric grid, in the family B3, is summarized in Table 2.

## 4 Results and Discussion

The lift, drag, and pitching-moment coefficients computed on both coarse and medium grids at angles of attack of 8° and 16° are shown in red in Fig. 7. Numerical results submitted by participants and collected by the organizing committee of the 3rd AIAA CFD High Lift Prediction Workshop are included for reference [22]. For systematically refined grids, it is possible to estimate discretization errors when the solutions on successive finer grids asymptotically approach zero [23]. For this case, the

---

[2]Available in ftp://hiliftpw-ftp.larc.nasa.gov/outgoing/HiLiftPW3/HL-CRM-Grids.
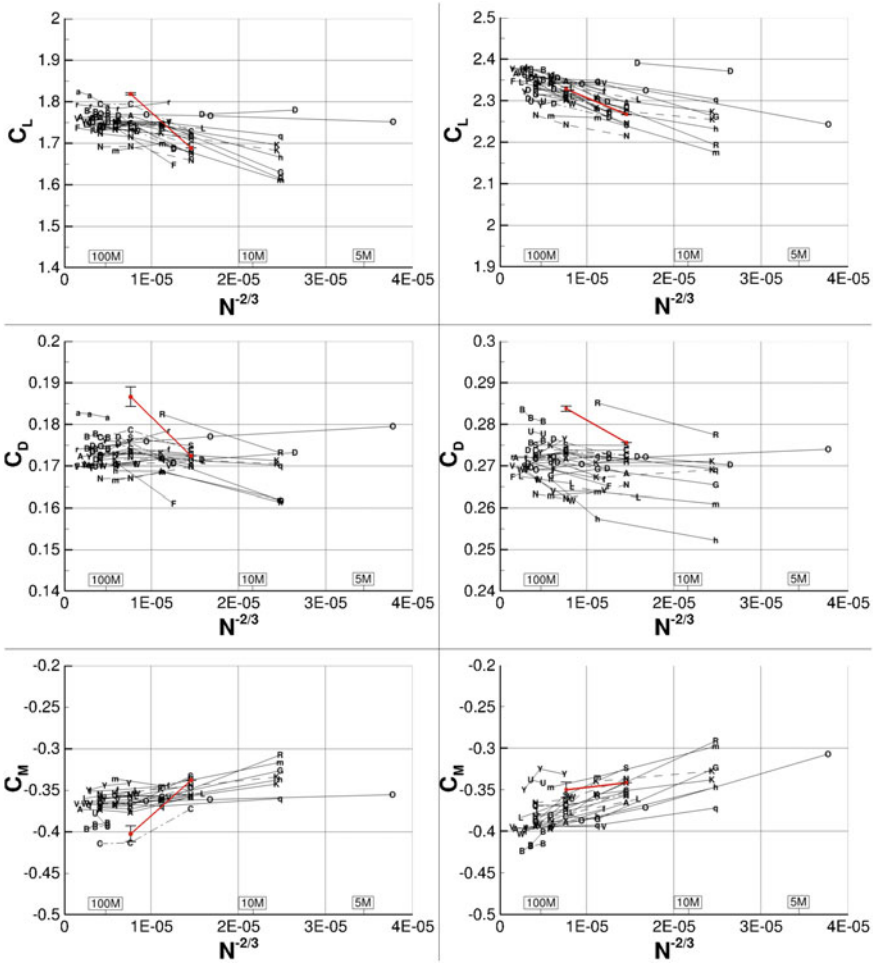
**Fig. 7** Lift, drag, and moment coefficients computed on the NASA Common Research Model for angles of attack of 8° and 16°. Values predicted by SU2 in the present work are shown in red, and solutions provided by participants of HiLiftPW-3 are shown in black

results were plotted against $N^{-2/3}$, assuming a second-order convergence. Although solutions computed on at least three grids of the mesh families are required to perform a grid convergence study, the results presented in this chapter were obtained on only coarse and medium grids of family B3.

Lift coefficients predicted by SU2 at an angle of attack of 8° on both grids were within the results submitted by the participants; however, the value computed on the medium grid was slightly above the group of solutions. The results obtained at an angle of attack of 16° were more promising. Values computed on both coarse and

medium grids are close to the mean of the solutions submitted by the participants, and they appear to follow a similar tendency as the grid is refined.

The drag coefficient is harder to predict than the lift coefficient. Comparison with solutions submitted by the participants showed that the drag computed on the coarse grid was within the dispersion, but it was overpredicted on the medium grid. The drag coefficient computed on the medium grid at an angle of attack of 16° was comparable to values identified by letters B and R but higher than most solutions. At an angle of attack of 8°, the value computed for the same grid was higher than all solutions presented in the plot.

Finally, the moment coefficient predicted on the coarse grid for both angles of attack are above the mean value but well within the dispersion of the solutions reported by the participants. The value computed on the medium grid at an angle of attack of 8° was lower than most solutions and does not seem to follow a similar trend as the grid is refined; however, the value computed at an angle of attack of 16° on the medium grid was in closer agreement with the solutions and showed a similar trend.

In general, the aerodynamic coefficients computed on both grids are within the dispersion range of results reported by the participants of the HiLiftPW-3, except for the values computed at angle of 8° on the medium grid. A solution for the fine mesh would provide further information on the aerodynamic forces at this angle of attack, and it would help to assess whether the solutions are within the asymptotic range. For the present work, the solutions computed are good enough to identify the main features of the flow around an airplane in high-lift configuration.

The pressure-coefficient distribution computed at an angle of attack of 8° on eight sections of the wing are shown in Fig. 8. The locations of the sections are shown in Fig. 9 for reference. Differences between the solutions computed on both grids were very small in the three sections near the wing root but increased considerably on the sections of the wing located along the outboard flap. Larger negative values were predicted on the medium grid over the suction side of the flap, near the leading edge, and towards the trailing edge of the main wing. Furthermore, wing sections located near the wingtip at 81.9 and 90.1% showed larger positive-pressure peak values over the bottom surface of the main wing close to the leading edge and over the bottom surface of the slat. These results agree with the higher-lift coefficient predicted on the medium grid, associated with larger suction values, and more negative-moment coefficients produced by the backward displacement of the center of pressure.

It is interesting to note that the differences between pressure coefficients computed in both grids are more evident over the suction side of the outer flap, but they are almost unnoticeable near the trailing edge of the sections located close to the wingtip. Unfortunately, no experimental data is available at the present time to validate these results, but it is expected that the complexities of the flow over the three wing elements are better captured by finer grids, and hence the results predicted on the medium grid were more accurate.

Pressure-coefficient distributions showed a better correlation between solutions computed on the coarse and medium grids at an angle of attack of 16° (Fig. 10). The differences reported at an angle of attack of 8° decreased substantially over most of the slat and main wing; only a small discrepancy remains over the pressure side of the main wing near the leading edge at 89.1 and 90.8%. A variation was still present
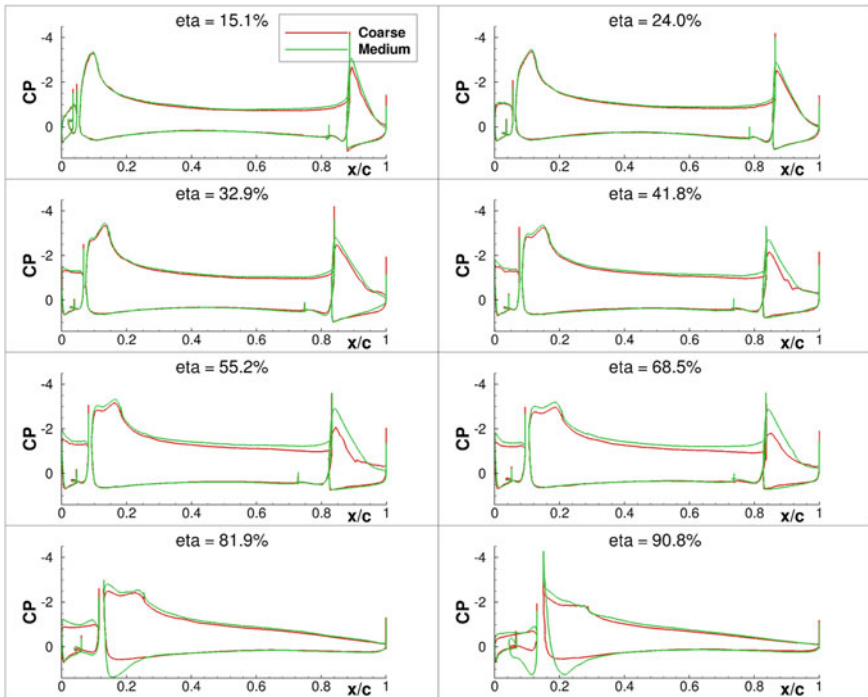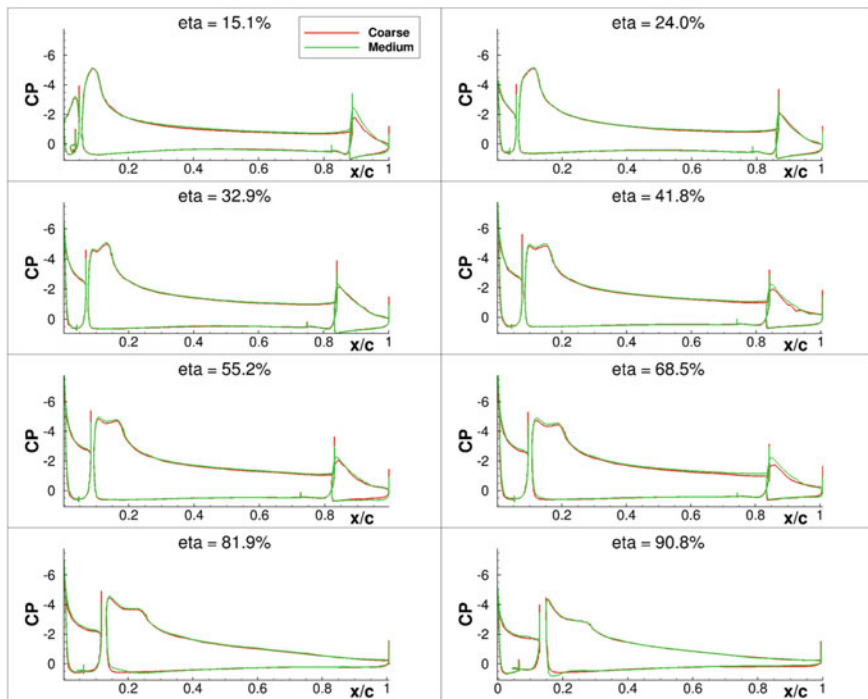


**Fig. 8** Pressure coefficient distribution on wing sections located at eight locations along the wingspan computed on both coarse and medium grids at an angle of attack of 8°
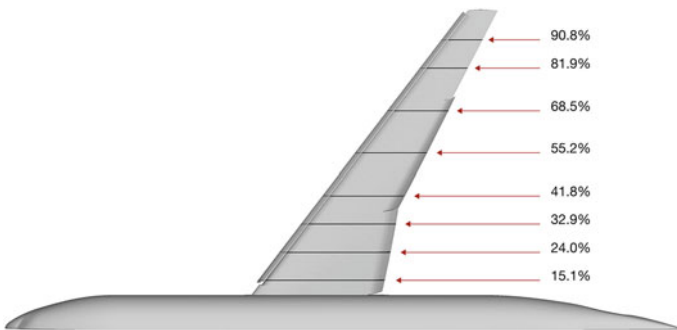


**Fig. 9** Location of the eight section cuts along the wingspan

**Fig. 10** Pressure-coefficient distribution on wing sections located at eight locations along the wingspan computed on both coarse and medium grids at an angle of attack of 16°

over the suction side of the outboard slat, but it was considerably smaller than that for the case evaluated at an angle of attack of 8°.

The effects of slats and flaps on the flow can be observed on the pressure distribution. At a relatively low angle of attack of 8°, more suction is produced over the main wing on the sections located in front of the flap than in the section without flap (i.e., near the wingtip). The pressure recovery towards the trailing edge of the main element becomes less severe up to the point where pressure becomes constant, and it begins to increase slightly. This reduction in the adverse pressure gradient is evidence of the increment in the local velocity due to the circulation effect produced by the flap on the main wing. Because of the modification in the pressure distribution, the lift produced by the main wing increases, while the flow is less prone to separate. At this angle of attack, a large amount of lift is achieved by the main wing and the flap but little by the slat.

At the higher angle of attack of 16°, the aerodynamic load on the slat increases, and its contribution to the total lift becomes more relevant. Induced velocity from the main wing on the flow near the trailing edge of the slat increases its circulation and the tangential velocity over the upper surface (i.e., circulation effect) [6]. Since the local velocity is higher, pressure recovery is less severe, which benefits the boundary

layer. Furthermore, the larger difference in pressure coefficient on the surface of the slat, particularly near the trailing edge, is evidence of high dumping-velocity ratios which are associated with the dumping effect [6]. The slat effect can also be appreciated on the suction peak of the main wing as the circulation around the slat reduces the high velocities around the leading edge at high angles of attack.

Distribution of skin-friction coefficient computed at the angle of attack of 8° is shown in Fig. 11. The flow is attached over most of the surface on all of the wing section located along the wingspan; however, some spots of separated flow were predicted on both grids near the leading edge of the main and on the medium grid on the upper surface of the outboard flap. The same separation was not seen on the coarse grid.

Similar results were predicted at 16° angle of attack (Fig. 12). Flow separation was computed on the medium grid over a portion of the outboard flap but none was observed on the coarse grid. The flow remains attached over most of the wing and no evidence of stall onset was estimated.

An inspection of the surface streamlines showed the flow separated over a portion of the flap in the solution computed on the coarse grid at 8° angle of attack (Fig. 13). On the medium grid, the flow is attached over the inboard flap, except for the tips, but
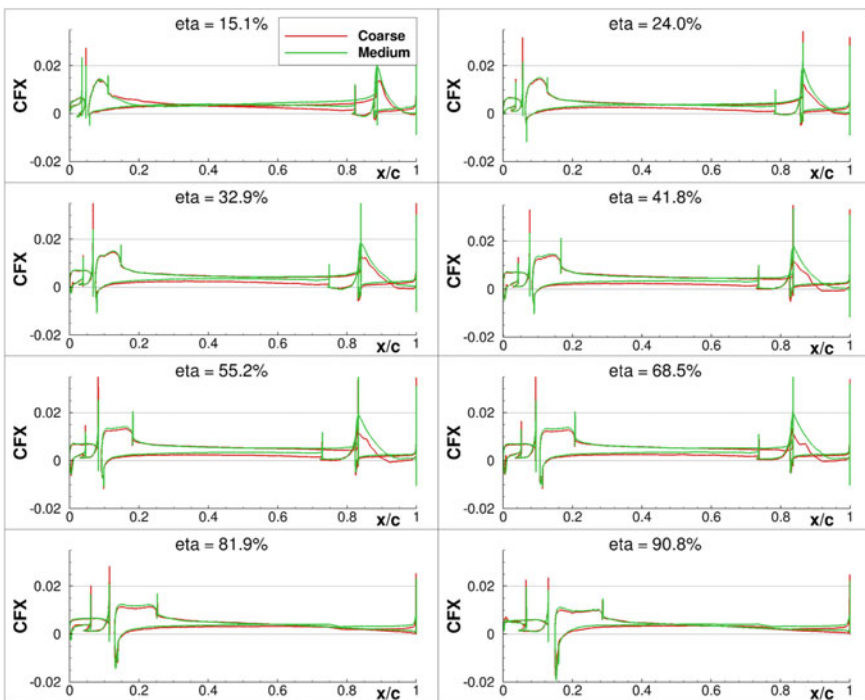


**Fig. 11** Skin-friction coefficient distribution on wing sections located at eight locations along the wingspan computed on both coarse and medium grids at an angle of attack of 8°
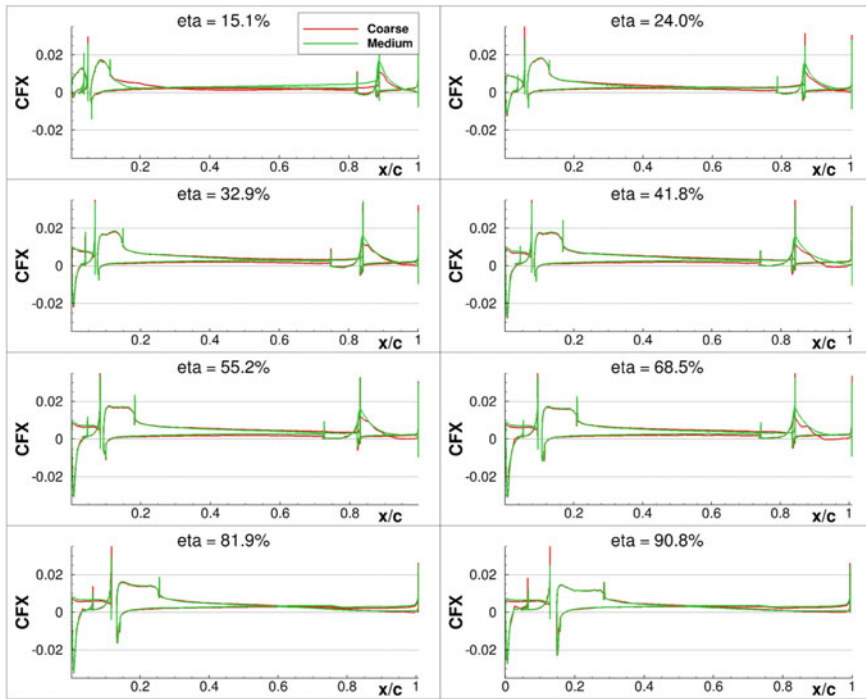
**Fig. 12** Skin-friction coefficient distribution on wing sections located at eight locations along the wingspan computed on both coarse and medium grids at an angle of attack of 16°

the onset of flow separation was captured on the outboard flap. These observations are in good agreement with the distribution of skin-friction coefficients of Fig. 12.

Similarly, surface streamlines in Fig. 14 showed a region of separated flow over the outboard flap on the coarse grid, but this was not the case for the medium grid.

Figure 15 shows vortical structures of the flow in the wake of the wing computed on the medium grids. At 8° angle of attack, lines of constant x-vorticity values showed three counter-clockwise free vortices produced by the flow around the wingtip, the tip of the outboard flap, and the gap between inboard and outboard flaps, while a clockwise free vortex is produced by the tip of the inboard flap at the wing root. The wingtip vortex dissipates relatively fast within two chords downstream (values of x-vorticity between -20s-1 and 20s-1 are not visible in the plot) but vortices shedding from the flaps dissipate further downstream at approximately six chords. At 16° angle of attack, similar vortical structures were captured in the wake of the wing, and although they are larger, they seem to dissipate more quickly at about four chords downstream. Overdamping of the wingtip and flap vortices may be due to poor grid resolution in the wake of the wing as investigated by Park et al. [24] and the turbulence model (i.e., SA) [25].
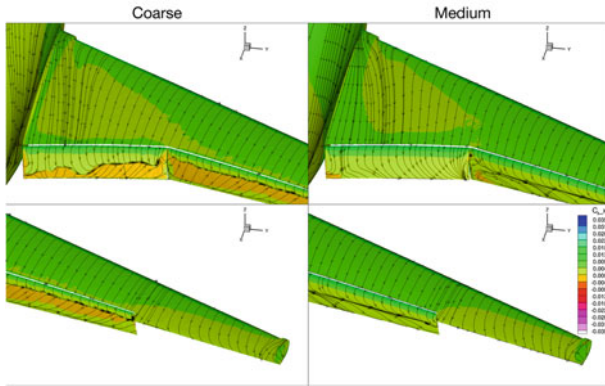
**Fig. 13** Contours of skin-friction coefficient and surface streamlines computed on the coarse and medium grids at 8° angle of attack
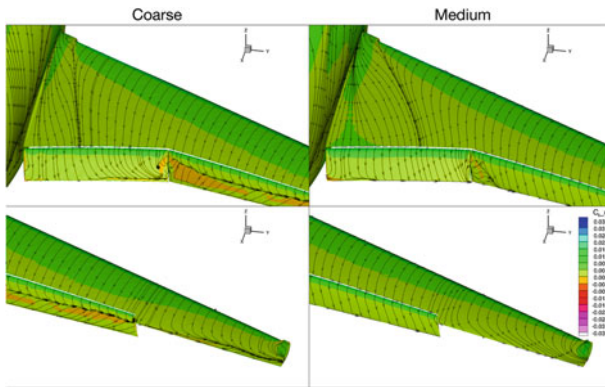


**Fig. 14** Contours of skin-friction coefficient and surface streamlines computed on the coarse and medium grids at 16° angle of attack
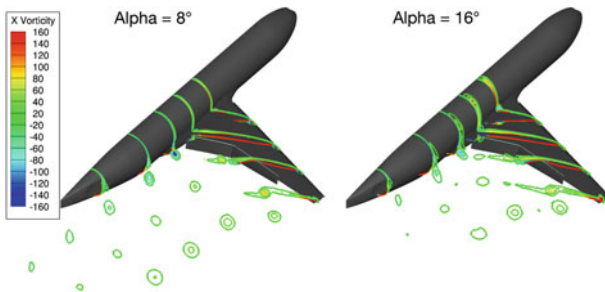


**Fig. 15** Lines of constant x-vorticity computed on the medium grid

## 5   Conclusions

The flow over the NASA's Common Research Model in high-lift configuration was analyzed by means of numerical simulations. For this purpose, Stanford's University SU2 was used to compute solutions at 8° and 16° angles of attack on coarse and medium grids of family B3, provided by the organizing committee of the 3rd HiLiftPW.

A comparison of numerical results from SU2 and data submitted by participants of the 3rd HiLiftPW showed that values of lift, drag, and moment coefficients computed on the coarse grid were within the range of solutions, except for the drag coefficient at 16° angle of attack, which was rather overestimated. Solutions computed on the medium grid were in general outside of the solution, particularly at 8° angle of attack; however, lift and moment coefficients computed on the medium grid at 16° angle of attack are in good agreement with solutions reported.

The pressure-coefficient distribution over eight sections located along the wingspan indicated significant differences on the suction side of the outboard flap between solutions computed on the coarse and medium grids. Similar discrepancies were also noted in the contours of skin-friction coefficients and in surface-restricted streamlines over the upper surface of the outboard flap. Poor resolution of the coarse grid was found to be the most probable cause.

Some of the more relevant effects of multi-element airfoils in high-lift configurations were observed in the numerical results such as a circulation effect, high dumping-velocity ratios at the trailing edge of the slat due to dumping effect, and a slat effect on the suction peak of the main wing. Furthermore, primary and secondary vortices shed from the wingtip and flaps were visualized as lines of constant x-vorticity in planes located in the wake of the wing. It was observed that vorticity dissipated quicker in the wake at 16° angle of attack than at 8° angle of attack. This phenomenon has been attributed to turbulence-model limitations and poor resolution of the grid in the wake of the wing.

## References

1. Runsey, C., Slotnik, J.: In: Overview and Summary of the Second AIAAA high Lift Prediction Workshop
2. Rudnik, R., Huber, K., Melber-Wilkending, S.: EUROLIFT Test Description for the 2nd High Lift Prediction

3. Lacy, D., Sclafani, A.: Development of the High Lift Common Research Model (HL-CRM): A representative high lift configuration for transonic transport. In: AIAA SciTech Forum, 54th AIAA Aerospace Sciences Meeting, San Diego (2016)
4. van Dam, C.: The aerodynamic design of multi-element high-lift systems for transport airplanes. Prog. Aerosp. Sci. 101–144 (2002)
5. Meredith, P.: Viscous phenomena affecting high-lift systems and suggestions for future CFD development. High-lift Syst. Aerodyn. (1993)
6. Smith, A.M.O.: High-lift aerodynamics. J. Aircr. **12**, 501–530 (1975)
7. Kharea, A., Baiga, R., Ranjana, R., Shaha, S., Pavithrana, S., Nikama, K., Moitrab, A.: Computational simulation of flow over a high-lift trapezoidal wing. ICEAE (2009)
8. Becker, K., Vassber, J.: Numerical aerodynamics in transport aircraft design. In: Note on Numeric Fluid Mechanics, pp. 209–220. Springer, Berlin (2009)
9. Mathias, D., Cummings, R.: Navier-stokes analysis of the flow about a flap edge. J. Aircr. 833–838 (1998)
10. Rogers, S., Roth, K., Nsh, S.: CFD validation of high-lift flows with significant wind-tunnel effects. In: Applied Aerodynamics Conference, Denver. (2000)
11. Chaffin, M., Pirzadeh, S.: Unstructured Navier-stokes high-lift computations on a trapezoidal wing. In: 23rd AIAA Applied Aerodynamics Conference, Toronto (2005)
12. Rumsey, C., Yingb, S.X.: Prediction of high lift: review of present CFD capability. Prog. Aerosp. Sci. 145–180 (2002)
13. Rumsey, C.: High lift prediction workshop. In: Third High Lift Prediction Workshop (2017)
14. Economon, T., Palacios, F., Copeland, S., Lukaczyk, W., Alonso J.: An open-source suite for multiphysics simulation and design. In: 51st AIAA Aerospace Sciences Meeting, Grapevine (2013)
15. Molina, E., Spode, C., Manosalvas-Kjono, D.E., Nimmagadda, S., Economon, T., Alonso, J., Righi, M.: Hybrid RANS/LES calculations in SU2. In: 23rd AIAA Computational Fluid Dynamics Conference (2017)
16. Economon, T., Mudigere, D., Bansal, G., Heinecke, A., Palacios, F., Park, J., Smelyanskiy, M., Alonso, J., Dubey, P.: Performance optimization for scalable implicit RANS calculations with SU2. Comput. Fluids 146–158 (2016)
17. Roe, P.L.: Approximate Riemann solvers, parameter vector, and difference schemes. J. Comput. Phys. 357–372 (1981)
18. Turkel, E., Vatsa, V.N., Radespiel, R.: Preconditioning Methods for Low-Speed flows (1996)
19. Spalart. P.R., Allmaras, S.R.: A one equation turbulence model for aerodynamic flows. In: 30th AIAA Aerospace Sciences Meeting and Exhibit (1992)
20. Vassber, J.C., DeHaan, M.A., Rivers, S.M., Wahls, R.A.: Development of a common research model for applied CFD validation studies. In: AIAA Applied Aerodynamics Conference, Honolulu, Hawaii (2008)
21. Taylor, N., Jones, B., Gammon, M.: 1st AIAA Geometry and Mesh Generation Workshop; GMGW-1 Presentations, 4 June 2017. Retrieved from http://www.pointwise.com/gmgw/gmgw1/GMGW1-Committee-Taylor-Geometry.pdf consulted on July 11, 2017
22. Sclafani, T., Slotnik, J., Chaffin, M., Feinmann, J., Melber, S.: HiliftPW-3 Case 1 Results Summary, Summary Case 1 2 copy (2017)
23. Diskin, B., Thomas, J., Rumsey, C., Schwoeppe, A.: Grid Convergence for Turbulent Flows (Invited). In: 53rd AIAA Aerospace Sciences Meeting, American Institute of Aeronautics and Astronautics (2015)
24. Park, M.A., Lee-Raush, E.M., Rumsey, C.L.: In: FUN3D and CFL3D Computations for the First High Lift Prediction Workshop. 49th AIAA Aerospace Sciences Meeting, 4–7 Jan, pp. 24, Orlando, FL (2011)
25. Nichols, R.: Algorithm and turbulence model requirements for simulating vortical flows. In: 46th AIAA Aerospace Sciences Meeting and Exhibit, American Institute of Aeronautics and Astronautics (2008)